PHOTON PRODUCTION AND FORWARD-BACKWARD MULTIPLICITY CORRELATION IN ALICE AT THE LHC

By

Sudipan De

Enrollment No. PHYS04200904001

Variable Energy Cyclotron Centre, Kolkata

A thesis submitted to

The Board of Studies in Physical Sciences

In partial fulfillment of requirements for the Degree of

DOCTOR OF PHILOSOPHY

of

HOMI BHABHA NATIONAL INSTITUTE

February, 2014

Homi Bhabha National Institute

Recommendation of the Viva Voce Board

As members of the Viva Voce Board, we certify that we have read the dissertation prepared by **Sudipan De** entitled **Photon production and forward-backward multiplicity correlation in ALICE at the LHC** and recommend that it may be accepted as fulfilling the dissertation requirement for the degree of Doctor of Philosophy.

S. Bhattacharya ....Date: 26/2/14

Chairman- Dr. S. Bhattacharya

Tapan Nayak ....Date: 26/2/2014

Convener- Dr. T. K. Nayak

Jane Alam ....Date: 26/2/2014

Member 1- Dr. J. Alam

Chatterjee ....Date: 26/02/2014

Member 2- Dr. S. Chattopadhyay

Hiranmaya Mishra ....Date: 23/03/2014

Member 3 (External Examiner)- Dr. H. Mishra

Finally approval and acceptance of this dissertation is contingent upon the candidate's submission of the final copies of the dissertation to HBNI.

I hereby certify that I have read this dissertation prepared under my direction and recommend that it may be accepted as fulfilling the dissertation requirement.

Date: 26/2/2014

Place: VECC, Kolkata

STATEMENT BY AUTHOR

This dissertation has been submitted in partial fulfillment of requirements for an advanced degree at Homi Bhabha National Institute (HBNI) and is deposited in the Library to be made available to borrowers under rules of the HBNI.

Brief quotation from this dissertation are allowable without special permission, provided that accurate acknowledgement of source is made. Requests for permission for extended quotation from or reproduction of this manuscript in whole or in part may be granted by the Competent Authority of HBNI when in his or her judgement the proposed use of the material is in the interests of scholarship. In all other instances, however, permission must be obtained from the author.

Sudipan De

DECLARATION

I, hereby declare that the investigation presented in the thesis has been carried out by me. The work is original and has not been submitted earlier as a whole or in part for a degree/diploma at this or any other Institution/University.

Sudipan De

Dedicated to my parents

ACKNOWLEDGEMENTS

I would never have been able to finish my dissertation without the guidance of my supervisor, help from friends, and support from my family.

I would like to express my special appreciation and thanks to my advisor Prof. Tapan Kumar Nayek, you have been a tremendous mentor for me. I would like to thank him for his excellent guidance, caring, patience, and providing me with an excellent atmosphere for doing research. His advice on both research as well as on my career have been priceless. I would also like to thank my committee members, Prof. S. Bhattacharya, Prof. J. Alam, Prof. S. Chattopadhyay for their encouragement and insightful comments.

I thank my collaborator Prof. Brijesh Kumar Shrivastava for giving me the opportunity to work with him. I would like to thank Prof. Subhasish Chattopadhyay and Prof. Bedangadas Mohanty for their advice, discussion and support for my understanding on experimental high energy physics and data analysis. I would thank Prof. Premamoy Ghosh and Prof. Anand Kumar Dubey for their support and useful discussion.

I would like to convey my sincere gratitude to Prof. D. K. Srivastava and Prof. Y.P. Viyogi for their valuable advices, inspirations and encouragement during these years.

I am really grateful to my seniors Dr. Sidharth Kumar Prasad, Dr. Mrignka Mouli Mondal and Dr. Satyajit Jena for their support and help regarding my data analysis. My special thanks to my friend, colleague and collaborator Subhash Singha for his support and discussion during data analysis. I would like to thank my other collaborator Dr. Igor Altsybeev for his useful discussion and support.

I take this opportunity to thank my colleagues and friends Dr. Nihar Ranjan Sahoo and Dr. Somnath De with whom I spent lot of times during my Ph.D. period. I would also like to thank my other colleagues Arnab, Md. Younus and Manish for spending friendly time with them. I would thank to my seniors Dr. Victor Roy, Dr. Santosh Kumar Das, Dr. Sabyasachi Ghosh, Dr. Haridas Pai and Dr. Payel Mohanty for their useful discussion and suggestion. I would like to thank Prithwish Tribedy and Sanjib Muhuri for discussion on various parts of physics.

I would like to thank VECC grid peer for proving me enormous support for my huge computational work. I thank to ALICE collaboration and Physics Working Group - Light Flavour (LF) and Correlation Fluctuation (CF) for guiding my analysis.

A special thanks to my family. Words cannot express how grateful I am to my wonderful parents and sister for all of the sacrifices that you have made on my behalf. Your prayer for me was what sustained me thus far. Last but not the least, I would like to thank my wife, Debashree Majumder. She was always there cheering me up and stood by me through all the times.

Sudipan De

SYNOPSIS

The Large Hadron Collider (LHC) at CERN offers unique possibilities to study particle production mechanisms in proton-proton (p-p), proton-lead (p-Pb) and lead-lead (Pb-Pb) collisions at ultra-relativistic energies. The ALICE experiment at the LHC is capable of measuring majority of the particles produced in these collisions, thereby making it possible to study the bulk properties of matter formed in these collisions. ALICE has taken data for p-p collisions at $\sqrt{s} = 0.9$ TeV, 2.76 TeV, 7 TeV and 8 TeV; p-Pb collisions at $\sqrt{s_{NN}} = 5.02$ TeV and Pb-Pb collisions at $\sqrt{s_{NN}}$ = 2.76 TeV. Work presented in this thesis is based on the data analysis of photons at forward rapidities using the Photon Multiplicity Detector (PMD), charged particle production and forward-backward multiplicity correlations using the central barrel detectors. A brief discussion on each of these topics is given below.

1. Photon production at forward rapidities:

Photon multiplicities and pseudorapidity distributions in the forward region of 2.3 $< \eta <$ 3.9 have been measured in ALICE by using the Photon Multiplicity Detector (PMD). Photon measurements provide complimentary information to that of the charged particles as majority of the photons are decay products of produced particles such as neutral pions. This work highlights the particle production mechanism in forward rapidity region and provides the information about longitudinal scaling of produced particles.

a) Photon Multiplicity Detector (PMD) in ALICE:

The Photon Multiplicity Detector in ALICE is designed to measure precise position and multiplicity of photons in the forward rapidity ($2.3 < \eta < 3.9$) with full coverage in azimuthal angle. PMD consists of a Charged Particle Veto plane (CPV), a lead converter of thickness $3X_0$, and a Preshower plane (PRE). The two detector planes are made up of large arrays of highly granular, honeycomb proportional counters. Photons, crossing through the lead converter, generate shower of electrons and positrons, which produce signals in the Preshower plane. The PMD consists of 50 modules, each consisting of 4608 cells. PMD measures the multiplicity and the spatial distribution of photons on an event-by-event basis.

b) Beam tests of the PMD modules:

Response of the PMD modules to charged particles and electrons have been studied by performing detector tests using pion and electron beams at CERN-PS. The modules are tested with pion beams at 3 GeV and electron beams in the range of 1 GeV to 3 GeV. Results of the test beams have been compared to a detailed simulation of the detector setup using the Aliroot GEANT framework. The ADC distribution of pions has been fitted to a Landau function and the Most Probable Value (MPV) of the distribution has been extracted. A conversion relation has been obtained between the calculated energy deposition from simulation and the digitized signal (in ADC) from the test beam data. In addition to characterizing the detector for response to various incoming particles, these studies provide the photon-hadron discrimination threshold in order to choose the photon sample.

c) Multiplicity and pseudorapidity distributions of photons:

Photon multiplicities from the experimental raw data have been extracted after data clean up, calibration and clustering of cells. After applying the photon-hadron discrimination thresholds on the reconstructed data, one obtains the photon-like distributions. For the p-p collisions, the photon distributions have been obtained from the photon-like sample by using unfolding method, which uses detailed simulations using PYTHIA and PHOJET event generators. The unfolding method is performed in each η-bin in order to obtain the pseudorapidity distribution of the photons.

The systematic uncertainties have been obtained from the variation of the photon-hadron discrimination thresholds, method of unfolding, different event generators. A detailed study has been made to understand the effect of the material in front of the PMD.

The corrected multiplicity and pseudorapidity distributions of photons in p-p collisions are compared with the predictions from PYTHIA and PHOJET event generators. It is observed that, at 0.9 TeV PHOJET results are comparable with the experimental data, PYTHIA under predicts the data, whereas at 2.76 and 7 TeV both the models under predict the data. The multiplicity distributions have been fitted to both single Negative Binomial Distribution (NBD) function and double NBD function. Beam energy dependence of average photon multiplicity has been studied in the forward rapidity region ($2.3 < \eta < 3.9$). It is found that average photon multiplicity increases with $\sqrt{s}$ as $\ln\sqrt{s}$ as well as with a power law. Photon production is compared with the charged particle production and it is found to be comparable in this η-acceptance. Limiting fragmentation behavior of photons is studied and the results are compared with the PHOJET.

d) Photon production in p-Pb collisions at $\sqrt{s_{NN}}$ = 5.02 TeV:

Pseudorapidity distribution of photons has been measured in the p-Pb collisions at $\sqrt{s_{NN}} = 5.02$ TeV. The photon multiplicity distributions are obtained after correction for efficiency and purity at each η-bin. The efficiency and purity of the detector has been calculated using the DPMJET event generator. The results are presented for minimum bias events as well as for different centrality classes from 0-5% to 60-80%. It is observed that photon production is highest in the top centrality class and decreases with more peripheral collisions. The results have been compared with the DPMJET event generators.

2. Charged particle production in p-Pb collisions at $\sqrt{s_{NN}}$ = 5.02 TeV:

Charged particle pseudorapidity distribution has been measured in the mid rapidity region for the Non Single Diffractive (NSD) events at $\sqrt{s_{NN}} = 5.02$ TeV. The results have been compared with the different model predictions. DPMJET and HIJING with gluon shadowing are found to closest to the data.

3. Forward-backward Multiplicity Correlations:

Forward backward multiplicity correlations of charged particles have been studied for p-p collisions at LHC energies. The study of correlations among particles produced in different rapidity regions may provide an understanding of the elementary (partonic) interactions, which lead to hadronization. Since it is believed that correlation of particles produced in the early stage of the collisions spread over a large rapidity interval, the measurement of the long-range rapidity correlations of the produced particle multiplicities could give insight into the space-time dynamics of the early stages of the collisions. Forward-backward multiplicity correlations have been studied across a wide range of energies and colliding species. The correlations over small range in rapidity are believed to be dominated by short-range correlations which are due to the particles produced from cluster decay, resonance decay or jet correlation and those extending over a wide range in pseudorapidity could be interpreted due to multiple parton interactions.

The data from the central barrel detectors (TPC and ITS) has been used to study the forward backward multiplicity correlation for minimum bias p-p events within the acceptance of $|\eta| < 0.8$ and $0.3 < p_T < 1.5$ (GeV/c). Two separate pseudorapidity windows with a bin width of 0.2 to 0.8 rapidity units have been chosen symmetrically around $\eta = 0$. Multiplicity correlation strengths have been studied as a function of η-gap between the two windows as well as the width of these windows. It is observed that correlation strengths decrease with increasing η-gap i.e. with increasing distance between two η windows and increase with the width of the each window. The results have been compared with three different event generators, such as, PYTHIA Perugia-0, PYTHIA Perugia-11 and PHOJET. It is observed that PYTHIA Perugia-0 is closer to the data than the other two event generators for all the energies. PHOJET explains the data at 0.9 TeV and under predict at 2.76 TeV and 7 TeV. PYTHIA-Perugia-11 over predict the data at each energy. Relative correlation has been studied in terms of the ratio of the correlation strength of 7 TeV and 2.76 TeV with respect to 0.9 TeV and it is found that the correlation strength significantly increases with beam energy.

Method for the analysis of forward backward multiplicity correlation in heavy-ion collision has been studied using the HIJING event generator. The results are

presented for different centralities using two different methods. It is shown that the method, which takes into account the fluctuation in centrality selection, should be chosen to determine the forward-backward correlation strength in heavy-ion collisions.

Contents

List of Figures

List of Tables

1 Introduction

Since the 1970s, particle physicists have described the fundamental structure of matter using an elegant theory called the *"Standard Model"*. The model describes how everything we observe in the Universe is made from a few basic blocks called fundamental particles, governed by four forces. To test the predictions and limits of the *Standard Model*, physicists have built world's largest accelerator, the Large Hadron Collider (LHC) at CERN, Geneva [1, 2]. The LHC has already achieved one of its main goal by discovering the *"Higgs boson"* [3]. Physicists hope that the LHC will also highlight some of the open questions in elementary particle physics, such as, physics beyond the Standard Model, existence of extra dimensions, matter and anti-matter asymmetry and the unifications of the fundamental forces. Beside these, LHC can provide information about the early universe by producing a state of matter, which is very similar to the state just after a few microseconds of the *Big Bang* [4, 5]. This phase is called *quark-gluon plasma (QGP)* [6], consisting of asymptotically free quarks and gluons, which are the basic building blocks of the matter.

1.1 The elementary particles and the Standard Model

All matter around us is made of elementary particles. The Standard Model of particle physics explains how these elementary particles interact governed by the four fundamental forces.

All the elementary particles can be divided in two groups such as *quarks* and *leptons*. There are six quarks [up (u), down (d), charm (c), strange (s), top(t), bottom(b)] and six leptons [electron (e^-), electron neutrino (ν_e), muon (μ^-), muon neutrino (ν_μ), tau (τ), tau neutrino (ν_τ)]. These particles are called "*fermions*". The interactions between the particles are governed by the four fundamental forces: the strong force, the weak force, the electromagnetic force, and the gravitational force. According to the Standard Model, three of the fundamental forces result from the exchange of carrier particles called "*bosons*". The strong force is carried by the "gluon", the electromagnetic force is carried by the "photon", and the "W and Z bosons" are responsible for the weak force. The *quarks* and *leptons* can be grouped into three different "*generations*". The lightest and most stable particles make up the first generation, whereas the heavier and less stable particles belong to the second and third generations.

The leptons can exist independently but the quarks are found in triplets and doublets. The triplets are called "*baryons*" and the doublets are called "*mesons*". Collectively baryons and mesons are know as "*hadrons*".

Generation	quarks	Charge (e)	mass (MeV/c^2)
1	u	2/3	1.7-3.3
	d	- 1/3	4.1-5.8
2	c	2/3	1270^{+70}_{-90}
	s	- 1/3	101^{+29}_{-21}
3	t	2/3	$172000 \pm 900 \pm 1300$
	b	- 1/3	4670^{+180}_{-60}

Table 1.1: The elementary particles (Fermions).

Generation	leptons	Charge (e)	mass (MeV/c^2)
1	e^{-1}	-1	0.511
	ν_e	0	<0.000002
2	μ^{-1}	-1	105.66
	ν_μ	0	<0.19
3	τ^{-1}	-1	1776.82
	ν_τ	0	<18.2

Table 1.2: The elementary particles (Fermions).

1.2 Quantum Chromodynamics (QCD)

The interaction between the quarks and gluons is known as strong interaction, which is governed by a well-known theory called Quantum Chromodynamics (QCD). QCD is an important part of the Standard Model of particle physics. QCD introduces a new quantum number called *"color quantum number"*. According to QCD quarks carry three different colors red, green and blue, while the anti-quarks carry anti-red, anti-green and anti-blue respectively. The strong force carrier gluons are mixtures of two colors, such as red and anti-green, which constitutes their color charges. In QCD there are eight independent color states of gluons.

QCD has two different properties *"confinement"* and *"asymptotic freedom"* [7, 8].

Due to the confinement an infinite amount of energy is needed to separate two quarks; they are bound into hadrons such as the proton and the neutron. According to asymptotic freedom the interaction between quarks gets weaker as their separation decreases i.e. the coupling between the quarks and gluons gets weaker in very high energy reaction.

Several different approaches are used to study the QCD. One of them is perturbative QCD (pQCD) which is based on asymptotic freedom and where the perturbation theory can be applied. pQCD is applicable in a very short distance scale or in case of large momentum transfer. The most well established non-perturbative approach to QCD is the lattice QCD (lQCD) approach that uses a discrete set of space-time points (called the lattice).

1.3 QCD phase diagram

The quarks and gluons are confined inside the hadrons in normal temperature and nuclear density. At extremely high temperature and/or baryon density quarks and gluons may become de-confined. This phase consists of asymptotically free quarks and gluons. This de-confined state of matter is called the *"Quark Gluon Plasma (QGP)"* state. The confined and de-confined state of matter have been presented pictorially in the QCD phase diagram [9] in Fig. 1.1. X-axis represents the chemical potential (μ) and Y-axis represents the temperature (T). The line that rises up from the nuclear/quark matter transition and then bends back towards the T axis, with its end marked by a star, is the conjectured boundary between confined and deconfined phases. If we heat up the system along the T axis, there is a *crossover* from hadronic phase to the quark gluon plasma. Whereas at large chemical potential

1st Order phase transition is speculated between two phases [10]. It is expected that there is an end-point of the *first order phase* transition line, which is known as *"QCD critical point"*. In the Fig. 1.1 the end point of the solid line, which is marked by a star is believed as *QCD critical point*.

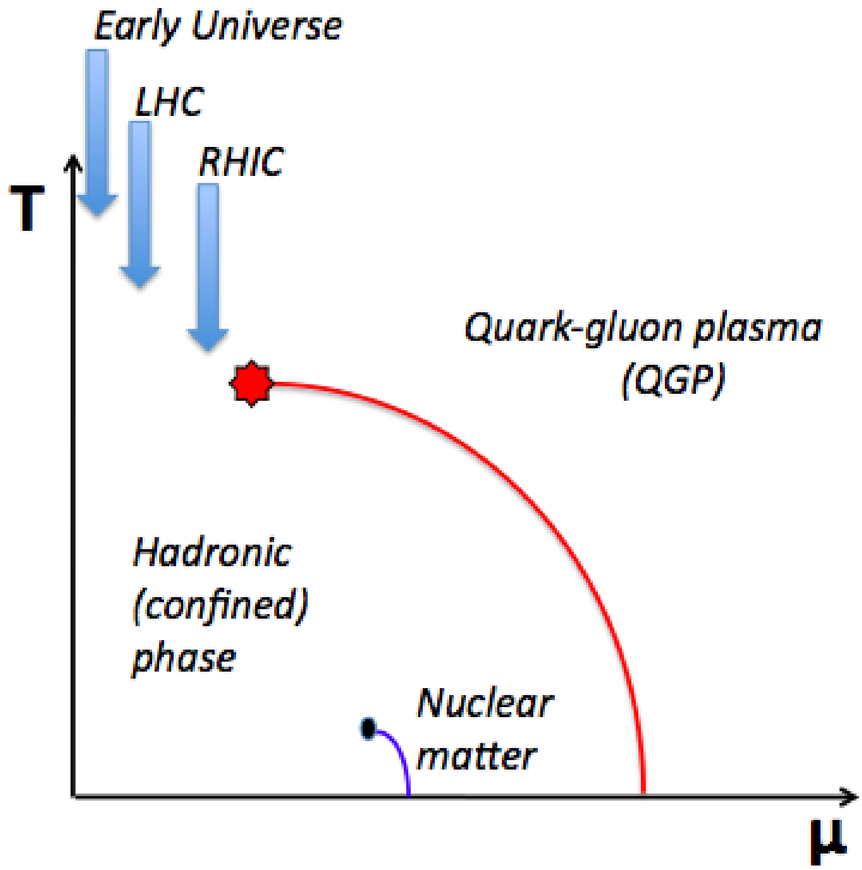

Figure 1.1: A schematic picture of the QCD phase diagram.

1.4 Relativistic collisions

From the Fig. 1.1 it is clear that to create the QGP state in the laboratory we need to achieve very high temperature for a fixed chemical potential. To do so, different collisions are performed in the LHC experiments at CERN like heavy-ion, proton-proton and proton-lead collisions. In heavy-ion collisions, nuclei are collided at very high centre of mass energy. At LHC Pb-Pb collisions have been performed at $\sqrt{s_{NN}} = 2.76$ TeV, which is the highest colliding energy so far for the heavy-ion collisions. It is believed that QGP can be created at very early stage of the heavy-ion collisions. Since the QGP is not expected in the p-p and p-Pb collisions, these have been performed to make a base line study for heavy-ions collisions. Besides this, the main goal of the p-p collisions at LHC is the search for the *"Higgs bosons"* and to study beyond the Standard Model. LHC has made the p-p collisions at $\sqrt{s}$ = 0.9 TeV to 8 TeV and p-Pb collisions at $\sqrt{s}$ = 5.02 TeV. In both cases LHC has achieved the highest colliding energy so far. Similar studies have been made in the other colliding experiments like Super Proton Synchrotron (SPS) at CERN and Relativistic Heavy Ion Collider (RHIC) at Brookhaven National Laboratory (BNL), USA.

1.5 Space time evolution of the heavy-ion collisions

Space time evolution of the high energy nucleus-nucleus collisions was first introduced by Bjorken in 1983 [11]. Bjorken estimated initial energy density in terms of rapidity density of the produced particles in central rapidity region.

We consider the head-on collision of two equal nuclei in the center-of-mass frame. Two Lorentz contracted nuclei come along z-direction with the speed of light and collide at z = 0 and t = 0. At vey high energies the baryons collide and move away

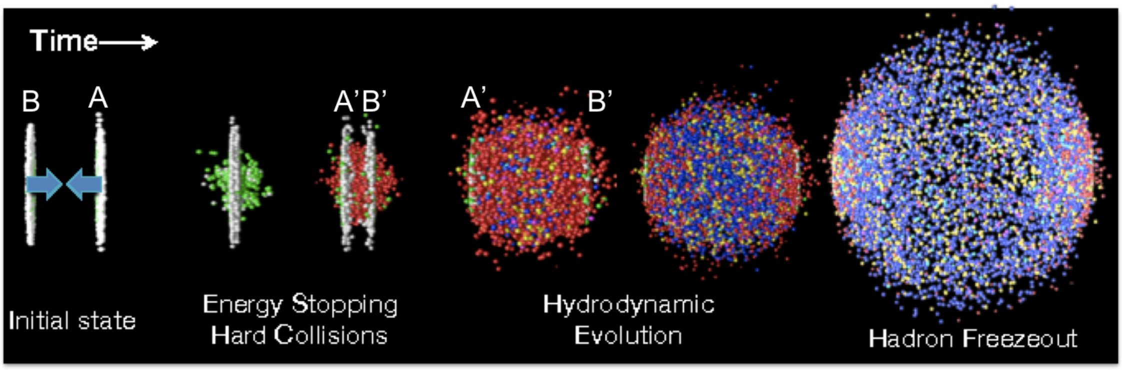

Figure 1.2: A schematic picture of heavy-ion collision.

from the region of collision as shown in the Fig. 1.2. Before the collision, the colliding baryon matters are denoted as A and B and after the collision, they are denoted as A' and B'. In this collision a large amount of energy is deposited in a small region of space in a short duration of time. The matter created in the collision region has a very high energy density, but small net baryon content. The energy density may be sufficiently high to make it likely that a system of quark-gluon plasma may be formed.

The plasma initially may not be in thermal equilibrium, but subsequent equilibration may bring it to local equilibrium at the proper time τ_0, and the plasma may then evolve according to the laws of hydrodynamics. As the plasma expands, its temperature drops down and the hadronization of the plasma will take place at a later proper time. The hadrons will stream out of the collision region when the temperature falls below the freeze-out temperature, which is called *"chemical freeze-out"*. After chemical freeze-out there is only elastic scattering between the hadrons. When the mean free path of the hadrons exceeds the dynamical size of the system there is no further interaction between the hadrons. This is called the *"Ki-*

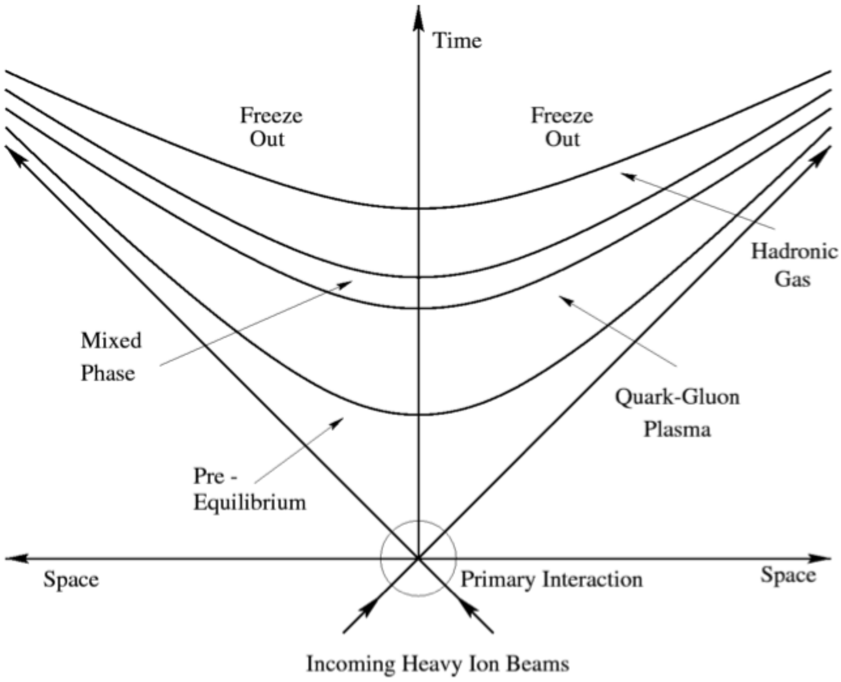

Figure 1.3: A schematic picture of the space time evolution of the heavy-ion collisions.

netic freeze-out" after which the hadrons stream out freely. Finally, these particles are detected in the detector.

1.6 Signatures of the QGP

The QGP cannot be detected directly as the information carried by the produced particles may be distorted while passing through the different stages of the collisions after QGP. According to the theory there are some proposed signatures of the QGP which can be measured in the experiments such as study of the nuclear modification factor of produce charged particles, strangeness enhancement, jet quenching, J/ψ suppression, particle yield modification etc. Some of these signatures are described below.

Most of the observables in heavy-ion (Pb-Pb) collisions are studied with respect to the systems where QGP is not expected like p-p and p-Pb collisions. One of the main observable is the *"nuclear modification factor"* (R_{AA}). It is defined as the ratios of yields in heavy-ion collisions and in p-p collisions normalized to the number of independent binary nucleon-nucleon collisions. It is found that for p-Pb collisions R_{pPb} is consistent with unity after $p_T \geq 2$ GeV/c while in central Pb-Pb collisions R_{PbPb} is much less than 1. It suggests that the strong suppression observed in central Pb-Pb collisions is not due to the initial-state effect but rather to a signature of QGP [12].

Another strong evidence of the QGP is the *"jet quenching"* in the heavy-ion collisions. In case of dijet production in heavy-ion collisions the away side jet traverse through the hot and dense medium and lose most of the energy or may even completely absorbed by the medium [13]. This effect is known as *"jet quenching"*. So the dijet asymmetry in heavy-ion collisions may provide the signature of the QGP.

Production of the J/ψ particles are suppressed in heavy-ion collisions with respect to the p-p collisions. J/ψ particle is the bound state of a charm quark (c) and a charm anti quark ($\bar{c}$). In presence of QGP the interaction between c and $\bar{c}$ becomes weak due to the *Debye screening*. Furthermore, in the QGP quarks and gluons are deconfined and the string tension between c and $\bar{c}$ vanishes. Because of these reasons, J/ψ particles production suppressed in presence of QGP. This phenomenon is known as *J/ψ suppression*, which has been observed in various experimental results [14].

Number of strange particles are enhanced in heavy-ion collisions in comparison with p-p collisions. It is believed that due to a drop in the strange quark's dynamical mass, strangeness in the QGP would equilibrate faster relative to those in a hadronic gas [15]. *Strangeness enhancement* has been clearly observed in various experiments [16].

1.7 p-p collisions

The main goal of the LHC is to search the Standard Model Higgs boson and to search the physics beyond the Standard Model. p-p collisions at very high centre of mass energy and at very high luminosity allow to explore this completely new regime. p-p collisions are also important to study the particle production mechanism. Besides these, p-p collisions serve very important references for heavy-ion measurements.

Proton-proton collisions can be divided into two processes (1) *elastic collisions* and (2) *inelastic collisions*. In case of elastic collisions no new particles are produced. Only the inelastic collisions are involved to produce the new particles after the collisions. Inelastic collisions consist of three different processes: (i) $single\ diffractive$ (SD), (ii) $double\ diffractive$ (DD) and (iii) $non\ diffractive$ (ND). The process where one particle gets excited and produces new particles and other particle remain same is called the SD process ($p_1+p_2 = p_1+X$ or $p_1+p_2 = X+p_2$). In DD process both the particles break up and produce new particles ($p_1 + p_2 = X_1 + X_2$). In ND process parton-parton interactions take place to produce the particles. The rapidity distributions of the charged particles have been shown in the Fig. 1.4 for three different processes. As experiments have limited capabilities to distinguish these processes the experimental results are generally published in two different classes: (a) *inelastic (INEL) (SD+DD+ND)* and (b) *Non-single diffractive (NSD)*. Recently ALICE experiment has measured the cross-section of the different processes at LHC energies. The values are presented in the table 1.3 [17].

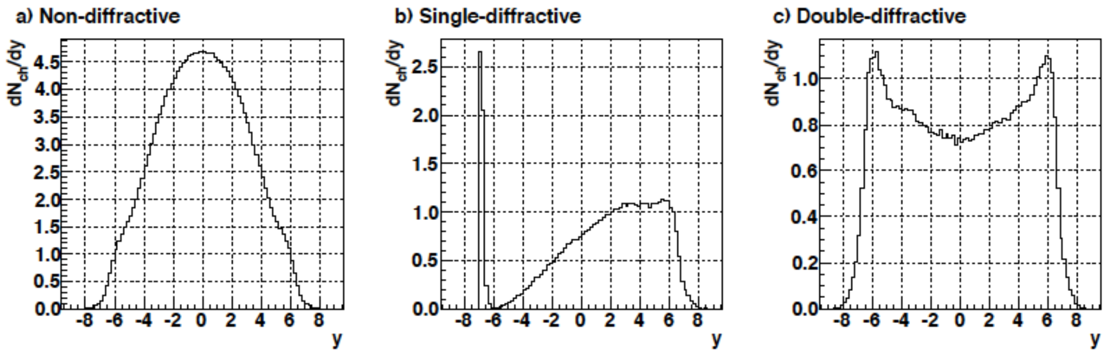

Figure 1.4: Rapidity distribution of the charged particles using PYTHIA at $\sqrt{s}$ = 0.9 TeV for ND, SD and DD processes. The figure has been taken from the ref [18].

$\sqrt{s}$ (TeV)	σ_{SD} (mb)	σ_{DD} (mb)
0.9	$11.2^{+1.6}_{-2.1}$	5.6 ± 2.0
2.76	$12.2^{+3.9}_{-5.3}$	7.8 ± 3.2
7	$14.9^{+3.4}_{-5.9}$	9.0 ± 2.6

Table 1.3: Cross-sections of the SD and DD processes at $\sqrt{s}$ = 0.9, 2.76 and 7 TeV [17].

Particle productions in the p-p collisions are measured in terms of pseudorapidity and multiplicity distributions of the produced particles. Pseudorapidity (or rapidity) distribution is the number of particles per unit pseudorapidity (or rapidity) i.e. $dN/d\eta$ (or dN/dy) vs. η (or y). Multiplicity distributions are presented as probability, $P(N)$, as a function of multiplicity (N) within available phase space. Scaling behavior of the multiplicity distribution is expressed as $< N > \times P(z)$ vs. z where $z = N/ < N >$. This scaling is called *"KNO-Scaling"* and z is called *"KNO variable"*. The energy dependence is studied by measuring the $dN/d\eta$ at $\eta = 0$ or the $< N >$ within the available acceptance as a function of $\sqrt{s}$.

There are various theoretical models and concepts that explain the multiplicity distributions of the final state particles produced in the p-p collisions. In 1969 Feynman postulated that average multiplicity of the produced particles are proportional to the $ln\sqrt{s}$. This is know as "Feynman scaling" [19].

$$< N > \propto ln\sqrt{s}, \tag{1.1}$$

Based on Feynman scaling Koba, Nielsen, and Olesen derived theoretically in 1972 that multiplicity distributions should follow so-called *KNO scaling* [20]. This law says that the quantity:

$$\psi(z) =< n > P(z) \tag{1.2}$$

is an energy independent function. Where z = $< n > /n$ and n is multiplicity of the produced particles.

Multiplicity distribution of the produced particle can be explained by a *"negative binomial distribution (NBD)"*. The NBD is defined as:

$$P(n; p; k) = \begin{pmatrix} n + k - 1 \\ n \end{pmatrix} (1 - p)^n p^k, \tag{1.3}$$

where 1/p = $1 + < n > /k$, $< n >$ is the average multiplicity and 'k' is a parameter responsible for the shape of the distribution [21, 22]. The distribution function can be written as:

$$P(n; m; k) = \frac{\Gamma(n + k)}{\Gamma(n + 1)\Gamma(k)} \frac{(m/k)^n}{(m/k + 1)^{n+k}} \tag{1.4}$$

where m = < n >; if $k \to \infty$ the distribution becomes Poissonian; if $k = 1$ the distribution becomes geometric;

It gives the probability of n failures and k-1 successes in n + k -1 trials and a success on the (n + k)th trial.

Giovannini and Ugoccioni introduced the double NBD function i.e. the combination of two NBDs [23]. This approach combines the the two classes of events: *soft* and *semi-hard*. The double NBD function can be expressed as:

$$P(n; m_1; k_1; m_2; k_2; W) = WP(n; m_1; k_1) + (1 - W)P(n; m_2; k_2), \tag{1.5}$$

where m_1, k_1 belong to soft processes and m_2, k_2 belong to semi-hard processes.

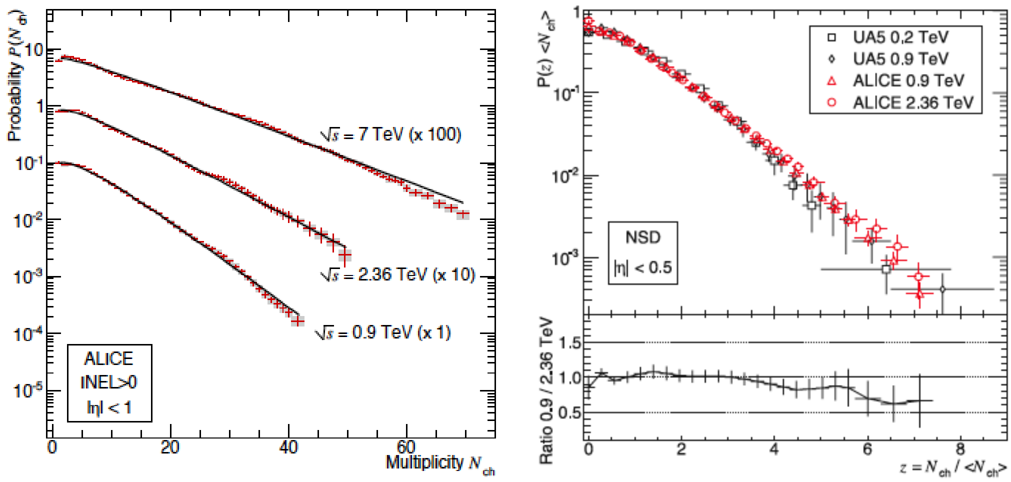

Figure 1.5: Left panel: Multiplicity distribution of charged particles within $|\eta| < 1$ with the NBD fit [24]. Right panel: Multiplicity distribution within $|\eta| < 0.5$ in terms of KNO variables from 0.2 to 2.36 TeV [25].

Left panel of the Fig. 1.5 shows the charged particle multiplicity distribution within $|\eta| < 1$ with NBD fits at $\sqrt{s} = 0.9$, 2.36 and 7 TeV from the ALICE experiment. It is observed that at 0.9 and 2.76 TeV multiplicity distributions are described well by the NBD, but at 7 TeV the NBD fit overestimates the data at high multiplicity [24]. The right panel of the Fig. 1.5 shows the multiplicity distribution in terms of KNO variables at $\sqrt{s}$ = 0.2, 0.9 and 2.36 TeV within $|\eta| < 0.5$. KNO scaling shows the reasonable description of the data from 0.2 to 2.36 TeV [25].

Measurement of the pseudorapidity density is also very important to study the *"limiting fragmentation (LF)"* behavior of the produced particles. The hypothesis of limiting fragmentation in high energy hadron-hadron collisions was suggested by J. Benecke et. al. in 1960s [26]. This hypothesis states that the produced particles, in the rest frame of one of the colliding hadrons, will approach a limiting distribution. Experimentally limiting fragmentation behavior is represented as a number of produced particles per unit pseudorapidity i.e. $dN/d\eta$ vs. $\eta - y_{beam}$, where y_{beam} is the beam rapidity. Limiting fragmentation behavior was observed both in p-p and heavy-ion collisions. Top panel of the Fig. 1.6 shows the centre of mass energy independent limiting fragmentation behavior in p-p collisions from 53 GeV to 1800 GeV [27]. Bottom panel of the Fig. 1.6 shows the energy independent LF behavior of both charged particles and photons in Au-Au collisions from 19.6 GeV to 200 GeV [28]. In the ref [28] it is also observed that the photons show centrality independent LF behavior where charged particles show centrality dependent LF behavior. In this point of view it will be very interesting to see the LF behavior of photons at LHC energies.

Limiting fragmentation behavior is also studied in the Color Glass Condensate (CGC) framework [29] and a reasonable agreement with the experimental data has been seen in the Fig. 1.7. In the ref [29] it is stated that *"Further detailed tests of limiting fragmentation at RHIC and the LHC will provide insight into the evolution*

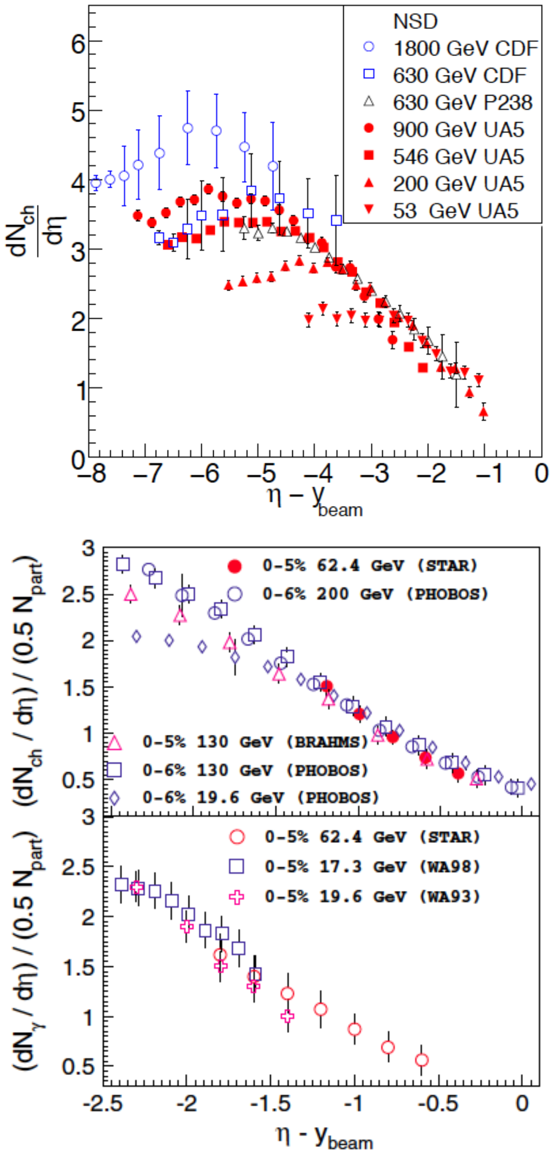

Figure 1.6: Upper panel: LF behavior of charged particles in p-p collisions for NSD events [27]. Lower panel: LF behavior of charged particles and photons in Au-Au collisions from STAR experiment [28].

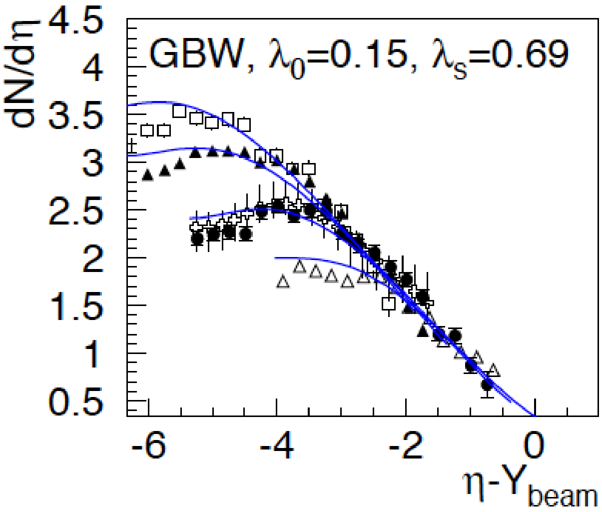

Figure 1.7: LF behavior is shown in CGC based model. The different symbols show the experimental data points in p-p collisions and solid lines represent the predictions from the CGC [29].

equations for high energy QCD".

1.8 Event generators

A direct comparison between theory and experiment can be made by the *event generators*. As the name indicates, event generators generate the event with exactly same format as the real data recorded by the detectors. Although the event generators are limited by the understanding of the existing underlying physics it plays very important role in various aspects of the high energy physics. It helps in the planning of a new detector, so that detector performance is optimized, within other constraints, for the study of new interesting physics scenarios. The analysis strategies that should be used on real data can be optimized using the event generators. Detector acceptance and efficiency corrections, which have to be applied to the *raw data*, in order to extract the true physics signal, are performed using the event generators. Comparing with the real data, it helps us to find the limitation of the existing underlying physics.

In the following subsections we will discuss four different event generators, which have been used in analysis of data presented in the thesis.

1.8.1 PYTHIA

PYTHIA [30, 31, 32] is a perturbative QCD (pQCD) based event generator, which can generate the simulated event for the collisions between the elementary particles such as e^-, e^+, p, $\bar{p}$ etc. In PYTHIA total proton-proton cross-section is the combination of *elastic*, SD, DD and ND processes. Among these, ND processes have the largest contribution to the total cross section. In PYTHIA each beam particle is characterized by a set of parton (q, $\bar{q}$, g) distributions, which defines the partonic substructure in terms of flavor composition and energy sharing. One shower initiator parton from each beam starts off a sequence of branching, such as $q \to qg$, which build up an initial-state shower before interaction. Hard processes such as $qg \to qg$, $qg \to q\gamma$ take place between the incoming partons and a number of outgoing partons are produced. It is the nature of this process that determines the main characteristics of the event. The cross-section for a process $ij \to k$ is given by

$$\sigma_{ij\to k} = \int dx_1 \int dx_1 f_i^1(x_1) f_i^2(x_2) \hat{\sigma}_{ij\to k} \tag{1.6}$$

Here $\hat{\sigma}$ is the cross section for the hard partonic process. The $f_i^a(x)$ are the parton-distribution functions, which describe the probability to find a parton 'i' inside beam particle 'a', with parton 'i' carrying a fraction 'x' of the total 'a' momentum. In addition to the hard process considered above, further semihard interactions may occur between the other partons of two incoming hadrons. The outgoing partons may branch, just like the incoming did, to build up final-state showers.

The fragmentation or hadronization process is governed by the *"Lund model"*. According to this model, as the q and $\bar{q}$ move apart, the potential energy stored in the string increases, and the string may break by the production of a new $q'\bar{q}'$ pair, so that the system splits into two colour-singlet systems $q\bar{q}'$ and $q'\bar{q}$. If the invariant mass of either of these string pieces is large enough, further breaks may occur. Finally, hadrons are produced.

1.8.2 PHOJET

In PHOJET [33, 34] event generator the total cross-section can be divided into *soft* and *hard* processes based on the momentum of the partons involved in the interaction. Soft processes are governed by the *Dual Parton Model (DPM)* [35] and the hard part is calculated using pQCD like in PYTHIA. The total cross-section can be written as:

$$\sigma_{tot} = \sigma_{soft} + \sigma_{hard} \tag{1.7}$$

Pomeron exchanges dominate the soft processes. The Pomeron exchange cross-section for pure soft interactions can be parametrized as [36]:

$$\sigma_{soft} = a s^{\alpha-1} \tag{1.8}$$

where a=37.08 mb and $\alpha = 1.076$. s is the centre of mass energy.

The soft interaction increases with the increase of centre of mass energy and violates the unitarity bound at higher energy. To preserve the unitarity bound multiple-Pomeron exchanges are taken into account.

The cross-section of the hard processes can be expressed as [36]:

$$\sigma_{hard} = \sum_{i,j \to k,l} \int\int\int dx_1 dx_2 d\bar{t} x_1 f_i(x_1, Q^2) \times x_2 f_i(x_2, Q^2) \frac{1}{x_1 x_2} \pi M^2 \frac{\alpha_s^2(Q^2)}{\hat{s}^2} \tag{1.9}$$

where $f_{i,j}(x_{1,2}, Q^2)$ are the parton distributions, $M = M_{1,j\to k,l}$ is the matrix element for the hard parton-parton scattering. $\alpha_s(Q^2)$ is the strong coupling constant.

Similar to the soft processes, a mechanism of multiple hard parton scattering must be adopted to preserve unitarity. Therefore PHOJET allows the possibility of having events with multiple soft interactions (multiple-Pomeron exchanges) and multiple hard parton scattering. The fragmentation process for both soft and hard interactions of PHOJET is governed by the *Lund model* as in PYTHIA.

In ALICE experiment PYTHIA and PHOJET event generators have been used to simulate the p-p collisions at different LHC energies.

1.8.3 HIJING

Monte Carlo (MC) event generator Heavy Ion Jet INteraction Generator (HIJING) was first introduced by M. Gyulassy and X.-N. Wang in 1991 [37]. It was developed combining pQCD inspired models for multiple jet production with low p_T multi-string phenomenology to study jet and multi-particle production in high energy p-p, p-A and A-A collisions. The model includes multiple mini-jet production with initial and final state radiation, nuclear shadowing of parton distribution functions and a schematic mechanism of jet interactions in dense matter. A model for jet quenching is included to enable the study of the dependence of moderate and high p_T observables on an assumed energy loss dE/dx of partons traversing the produced dense matter. Glauber geometry for multiple collisions is used to calculate p-A and A-A collisions. The formulation of the HIJING was guided by the Lund model and DPM for the soft interactions and the pQCD processes for the hard interactions. In ALICE experiment HIJING event generator has been used to simulate Pb-Pb and p-Pb collisions.

1.8.4 DPMJET

In DPMJET [38, 39, 40], the two-component Dual Parton Model is used with multiple soft chains and multiple mini-jets at each elementary interaction. Particle production is realized by the fragmentation of colorless parton-parton chains constructed from the quark content of the interacting hadrons. It includes the cascading of secondaries within the target as well as projectile nuclei, which is suppressed by the formation time concept. The excitation energy of the remaining target and projectile nuclei is calculated and using this nuclear evaporation is included into the model. DPMJET can be applied for hadron-hadron, hadron-nucleus, nucleus-nucleus and neutrino-nucleus interactions at high energies. DPMJET has been used to simulate p-Pb collisions in the ALICE experiment.

1.9 Study of the photon production

Inclusive photo production gives the complementary information of the charged particle production as most of the photons are the decay product of π^0 particles. So far, ALICE has been published the charged particles production in p-p collisions at mid rapidity [24, 25]. It will be very interesting to study the particle production in p-p collisions at forward rapidity as the particle production mechanism may be different at forward rapidity than that of mid rapidity. It is also of interest to see how particle production varies with centre of mass energy at forward rapidity. Comparing with existing models, study of photon production can provide important constrains to these models.

STAR experiment at RHIC provides the pseudorapidity density of the inclusive photons at forward rapidity region using Photon Multiplicity Detector (PMD) in Au-Au collisions at $\sqrt{s_{NN}} = 62.4$ GeV [28]. Fig. 1.8 shows the pseudorapidiy distributions of photons for different centrality classes. It is found that both the models, AMPT [41] and HIJING [37] explain the data well for central as well as peripheral collisions.

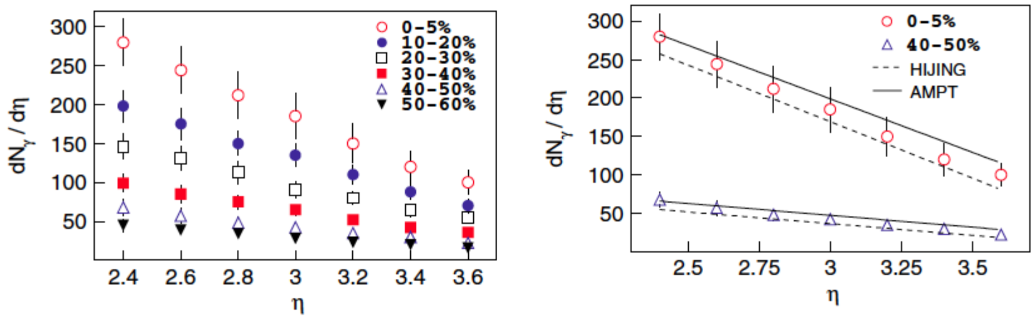

Figure 1.8: Left panel: pseudorapidity densities of photons for different centralities. Right panel: data points with the expectation from the models AMPT (solid line) and HIJING (dotted line) [28].

1.10 Study of the Forward-backward multiplicity correlation

It is believed that the correlations of the particles created at early stage of the collisions can spread over large rapidity intervals [42]. Thus, the measurement of Forward-backward (F-B) correlations over a large rapidity interval could provide some information about the initial stage of the collisions [43]. F-B correlations in p-p collisions give crucial information towards understanding of particle production mechanisms at different centre of mass energies as well as provide the strong base line for heavy-ion collisions.

F-B multiplicity correlations were measured in different systems like p-p, p-$\bar{p}$ and Au-Au in various experiment such as ISR, E735, UA5 and STAR. The first measurement of the F-B correlation was done in ISR experiment at 1978 at $\sqrt{s}$ = 24, 31, 45, 53 and 63 GeV within $|\eta| < 3.6$ [44]. They investigated the average charged particle multiplicity $< n_B >$ in different rapidity intervals of the backward hemisphere as a function of the multiplicity n_F in the corresponding intervals of the forward hemisphere. It was found that average backward multiplicity $< n_B >$ increases linearly with the forward multiplicity n_F and can be expressed as [44]:

$$n_B = a + bn_F \tag{1.10}$$

where the slope *'b'* measures the strength of the correlation between the forward and backward interval. It was found that a linear rises of *'b'* with the $\ln\sqrt{s}$ [44].

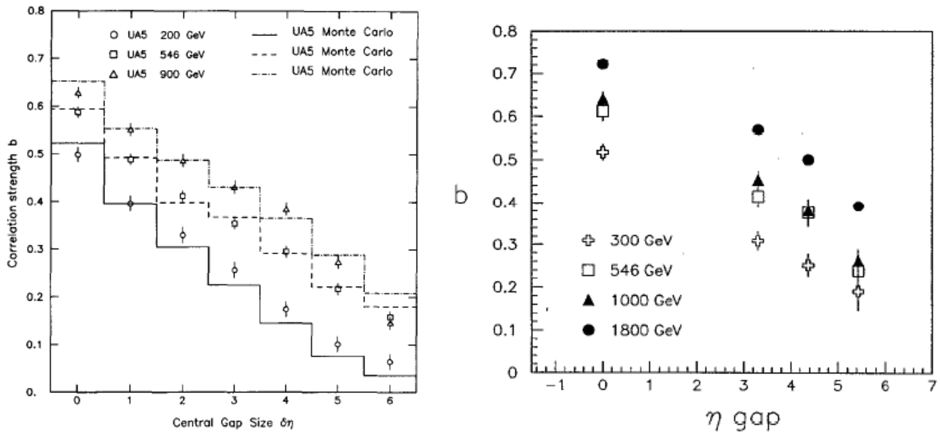

Figure 1.9: Left panel: correlation strength as a function of η *gap* from UA5 experiment [45]. Right panel: correlation strength as a function of η *gap* from E735 experiment [46].

UA5 experiment studied the F-B correlation strength as a function of η *gap* i.e. the distance between the forward and backward η windows at $\sqrt{s}$ = 200, 546 and 900 GeV in p-$\bar{p}$ collisions [45]. It was found (Fig. 1.9) that correlation strength 'b' deceases with increasing the η *gap* between the two windows. Similar study was also performed in the E735 experiment [46] and a very strong dependence of 'b' on the η *gap* had been found (Fig. 1.9).

STAR experiment studied the F-B correlations in Au-Au 200 GeV as well as in

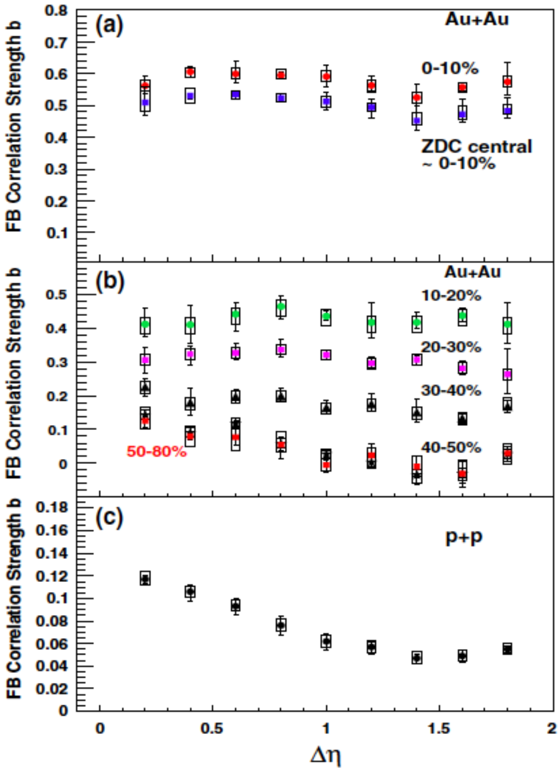

Figure 1.10: Correlation strength as a function of η *gap* ($\Delta\eta$) in Au-Au collisions (upper two panels) and p-p collisions (lower panel) [47].

p-p 200 GeV. The correlation strength 'b' was defined as [47]:

$$b = \frac{\langle N_f N_b \rangle - \langle N_f \rangle \langle N_b \rangle}{< N_f^2 > - < N_f >^2} = \frac{D_{\mathrm{bf}}^2}{D_{\mathrm{ff}}^2}, \tag{1.11}$$

where D_{ff}^2 and D_{bf}^2 are the forward-forward and backward-forward dispersions.

The results were presented as a function of η *gap* for different centrality classes in the Fig. 1.10 and strong long range correlation has been observed in the most central collisions. Whereas the behavior of correlation strength as a function of η *gap* in most peripheral collisions were found to very similar with the same energy p-p collisions.

1.11 Organization of the thesis

The work presented in the thesis can be divided in two parts - photon production at forward rapidity region and forward-backward multiplicity correlations of charged particles at central rapidity region. Outline of the thesis is the following:

Chapter 1 introduces the theoretical aspects of measurement of photon multiplicity and F-B multiplicity correlations. In *chapter 2* there is a brief description of Large Hadron Collider (LHC) along with ALICE experiment. Each sub-detector of ALICE is described in this chapter. Detailed description of the Photon Multiplicity Detector (PMD) along with the module testing is given in the *chapter 3*. Measurement of photon multiplicity and pseudorapidity density in p-p collisions using the PMD are described in *chapter 4*. In this chapter, each step of the analysis procedure is discussed and finally results are presented with different model predictions. Photon production in p-Pb collisions using the PMD is discussed in *chapter 5*. *Chapter*

6 introduces the measurement of forward-backward multiplicity correlations in p-p collisions at LHC energies using the central barrel of ALICE. In *chapter 7*, different methods for studying the F-B multiplicity correlations in heavy-ion collisions are discussed. In *chapter 8*, the work presented in this thesis is summarized.

2 The Large Hadron Collider and the ALICE experiment

In this chapter a brief description of the Large Hadron Collider (LHC) and the ALICE experiment are presented. A short overview and physics goals of all the detectors involved in the ALICE experiment are described.

2.1 The Large Hadron Collider (LHC)

The LHC at CERN [1, 2] is the largest particle accelerator in the world. The LHC project started inside the tunnel of the Large Electron Collider (LEP) in 2001. The LHC is located under the Swiss - French border area at a depth of 50 to 175 m. It has the circumference of approximately 27 Km.

LHC is designed to collide proton beams up to $\sqrt{s} = 14$ TeV and lead ion beam up to $\sqrt{s_{NN}} = 5.5$ TeV. Its design luminosity is $10^{34} cm^{-2} s^{-1}$ for proton beam and $10^{27} cm^{-2} s^{-1}$ for lead ion beam. For the ALICE experiment LHC can provide a lower luminosity of about 3×10^{30} during the p-p collisions.

The schematic layout of the LHC is shown in the Fig. 2.1. It consists of two superconducting rings and it is segmented into eight octants. Each octant has a straight section in its center, which is called *points*. Beams cross only at four points i.e. 1, 2, 5, and 8 out of the eight points. Particles are injected into outer arcs upstream of points 2 and 8. The Radio-frequency system which accelerates the particles is located at point 4 and the beam dumping system is located at point 6. Collimation systems are placed at point 3 and 7 to clean the beam. The cleaning prevents particles from being lost in an uncontrolled fashion within the accelerator. A total of 1232 dipole magnets, each 14.3 m length, are used to bend the beams and 392 quadrupole magnets, each 5 - 7 m long, are used to focus the beams.

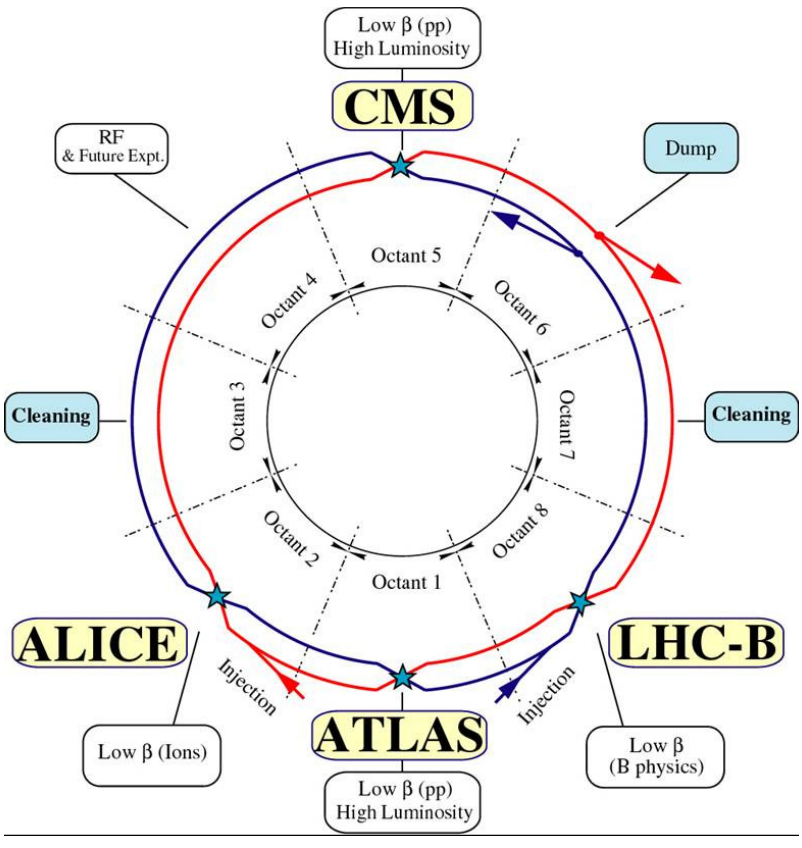

Figure 2.1: A schematic view of the LHC.

A schematic of the CERN accelerator complex is shown the Fig. 2.2. There are six experiments installed at the LHC: A Large Ion Collider Experiment (ALICE), A Toroidal LHC ApparatuS (ATLAS), the Compact Muon Solenoid (CMS), the Large Hadron Collider beauty (LHCb) experiment, the Large HadronCollider forward (LHCf) experiment and the TOTal Elastic and diffractive cross section Measurement (TOTEM) experiment.

ALICE [48, 49] is at point 2. It is specialized for heavy-ion collisions. It explores the properties of quark-gluon plasma, a state of matter where quarks and gluons, under conditions of very high temperatures and densities, are no longer confined inside hadrons. ALICE also studies the proton proton collision as a base line for heavy ion measurements and it is complementary to other LHC experiments.

ATLAS and CMS [50, 51] are at point 1 and Point 5 respectively. These two detectors are general-purpose proton - proton detectors designed to cover the wide range of physics at LHC, from the search for the Higgs boson to supersymmetry (SUSY) and extra dimensions. Both experiments are with the same physics goals, but different technical solutions and design.

LHCb [52] specializes in the study of the slight asymmetry between matter and antimatter present in interactions of B-particles (particles containing the b quark).

LHCf [53] shares the point 1 with ATLAS. It measures the particles produced very close to the direction of the beams in the proton-proton collisions at the LHC. The motivation is to test models used to estimate the primary energy of the ultra high-energy cosmic rays.

TOTEM [54] is located within the CMS detector. It measures the cross-section of the proton at LHC. To do this TOTEM must be able to detect particles produced

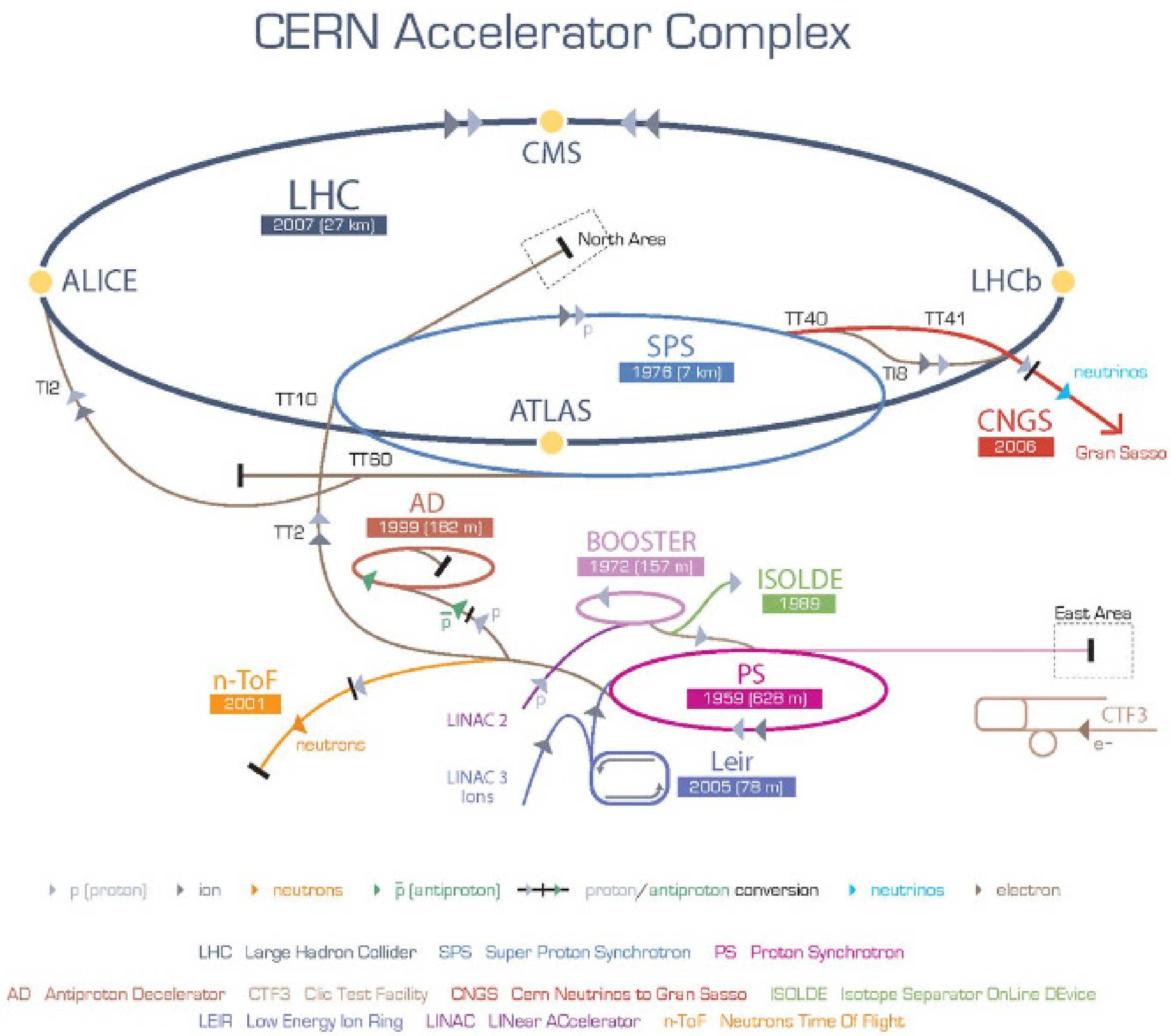

Figure 2.2: A schematic view of the CERN accelerator complex.

very close to the LHC beams. It includes detectors housed in specially designed vacuum chambers called Roman pots, which are connected to the beam pipes in the LHC.

The protons used in the p-p collision are obtained by removing electrons from hydrogen atoms in the linear accelerator (LINAC 2). They are injected from LINAC 2 into the BOOSTER at 50 MeV. The BOOSTER accelerates them to 1.4 GeV and sends to the Proton Synchrotron (PS), which further accelerates the protons to 25 GeV. From the PS they are sent to the Super Proton Synchrotron (SPS), where they are accelerated further to 450 GeV. From the SPS the proton beam is split into bunches traveling the LHC ring either clockwise or counter-clockwise. The bunches of protons are then accelerated to their expected reachable energy, and made to collide at the location of the four experiments ALICE, ATLAS, CMS and LHCb.

To accelerate the lead ions the procedure is similar. A highly purified lead sample is heated to produce the lead ions which are dominated by Pb^{27+} and are accelerated in LINAC 3 to 4.2 MeV per nucleon. These are passed through a carbon foil to get Pb^{54+} ions, which is lead to the Low Energy Ion Ring (LEIR) which accelerates them to 72 MeV per nucleon and sends to the PS where another acceleration is made to achieve 5.9 GeV per nucleon. The ions once again are sent through a foil to get Pb^{82+} and lead to SPS, where they are accelerated to 177 GeV per nucleon. Afterwards the ions are split into bunches and reaches into the LHC ring.

We got the first collisions of protons beam at $\sqrt{s} = 0.9$ TeV on 23^{rd} November 2009. After that the LHC has made the proton - proton collisions at $\sqrt{s} = 7$ TeV and $\sqrt{s} = 2.76$ TeV. The current top energy is $\sqrt{s} = 8$ TeV for p-p collisions and $\sqrt{s_{NN}} = 2.76$ TeV for Pb-Pb collisions. Also, in January 2013 the p-Pb collisions have been taken place at $\sqrt{s_{NN}}$= 5.02 TeV. The LHC will be shut down for a full year in 2013 for preparing to achieve the highest design energy.

2.2 The ALICE detector system

ALICE is a general-purpose, heavy-ion detector at the CERN LHC. It is designed to explore the physics of strongly interacting matter and quark-gluon plasma (QGP) at extreme condition in nucleus-nucleus collisions. It also takes the data during proton-proton collisions to do the complementary study with the other LHC detectors as well as provides the reference to the heavy ion collisions.

The design was optimized for $dN_{ch}/d\eta$ up to 4000 but tested up to 8000. The uniqueness of the ALICE detector is in the tracking and identifying the particles over a large momentum range (10 MeV/c to 100 GeV/c). This allows us to study from soft to jet physics.

The general layout of the ALICE detectors are shown in the Fig. 2.3. It consists of 16 detectors which can be separated into three main sections : central detectors, forward detectors and the Muon spectrometer [55]. The central barrel consists of the ITS, TPC, TRD, TOF, PHOS, EMCAL, HMPID and ACORDE [56] - [63]. The forward detectors include PMD, FMD, V0, T0 and ZDC [64] - [66] . With these detectors ALICE has a large η coverage, which is shown in the Fig. 2.4. A brief description of all the sub-detectors are given in the next section. In this thesis, the data from PMD are analyzed to study the photon production in forward rapidity region and the data from TPC and ITS are used to study multiplicity correlations.

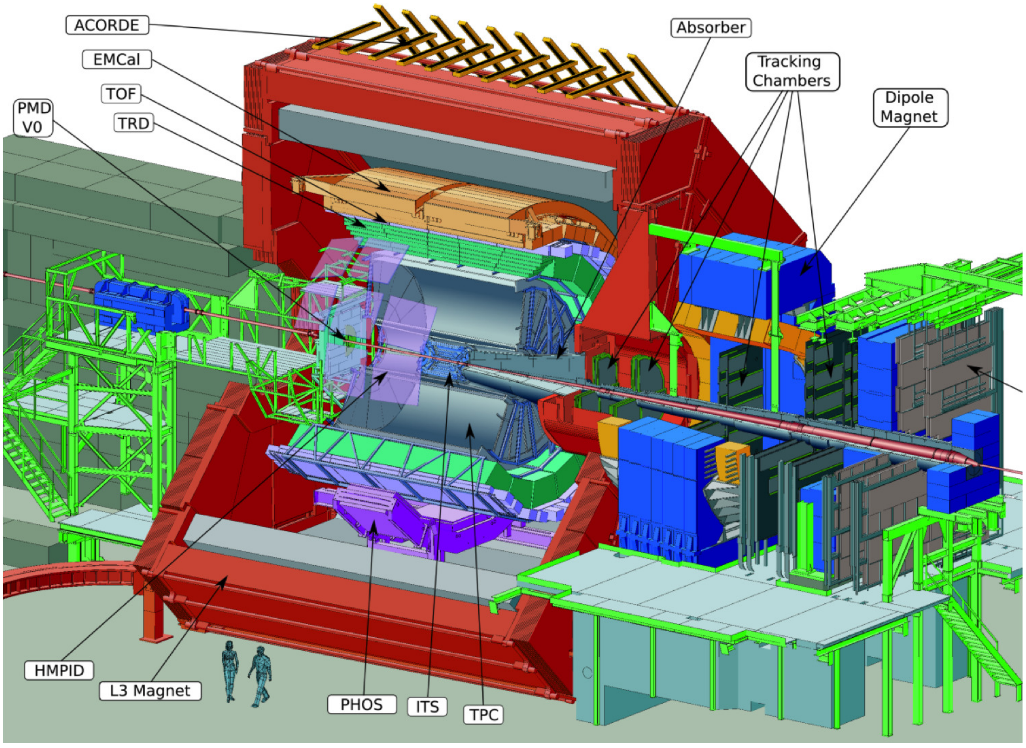

Figure 2.3: A schematic view of the ALICE detectors.

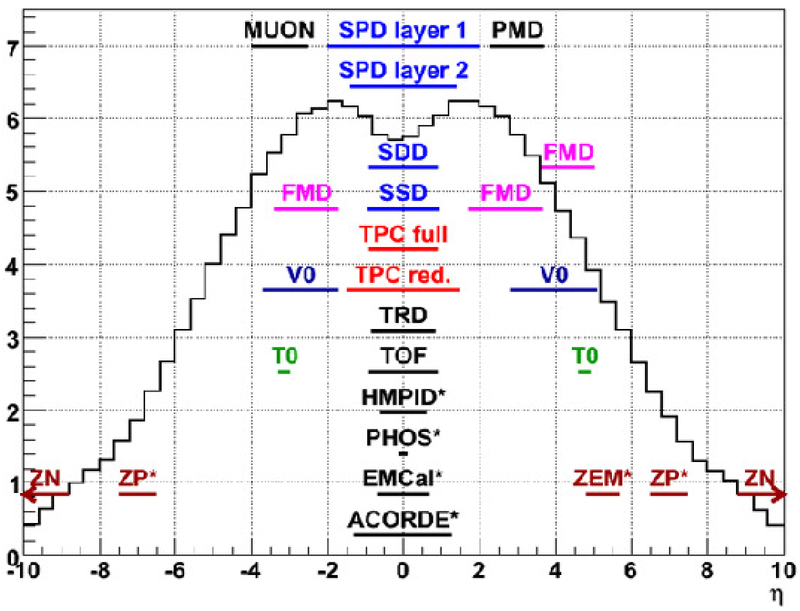

Figure 2.4: pseudorapidity coverages of different sub-detectors of the ALICE. All have the full azimuthal coverage except that have the marked with an asterisk.

2.2.1 The ALICE coordinate system

The ALICE coordinate system is shown in the Fig. 2.5 The interaction point is shown as an origin x=y=z=0. The z-axis is along the beam direction. The x-axis is perpendicular to the beam direction and pointing to the accelerator centre. The y-axis is the perpendicular to the x-axis and pointing upward. An observer looking to positive z has the accelerator center on the left. The PMD is in the positive z direction and the Muon spectrometer is at negative z. The polar angle θ increases from +z to -z. The azimuthal angle ϕ increases clockwise from x-axis passing through y-axis finally coming back to the x-axis.

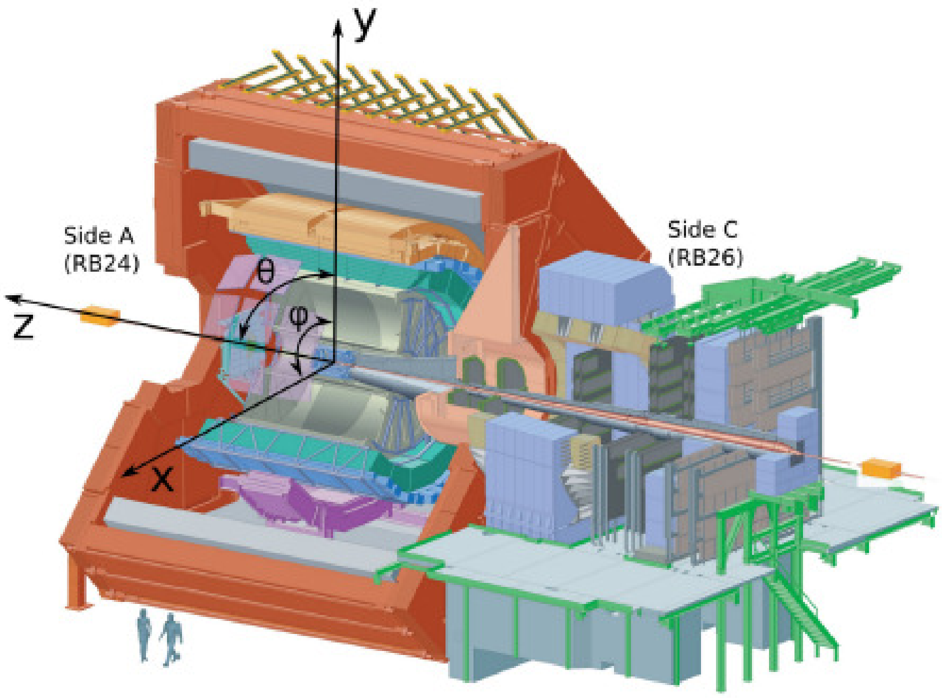

Figure 2.5: The ALICE coordinate system.

2.3 The central barrel detectors

A set of the detectors (ITS, TPC, TRD, TOF) covers the midrapidity region ($|\eta|$ <0.9) of the ALICE. It is enclosed in the L3 solenoid, which has an internal length of 12.1 m and a radius of 5.75 m. These are for tracking and particle identification in the very high multiplicity environment. Additional detectors like HMPID, EMCAL and PHOS are located in the central region with smaller phase space than the other central detectors mentioned earlier.

2.3.1 The Inner Tracking System (ITS)

The ITS [56] is a six layer silicon detector system with the radii from 3.9 to 43 cm. This is the closest detector to the interaction point (IP).

The ITS consists of three subsystems. Starting from the central to the peripheral these are Silicon Pixel Detector (SPD), Silicon Drift Detector (SDD) and Silicon Strip Detector (SSD) (Fig. 2.6).

Silicon Pixel Detector (SPD) [56] constitutes the two innermost layers of the ITS. It determines the position of the primary vertex as well as for the measurement of the impact parameter of secondary tracks originating from the weak decays of strange, charm, and beauty particles. The SPD is based on hybrid silicon pixels, consisting of a two-dimensional matrix (sensor ladder) of reverse-biased silicon detector diodes. There is no energy loss information is available and the readout is binary i.e. either there is a hit or there is not. The signals from this detector are used to measure the charged particle multiplicity within $|\eta|$ <2.1.

Silicon Drift Detector (SDD) [56] constitute the two intermediate layers of the ITS. It consist of a 300 μm thick layer of homogeneous high-resistivity silicon.

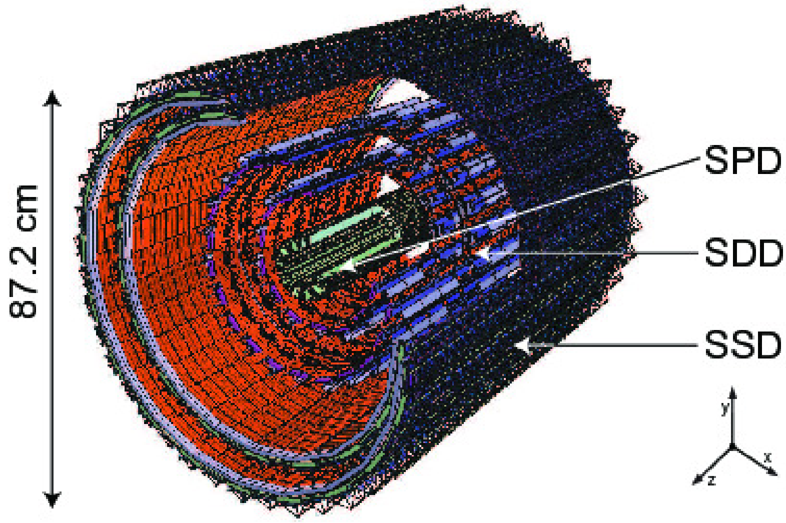

Figure 2.6: A schematic view of the ITS.

It provides the dE/dx information for particle identification.

Silicon Strip Detector (SSD) [56] It is the outer most layer of the ITS and important for the matching of the tracks from the TPC to the ITS. It provides a two dimensional measurement of the track position. In addition it provides dE/dx information to assist particle identification for low-momentum particles. The system is optimized for low mass in order to minimize multiple scattering.

As a whole ITS perform as a trigger detector. It determines the primary collision vertex and the secondary vertices, necessary for the reconstruction of charm and hyperon decays. It is also used as a particle identification and tracking of the low momentum particles. It also improves the momentum and angle resolution in combination with the TPC.

2.3.2 The Time Projection Chamber (TPC)

Time projection Chamber [57] is the largest sub-detector in the ALICE. It is the main tracking detector covering the phase space in pseudorapidity, $|\eta| < 0.9$, for tracks with full radial track length (matches in ITS, TRD, and TOF detectors); for reduced track length (at reduced momentum resolution), an acceptance up to about $|\eta| <= 1.5$ is accessible. The TPC covers the full azimuth (with the exception of the dead zones). A large p_T range is covered from low p_T of about 100 MeV/c up to 100 GeV/c with good momentum resolution. It also provides the particle identification via dE/dx measurements and determines the vertex positions.

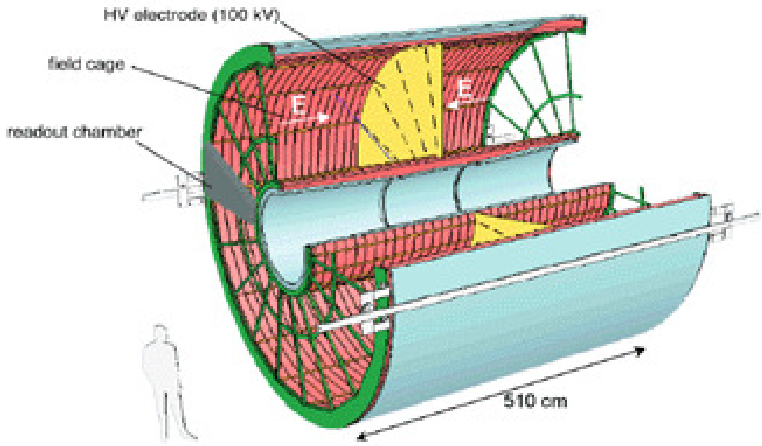

Figure 2.7: A schematic view of the TPC.

Fig. 2.7 shows a schematic view of the TPC. It is a gas detector with a volume of 90 m^3 and has a length of 5 m. It is filled with a $Ne/CO_2/N_2$ (90/10/5) gas mixture. A high voltage of 100 kV is applied between the central electrode and the two read out plates at a distance of $\pm$ 2.5 m from the z = 0 position. It results the maximum drift time of about 90 μs, which makes TPC the slowest detector in ALICE. The

TPC readout consists of multi-wire proportional chambers with cathode readout which comprises about 560 000 channels. Fig. 2.8 shows the reconstructed tracks in an event from Pb-Pb collisions in ALICE.

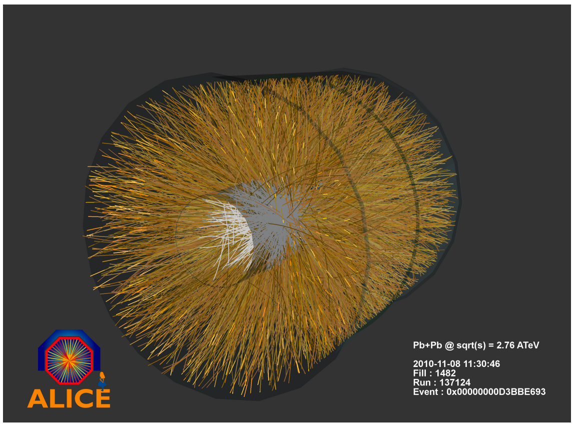

Figure 2.8: The event display showing large number of tracks within the TPC volume.

2.3.3 The Transition-Radiation Detector (TRD)

The main purpose of the ALICE Transition Radiation Detector (TRD) [58] is to provide electron identification in the central barrel for momenta above 1 GeV/c. Below this momentum electrons can be identified via specific energy loss measurement in the TPC. Above 1 GeV/c transition radiation (TR) from electrons passing a radiator can be exploited in concert with the specific energy loss in a suitable gas mixture to obtain the necessary pion rejection capability. The TRD is designed to produce a fast trigger for high momentum charged particles. It is a part of level 1 trigger and can significantly enhance the recorded Υ - yields, high-p_T J/ψ, the high-mass part of the dilepton continuum as well as jets.

The TRD is located at radii of 2.9 to 3.68 m with the pseudorapidity coverage of $|\eta| < 0.84$. It consists of 540 individuals read out detectors modules which are arranged into 18 super modules each of them containing 30 modules. Ionizing radiation produces electrons in the counting gas (X_e/CO_2 (85 : 15)). Particles exceeding the threshold for transition radiation production ($\gamma \approx 1000$) will in addition produce about 1.45 X-ray photons in the energy range of 1 to 30 keV. X-rays in this energy regime are efficiently converted by the high-Z counting gas with the largest conversion probability at the very beginning of the drift region. All electrons from ionization energy loss and X-ray conversions will drift towards the anode wires. After gas amplification in the vicinity of the anode wires, the signal is induced on the readout pads.

2.3.4 The Time-of-Flight detector (TOF)

The main goal of the ALICE Time-of-Flight detector [59] is to identify the charged particles in the intermediate momentum range. The TOF, coupled with the ITS and TPC for track and vertex reconstruction and of dE/dx measurements in the low momentum range (< 1GeV/c), provides event-by-event identification of large sample of pions, kaons and protons.

The TOF is located at radii from 2.7 to 3.99 m and covers a pesudorapidity region of $|\eta| < 0.9$. It is a gas detector based on Multi-gap Resistive Plate Chamber (MRPC). The TOF consists of 90 modules. Every module of the TOF detector consists of a group of MRPC strips (15 in the central, 19 in the intermediate and external modules) closed inside a box that defines and seals the gas volume and supports the external front-end electronics and services. The front-end electronics for the TOF are designed to comply with the basic characteristics of the MRPC detector, i.e. very fast differential signals from the anode and cathode readout pads and intrinsic time resolution better than 40 ps.

2.3.5 The Photon Spectrometer (PHOS))

The Photon Spectrometer [60] is a high-resolution electromagnetic spectrometer covering a limited acceptance of $|\eta| < 0.12$. The main physics objectives are the test of thermal and dynamical properties of the initial phase of the collision extracted from low p_T direct photon measurements and the study of jet quenching through the measurement of high p_T π^0 and γ - jet correlations.

The PHOS is high-granularity electromagnetic spectrometer consisting of a highly segmented electromagnetic calorimeter (PHOS) and a Charged-Particle Veto (CPV) detector. It is positioned on the bottom of the ALICE setup at a distance of 460 cm from the interaction point. Each PHOS module is segmented into 3584 detection cells arranged in 56 rows of 64 cells. The detection cell consists of a $22 \times 22 \times 180$ mm^3 lead-tungstate crystal, coupled to 5×5 mm^2 Avalanche Photo-Diode (APD) followed by a low-noise preamplifier.

2.3.6 The Electromagnetic Calorimeter (EMCal)

The Electromagnetic Calorimeter [61] is a large Pb-scintillator sampling calorimeter with cylindrical geometry, located adjacent to the ALICE magnet coil at a radius of $\sim$ 4.5 m from the beam line. It cover the pseudorapidity region of $|\eta| < 0.7$, and is positioned approximately opposite in azimuth to the high-precision ALICE Photon-Spectrometer (PHOS) calorimeter.

The EMCal is designed to explore in detail physics of jet quenching (interaction of energetic partons with dense matter) over the large kinematic range accessible in heavy-ion collisions at the LHC.

2.3.7 The High-Momentum Particle Identification Detector (HMPID)

The High-Momentum Particle Identification Detector [62] is dedicated to measure the identified hadrons at $p_T > 1$ GeV/c. The aim is to enhance the PID capability of ALICE by enabling identification of charged hadrons beyond the momentum interval attainable through energy-loss (in ITS and TPC) and time-of-flight measurements (in TOF). The detector was optimized to extend the useful range for π/K and K/π discrimination, on a track-by-track basis, up to 3 GeV/c and 5 GeV/c, respectively.

The HMPID is based on proximity-focusing Ring Imaging Cherenkov (RICH) counters and consists of seven modules of about 1.5×1.5 m^2 each, mounted in an independent support cradle. The radiator, which defines the momentum range covered by the HMPID, is a 15 mm thick layer of low chromaticity C_6F_{14} (perfluorohexane) liquid with an index of refraction of n = 1.2989 at $\lambda = 175$ nm corresponding to $\beta_{min} = 0.77$. Cherenkov photons, emitted by a fast charged particle traversing the radiator, are detected by a photon counter which exploits the novel technology of a thin layer of CsI deposited onto the pad cathode of a Multi-Wire Pad Chamber (MWPC). The HMPID, with a surface of about 11 m^2, is the largest scale application of this technique.

2.3.8 The ALICE Cosmic ray Detector (ACORDE)

ACORDE [63] is the cosmic ray detector, is an array of plastic scintillator counters placed on the upper surface of the L3 magnet. It plays a two-fold role in ALICE : i) the first task is to provide a fast (Level-0) trigger signal, for the commissioning, calibration and alignment procedures of some of the ALICE tracking detectors; ii) it can also detect, in combination with the TPC, TRD and TOF, single atmospheric muons and multi-muon events (so-called muon bundles). It allows us to study high-energy cosmic rays.

The detector is located at the radial position of 8.5 m with the pesudorapidity coverage of $|\eta| < 1.3$. An ACORDE module consists of two scintillator counters, each with 190×20 cm^2 effective area, placed on top of each other and read out in coincidence. The ACORDE scintillator module array, which includes 60 scintillator counter modules placed on top of the ALICE magnet. ACORDE provides a fast Level-0 trigger signal to the Central Trigger Processor, when atmospheric muons impinge upon the ALICE detector. The signal is used for the calibration, alignment and performance of several ALICE tracking detectors, mainly the TPC, TOF, HMPID and ITS. The operational Cosmic Ray Trigger is delivering trigger signals independent of the LHC beam.

2.4 The Forward detectors

2.4.1 The Photon Multiplicity Detector (PMD)

The Photon Multiplicity Detector [64] in ALICE is designed to measure the inclusive photon multiplicity in the forward rapidity ($2.3 < \eta < 3.9$) with the full ϕ coverage. It is situated 367 cm away from the interaction point opposite to the Muon spectrometer.

The detector consists of a Preshower plane, Charged Particle Veto plane (CPV) and a lead converter of thickness $3X_0$ which is sandwiched between the two planes. The two planes are the identical gas proportion chambers. The photons produce shower of electrons and positrons while crossing through the detectors and the shower particles produce signals in the Preshower plane. More details of the PMD will be discussed in Chapter 3.

2.4.2 The Forward Multiplicity Detectors (FMD)

The Forward Multiplicity Detector [65] is designed to provide charged particles multiplicity in the wide range of pseudorapidity region like -3.4 $< \eta <$ -1.7 and $1.7 < \eta < 5.0$. The FMD consists of 3 groups of detectors called FMD1, FMD2, and FMD3. FMD2 and FMD3 each consists of a ring of inner type Si sensors and a ring of outer type Si sensors. These are located on either side of the IP. FMD1 consists of a ring of inner type Si sensors and it is placed opposite to the muon spectrometer to extend the charged particle multiplicity coverage.

The information from FMD can also be used to study the event-by-event multiplicity fluctuation, determination of reaction plane, and elliptic flow measurement within its pseudorapidity coverage. In conjunction with PMD, FMD can also be used to study the correlation between photons and charged-particles at forward rapidity.

2.4.3 The V0 detector

In ALICE, V0 detector [65] has several functions. It provides minimum-bias triggers for the central barrel detectors. It rejects the beam-gas events and provide a pre-trigger to the TRD. The V0 serves as an indicator of the centrality of the collision via the multiplicity recorded in the event. This detector also participates in the measurement of luminosity in p-p collisions with a good precision of about 10%.

The V0 detector is a small angle detector consisting of two arrays of scintillator counters, called V0A and V0C, which are installed on either side of the ALICE interaction point. V0A is located 340 cm from the vertex on the side opposite to the muon spectrometer whereas V0C is fixed to the front face of the hadronic absorber, 90 cm from the vertex. They cover the pseudorapidity ranges -3.7 $< \eta <$ -1.7 (VOC) and 2.3 $< \eta <$ 5.1 (V0A) and are segmented into 32 individual counters each distributed in four rings.

2.4.4 The T0 detector

The T0 (time-0) detector [65] is a timing detector with high resolution. It can measure the collision time with a precision of 25 ps. If the vertex position is inside a window where interactions are expected an L0 trigger is issued. A vertex position outside the region where collisions should appear is used as a beam-gas rejection signal. The T0 can also generate an early wake-up signal to the TRD, prior to L0.

The detector consists of two arrays of Cherenkov counters, 12 counters per array. Each Cherenkov counter is based on a photomultiplier tube PMT-187, 30 mm in diameter, 45 mm long. Each PMT is optically coupled to a quartz radiator 20 mm in diameter and 20 mm thick. One of the arrays, T0-C is placed 72.7 cm from the nominal vertex. The pseudo-rapidity range of T0-C is -3.28 < η < -2.97. On the opposite side of the IIP, the distance of the other array (T0-A) is about 375 cm and covers the pseudorapidity range of 4.61 < η < 4.92.

2.4.5 The Zero-Degree Calorimeter (ZDC)

The ZDC [66] is designed to detect the spectators nucleons by measuring the energy carried by them in the forward direction (at 0^0 relative to the beam direction). The centrality information provided by the ZDC is also used for triggering at Level 1. The ZDC being also a position-sensitive detector, can give an estimate of the reaction plane in nuclear collisions.

In ALICE two sets of hadronic ZDCs are located at 116 m on either side of the Interaction Point. In addition, two small electromagnetic calorimeters (ZEM) are placed at about 7 m from the IP, on both sides of the LHC beam pipe, opposite to the muon arm. Spectator protons are spatially separated from neutrons by the magnetic elements of the LHC beam line. Therefore, each ZDC set is made by two distinct detectors: one for spectator neutrons (ZN), placed between the beam pipes at 0^0 relative to the LHC axis, and one for spectator protons (ZP), placed externally to the outgoing beam pipe on the side where positive particles are deflected.

2.5 The Muon Spectrometer

The muon spectrometer [55] is designed to detect muon in the polar angular range $171^0 - 178^0$ and in pseudorapidity range -4.0 < η < -2.5. It is located at -ve z direction of the ALICE experiment. It provides the measurement of the complete spectrum of quarkonia (J/ψ, ψ', Υ, Υ', Υ'') as well as the ϕ meson using the $\mu^+\mu^-$ decay channel.

The spectrometer consists of the following components: a passive front absorber to absorb hadrons and photons from the interaction vertex; a high-granularity tracking system of 10 detection planes; a large dipole magnet; a passive muon-filter wall, followed by four planes of trigger chambers; an inner beam shield to protect the chambers from primary and secondary particles produced at large rapidities. The tracking system is made of 10 cathode strip chambers arranged in 5 stations of 2 chambers each. Four planes of Resistive Plate Chambers (RPCs) arranged in 2 stations and positioned behind a passive muon filter provide the transverse momentum of each muon. The spatial resolution is better than 1 cm and the time resolution is 2 ns.

2.6 The ALICE Trigger System

The ALICE Trigger system consists of a two types of triggers : The low-level hardware trigger called Central Trigger Processor (CTP) and the High-Level Trigger (HLT) which is the software trigger.

2.6.1 The Central Trigger Processor (CTP)

The CTP combines the trigger signals from the different sub-detectors to decide if an event is accepted. It provides several levels of hardware triggers. The first level called Level-0 (L0), is delivered after 1.2 μs, the second, called Level-1 (L1), after 6.5 μs. The final trigger, which is called Level-2 (L2) trigger is delivered after 100 μs.

After the Level-2 trigger the event is stored. The CTP consists of 24 Local Trigger Units (LTU) for each detector systems. The output from the CTP go to the LTUs of each detector and then to the front-end electronics to the detectors via LVDVS cables and optical fibers. The CTP forms 50 independent trigger classes combining 24 L0 inputs, 24 L1 inputs and 12 L2 inputs [67].

In ALICE information from the V0 detector and SPD detector are combined to form the **Minimum-Bias triggers** which is designed to trigger on all inelastic interactions. A set of minimum-bias triggers are available: MB1 (($V0_{OR}$ or SPD_{OR}) and not $V0_{BG}$), MB2 ($V0_{OR}$ and SPD_{OR} and not $V0_{BG}$) , MB3 ($V0_{AND}$ and SPD_{OR} and not $V0_{BG}$). $V0_{OR}$ requires a signal in either of two V0 sides, $V0_{AND}$ requires signals on both sides of the V0, $V0_{BG}$ indicates that a beam-gas or beam-halo collision was detected by the V0 which utilizes the timing of the collision. SPD_{OR} requires at least one chip that measured a signal in the SPD [49] [18] .

2.6.2 The High-Level Trigger (HLT)

In order to meet the high computing demands, the HLT [67] consists of a PC farm of up to 1000 multi-processor computers. The raw data of all ALICE detectors are received by HLT via 454 Detector Data Links (DDLs) at layer 1. The first processing layer performs basic calibration and extracts hits and clusters (layer 2). This is done in part with hardware coprocessors and therefore simultaneously with the receiving of the data. The third layer reconstructs the event for each detector individually. Layer 4 combines the processed and calibrated information of all detectors and reconstructs the whole event. Using the reconstructed physics observables layer 5 performs the selection of events or regions of interest, based on run specific physics selection criteria. The selected data is further subjected to complex data compression algorithms.

2.6.3 The Data AcQuisition (DAQ) System

The main task of the ALICE DAQ system [67] is event building and export of assembled events to permanent storage. The DAQ is designed to process a data rate of up to 1.25 GB/s in heavy-ions collisions. Event building is done in two steps. Data from the sub-detectors is received by Detector Data Links (DDLs) on Local Data Concentrators (LDCs). The LDCs assemble the data into sub-events that are then shipped to Global Data Collectors (GDCs). The GDCs archive the data over the storage network as data files of a fixed size to the Transient Data Storage (TDS). During a run period, each GDC produces a sequence of such files and registers them in the ALICE Grid software (AliEn).

2.7 The ALICE offline Computing

The role of the Offline Project is the development and operation of the framework for data processing. This includes tasks such as simulation, reconstruction, calibration, alignment, visualization and analysis. These are the final steps of the experimental activity, aimed at interpreting the data collected by the experiment and at extracting the physics content.

The computing resources required to process the ALICE data are such that they cannot be concentrated in a single computing centre. Therefore, data processing is distributed onto several computing centers located worldwide. At present, 80 centers contribute to ALICEs computing centers. Distribution of the data for reconstruction and analysis cannot be performed manually and this led to the need for an automated system. The concept of Grid was introduced. ALICE uses the ALICE Environment (AliEn) system as a user interface to connect to a Grid composed of ALICE-specific services that are parts of the AliEn framework and basic services of the Grid middleware installed at the different sites. The data analysis and simulation are done by a dedicated frame work called AliRoot. The AliEn and AliRoot framework are discussed in the sections below.

2.7.1 Dataflow

The data processing strategy varies according to the type of collision. During proton-proton collisions the data, recorded at an average rate of 100 MB/s, are written by the DAQ on a disk buffer at the CERN (Tier-0) computing centre, where the following four activities proceed in parallel on the RAW data:

- Copy to the CASTOR tapes;
- Export to the Tier-1 centers to have a second distributed copy on highly-reliable storage media and to prepare for the successive reconstruction passes that will be processed in the Tier-1 centers;
- First pass is processing at the Tier-0 centre. This includes: reconstruction, production of calibration and alignment constants and scheduled analysis;
- Fast processing of selected sets of data, mainly calibration, alignment, reconstruction and analysis on the CERN Analysis Facility (CAF)

the processing of the nucleus-nucleus RAW data proceeds as follows:

- Registration of the RAW data in CASTOR;
- Partial export to the Tier-1 centers to allow remote users to examine the data locally;
- Partial first pass processing at the Tier-0 center to provide rapid feedback on the offline chain;
- Fast processing, mainly calibration, alignment, reconstruction and analysis on the CAF.

During the first pass reconstruction, high-precision alignment and calibration data are produced, as well as a first set of Event Summary Data (ESD) and Analysis Object Data (AOD). The feedback derived from the first pass, including analysis, is used to tune the code for the second pass processing. One full copy of the raw data is stored at CERN, and a second one is shared among the Tier-1s outside CERN. Reconstruction is shared by the Tier-1 centers, CERN being in charge of processing the first pass. Subsequent data reduction, analysis and Monte Carlo production is a collective operation where all Tiers participate, with Tier-2s being particularly active for Monte Carlo and end-user analysis.

2.7.2 AliEn Framework

The concept of ALICE Grid is introduced to process huge amount of data. The user interacts with the Grid via the AliEn [68] User Interface (UI), and the services are offered by a combination of AliEn Middleware, providing high-level or ALICE-specific services, and the Middleware installed on the computing centre, providing basic services. The AliEn system is built around Open Source components, uses Web Services model and standard network protocols. AliEn Web Services play the central role in enabling AliEn as a distributed computing environment. The user interacts with them by exchanging SOAP (Simple Object Access Protocol) messages and they constantly exchange messages between themselves behaving like a true Web of collaborating services. AliEn has been extensively used to access the data recorded and reconstructed in the p-p, Pb-Pb and p-Pb collisions and as well as the simulated data. The results discussed in this thesis are obtained from the data accessed by this environment.

2.7.3 AliRoot Framework

The implementation of AliRoot Framework [69] is based on Object-Oriented techniques for programming and, as a supporting framework, on the ROOT system [70]. It is complemented by the AliEn system which gives access to the computing Grid. This framework is entirely written in C++ except some external programs which are still in FORTRAN. AliRoot has been in continuous development since 1998. Before the start of data taking, it was used to evaluate the physics performance of the full ALICE detector and to assess the functionality of the framework towards the final goal of extracting physics from the data. A schematic picture of AliRoot framework is shown in the Fig. 2.9

Event generation

The offline framework is developed to allow for efficient simulations of nucleus-

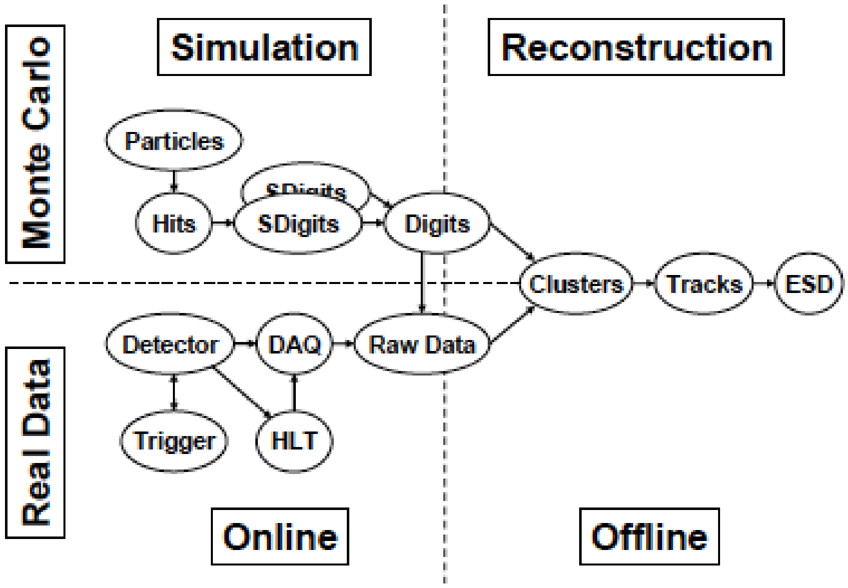

Figure 2.9: A schematic picture of the AliRoot Framework. The figure is taken from the ref. [49]

nucleus, proton-nucleus and proton-proton collisions and to provide a precise simulation of the detector response. The framework provides interfaces to the several event generators such as PYTHIA [30, 31], PHOJET [33, 34], HIJING [37], DPMJET [40] etc. The data produced by the event generators contain full information about the generated particles: type, momentum, charge, and mother-daughter relationship.

Detector Response Simulation

The generated particles are transported through the detector geometry. During the transport, the response of the detectors to each crossing particle is simulated. For this detector response simulation different transport Monte Carlo packages are available, namely GEANT3 [71] GEANT4 [72] and FLUKA [73]. The ALICE detector is described in great detail, including services and support structures, absorbers, shielding, beam pipe, flanges, and pumps. The hits (energy deposition at a given point and time) are stored for each detector. The information is complemented by the so-called track references corresponding to the location where the particles are crossing user defined reference planes. The hits are converted into digits taking into account the detector and associated electronics response function. Finally, the digits are stored in the specific hardware format of each detector as raw data.

Alignment and calibration framework

When the simulation program is started, the ideal geometry is generated via compiled code or read from the OCDB where it was saved in a previous run. Several objects are marked as 'aligneable', that is the geometrical modeller is ready to accept modifications to their position, even if they were obtained by replication. The framework then reads the alignment objects which contain the adjustments in the position of the 'aligneable' objects. The particle transport is then performed in the modified geometry.

The calibration framework is similar to the alignment one. The initial calibration constants come either from the detector properties as measured during construction, or from algorithms running online during data-taking aimed at providing a partial calibration sufficient for the first-pass data reconstruction. During the reconstruction itself, better calibration constants can be calculated and stored in the OCDB.

Reconstruction framework

As described earlier both the physics data and simulated data are stored in the same raw data format. This raw data is then reconstructed using the same algorithms. The output of the reconstruction is the ESD (Event Summary Data) which contains only high-level information such as the position of the event vertex, parameters of reconstructed charged particles together with their PID information, positions of secondary-vertex candidates, parameters of particles reconstructed in the calorimeters, and integrated signals of some sub-detectors.

Analysis

Analysis is the final operation performed on the data to extract the physics information. The analysis starts from ESD produced after reconstruction. To do precise physics study, data is further reduced to Analysis-Object Data (AOD) format. These smaller-sized objects contain only information needed for the analysis. An analysis framework is developed to analyze these reconstructed real or simulated data. As the first step, the analysis framework extracts a subset of the Datasets from the File Catalogue using meta-data selection. Then the framework negotiates with dedicated Grid services the balancing between local data access and data replication. Once the distribution is decided, the analysis framework creates sub-jobs. The framework collects and merges available results from all terminated sub-jobs on request. An analysis object associated with the analysis task remains persistent in the Grid environment so the user can go offline and reload an analysis task at a later date, check the status, merge current results, or resubmit the same task with a modified analysis code.

3

The Photon Multiplicity Detector (PMD) and test of the PMD modules with pion and electron beams

In this chapter a brief description of Photon Multiplicity Detector will be discussed. The performance of the PMD modules with pion and electron beams at various beam energies at the T10 beam line of CERN PS will be presented.

3.1 Photon Multiplicity detector (PMD)

Photon multiplicity detector (PMD) is designed to measure the multiplicity and the spatial distribution of inclusive photons. It consists of two planes of detectors and a Pb converter between them. PMD is situated at 367 cm away from the interaction point and covers $2.3 < \eta < 3.9$ with full azimuthal coverage [64].

3.1.1 Physics goal

Using the measurements of photon multiplicity the following physics topics can be studied:

- Beam energy dependence of average photon multiplicity in forward rapidity region and limiting fragmentation behavior of photons can be studied.

- Photons in forward rapidity can be used to determine the reaction plane for measuring the azimuthal anisotropy of the charged particles in midrapidity

- It can probe the thermalization by measuring the azimuthal anisotropy of the inclusive photons.

- critical phenomena near the phase boundary leading to fluctuations in global observables like multiplicity and transverse energy.

- signals of chiral-symmetry restoration (e.g. disoriented chiral condensates) through the measurement of N_{γ}/N_{ch} in a common part of phase space.

3.1.2 Overview of the PMD design

PMD consists of two identical planes with a $3X_0$ thick Pb plane sandwiched between them. The plane which faces the IP is called Charged Particle Veto (CPV) and the other plane is called Preshower (PRE) plane. A schematic view of the PMD from the IP is shown in the Fig. 3.1.

Each of the planes consist of 24 modules and each of the modules consist of 4608 numbers of honeycomb cells. In the latest configuration four modules has been taken out from each of the plane. So the total number of existing modules are 40. Each module is an independent gas-tight rectangular unit. The modules can be handled individually. There are two types of modules. The modules containing 48 rows and 96 column are called short modules and the modules containing 96 rows and 48 columns are called long modules. The basic unit of PMD is hexagonal or honeycomb

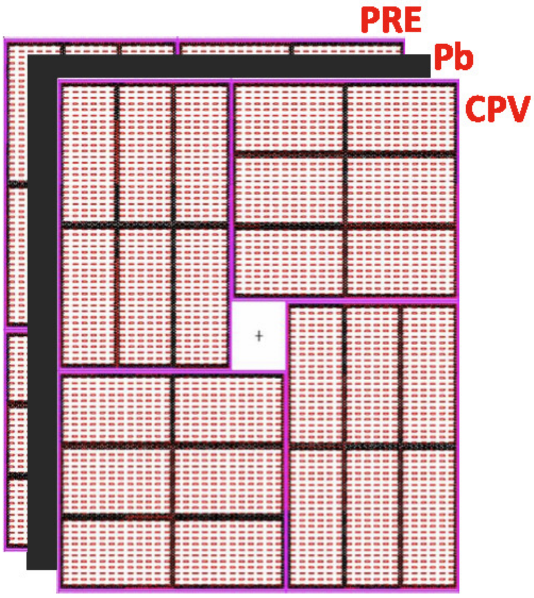

Figure 3.1: A schematic view of PMD from the interaction point.

cells having 5 mm depth and 0.23 cm^2 cross section. A schematic picture of the honeycomb cell is shown in the Fig. 3.2.

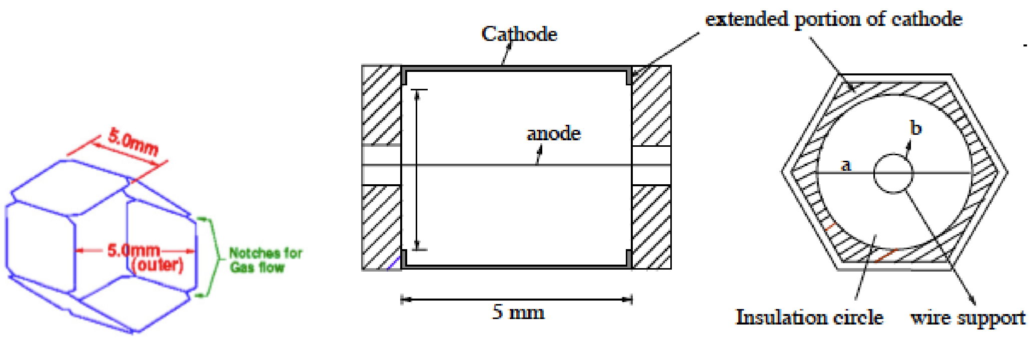

Figure 3.2: A schematic picture of a honeycomb cell of PMD.

A matrix of 48 × 96 or 96 × 48 cells is made using thin copper sheet, which is known as honeycomb chamber. The honeycomb chamber is placed between two gold plated Printed Circuit Boards (PCB). There are 4608 number of cells in a module and gold plated tungsten wires of diameter 20 μ are inserted through the centre of each cell and a proper tension is applied in the wire during soldering. The top PCB has the solder islands at the centre corresponding to each cell. There are 32 connectors to extract the signal from the 32 cells in the top PCB. There are 72 connectors in a module. The bottom PCB has only soldering islands without signal tracks, serving as anchor points. The inner part of the PCBs are gold plated, with circular islands near the anode wire. Together with the honeycomb wall they form part of an extended cathode going very close to the anode wire. A proper alignment is needed to put the honeycomb plane between the two PCBs. One of the alignment pin is used to provide the high voltage to the honeycomb chamber which is used as a cathode plane. The gold plated tungsten wires are used as anodes. Assembly of a module is shown in the Fig. 3.3.

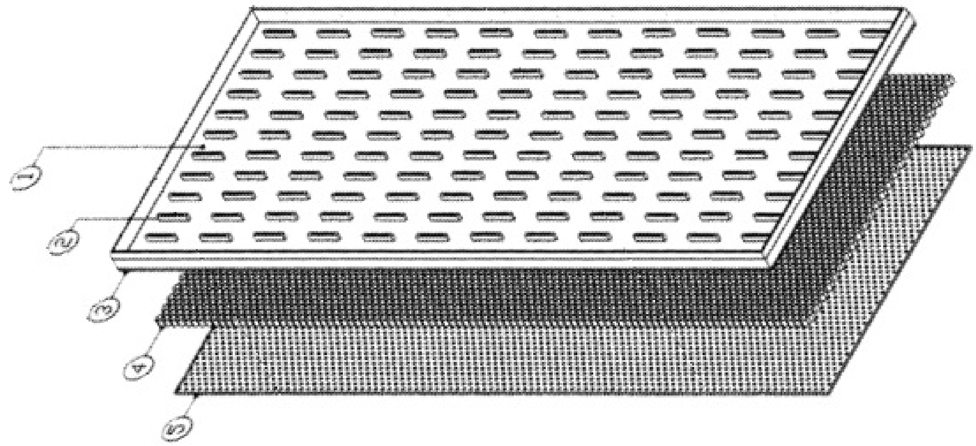

Figure 3.3: Component of a PMD module: (1) Top PCB, (2) 32-pin ETEC connectors, (3) edge frame, (4) honeycomb of 48 × 96 cells, (5) bottom PCB.

The modules are kept inside air-tight containers, which are made of 2 mm thick stainless steel (SS) containing the nozzles for gas inflow and outflow. A mixture of Ar and CO_2 with a ratio of 70:30 by weight flows through the modules.

The rectangular Pb converter is situated between the two planes of PMD. There are 40 Pb plates corresponding to 40 modules. There are two types of Pb plates as modules. The long type lead plate is of the size 49.05 cm $\times$ 21.7 cm while the short type is 42.5 cm $\times$ 25.15 cm. The thickness of the Pb plates are 1.5 cm, which is equivalent to $3X_0$ radiation length.

PMD has two parts on both sides of beam pipe. SS plate of 5 mm thick is used to support the lead converter plates and the modules in each half of the PMD. The SS plate has tapped holes for screws corresponding to hole position in the lead converter plates. There are two different slots on the SS plate for placing two different types of modules. Each SS plate contains 10 modules. Each half of the PMD has independent gas supply, electronic accessories and cooling systems. The PMD is supported from a SS girder in such a way that the two halves can be moved on the girder to bring them together for data taking operation or separated for servicing. The view of the PMD in the ALICE experiment is shown in the Fig. 3.4.

3.1.3 Front End Electronics and Readout

A schematic diagram of the front end electronics is shown in the Fig. 3.5. The signals from the PMD are taken from the anode wires. The Front End Electronic Boards (FEE boards), connected to the detector with the help of flexible kapton cables, collect the signals. After processing and digitizing, the signals are then sent to the Translator Board (TB) via back plane. These signals are then sent to the Cluster Readout Concentrator Unit System (CROCUS) with the help of Patch Bus cables. From the CROCUS these signals are transferred further to the Data Acquisition System (DAQ) with the help of Detector Data Link (DDL).

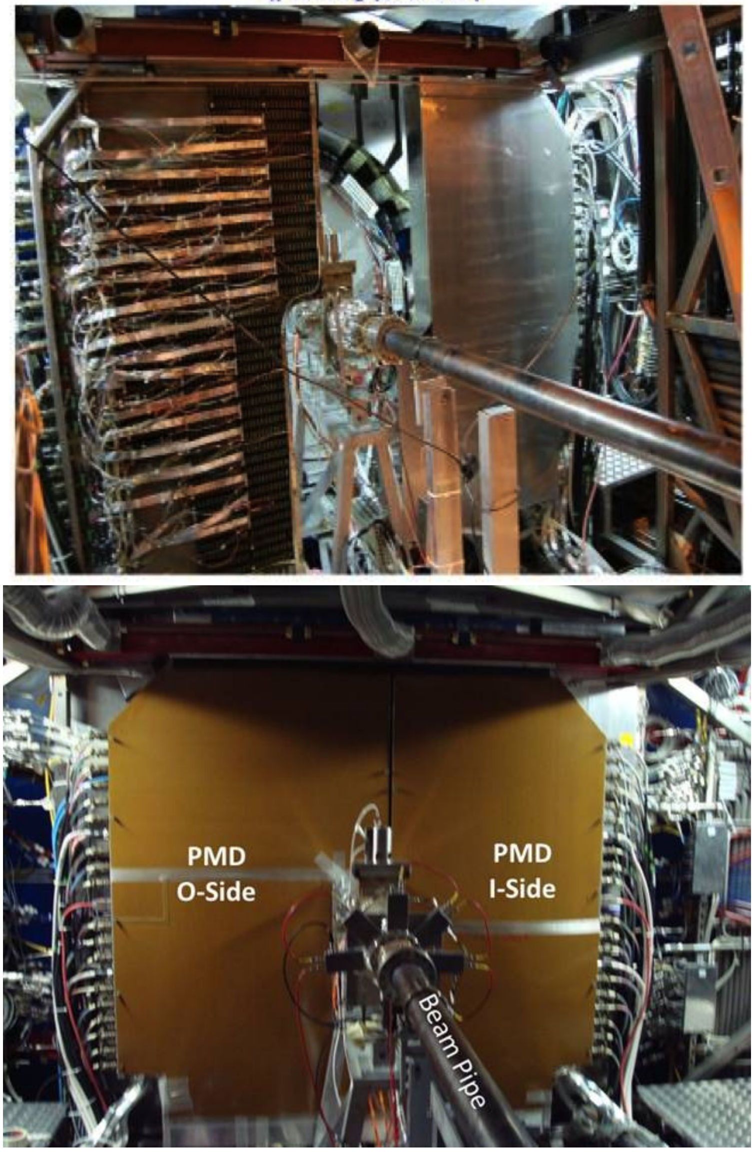

Figure 3.4: View of the PMD looking towards the IP. Upper: two halves of the PMD are separated. Lower: data taking configuration of the PMD.

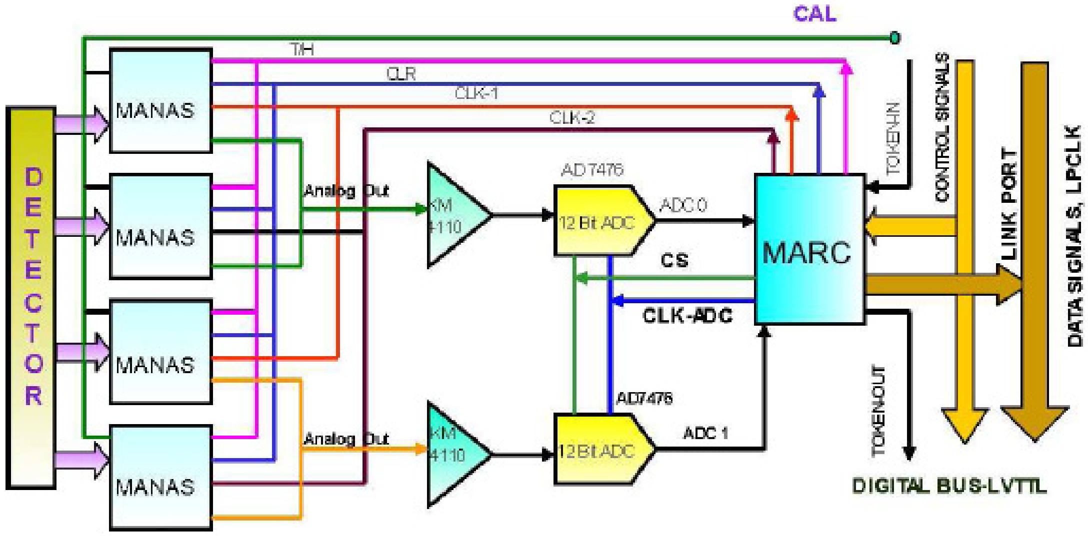

Figure 3.5: A schematic view of the front end electronics of the PMD.

Some of the electronic components are discussed below:

FEE boards and Translator boards (TB):

Each Front End Electronics (FEE) board of PMD consists of four Multiplexed ANAlog Signal Processor (MANAS) chips, two inverting buffer amplifiers, two serial 12 bit ADCs (AD7476) and a custom built ASIC called Muon Arm Readout Chip (MARC). The MANAS chip has sixteen input channels and one output channel. A group of 64 cells are connected to two 32-pin connectors by a flexible cable which connects to the FEE board at the other end. The signals are processed by the MANAS chips which provide the analog outputs. ADCs convert the analog signal coming from MANAS. The digitized output signal is sent to the MARC. MARC controls 4 MANAS chips and 2 serial 12-bit ADCs and performs zero suppression on data.

The Low Voltage Transistor Transistor Logic (LVTTL) type signals are delivered to TB from FEE boards. The TB converts all LVTTL signals to Low Voltage

Differential (LVDS) signals before sending CROCUS and translates all the LVDS signals from CROCUS to LVTTL.

Readout chain: Patch bus

A flexible flat cable known as patch bus cable is designed to transfer the LVDS signals from TB to CROCUS and vise versa. To minimize the electromagnetic disturbances the cable is shielded with aluminum tape. There are 200 patch bus cables of length around 8.5 m are used for the readout of PMD.

CROCUS

The Cluster Read Out Concentrator Unit System (CROCUS) is one of the important readout electronic component of the PMD. It gathers the signals from the FEE via patch bus cable and transfers to the DAQ. It also provide the trigger signal to the detector and allow the calibration. One CROCUS consists of one Concentrator Board (CRT) and five Frontal Boards (FRTs). The FRTs mange the FEEs via patch bus cable. These concentrate Level-I data, which is coming from FEESs and transfer the data to Level-II data concentration crocus system. FRTs also send the calibration signal to the detectors. The main objectives of the CRT are the data acquisition from the FRTs and distribution of the trigger signal to them.

3.1.4 Working principle of PMD

As mentioned earlier PMD consists of two identical planes and a Pb converter between them. The planes are made of small honeycomb cells which are designed as proportional counters. A schematic picture of the working principle of the PMD is shown in the Fig. 3.6

The particles produced in the interaction point pass through CPV plane, then

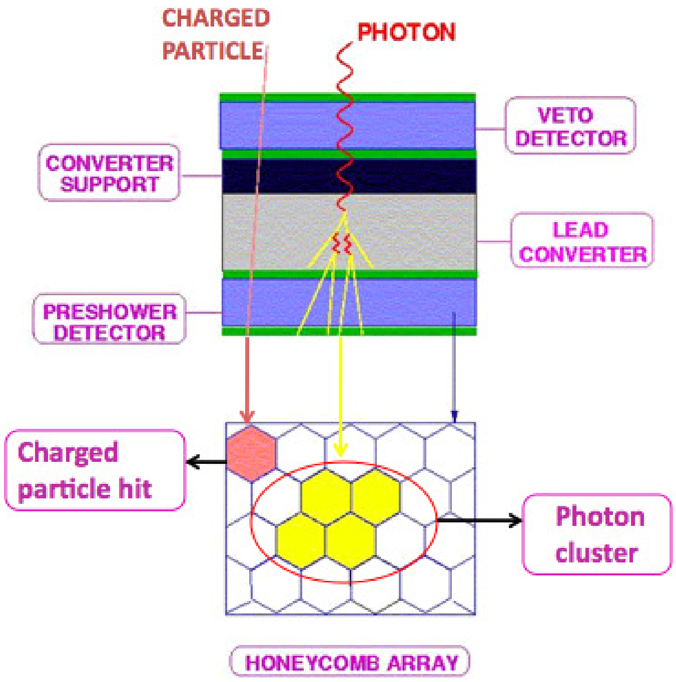

Figure 3.6: A schematic picture of working principle of the PMD.

Pb converter and finally face the preshower plane. The photons do not produce any signal in the CPV plane. These produce electromagnetic shower in the Pb converter by pair production and bremsstrahlung radiation. The thickness of the converter is chosen such a way that conversion probability of photons is high and transverse shower spread is small to minimize shower overlap. The shower particles give signal in the honeycomb cells of the preshower plane. So, the photon affects several cells and deposit large amount of energy in the preshower plane. On the other hand, the charged hadrons behave like Minimum Ionizing Particles (MIP) and produce signal in both CPV and preshower plane. Since the interaction cross-section of the charged hadrons with the Pb converter is very low, they deposit very small energy in the preshower plane and the signals are confined within one or two cells. The different response of the photon and the charged hadron to the detector helps us to discriminate charged particles from the photon sample.

To understand the response of charged particles and photon to the detector test beam experiment has been performed in the year of 2006 [64], 2009 [74] and 2010 [75]. The results from the 2010 test beam experiment is discussed in the next section.

3.2 Test of the PMD modules with pion and electron beam

The basic motivations of the test beam experiment are as follows:

- To understand the response of the charged hadrons to the detector
- Optimizing the thickness of the Pb converter to minimize the overlap of transverse showers
- To get the calibration relation between the energy deposition from simulation (in keV) and digitized electronic signal (in ADC) from real data
- To check the performance of the integrated electronics and Data AcQuisition (DAQ) of the PMD
- To optimize the detector parameters like operating voltage, gas mixture ratio etc.

The detector had been tested in 2009 in the T10 beam line at the CERN PS and calibration relation was made at an operating voltage of 1350V [74, 27, 76, 77]. It was found during the LHC p-p runs that MIP response was different in the p-p runs from that obtained in the test runs and the detector was tripping frequently at the operating voltage of 1350V. It was suspected that the problem might be due to gas mixture of Ar and $C0_2$. Rotameters were used for handling the gas mixture and there had been some instability of the reading, particularly for CO_2, which affects the ionization process significantly. In order to investigate this issue and the possibility of getting lower operating voltage of the PMD to minimize the trips another test beam experiment was performed in the CERN PS T10 beam line in June, 2010 [75]. This time Mass Flow Controllers (MFCs) with recent calibrations as used in the ALICE experimental setup has been used for gas handling.

3.2.1 The experimental setup and data taking

The test beam experiment was performed in the T10 beam line of CERN PS facility. Two modules were placed back-to-back in stand which can moves horizontally. The Pb converter was placed between the two modules to study the preshower plane. The picture of the test beam setup is shown in the Fig. 3.7

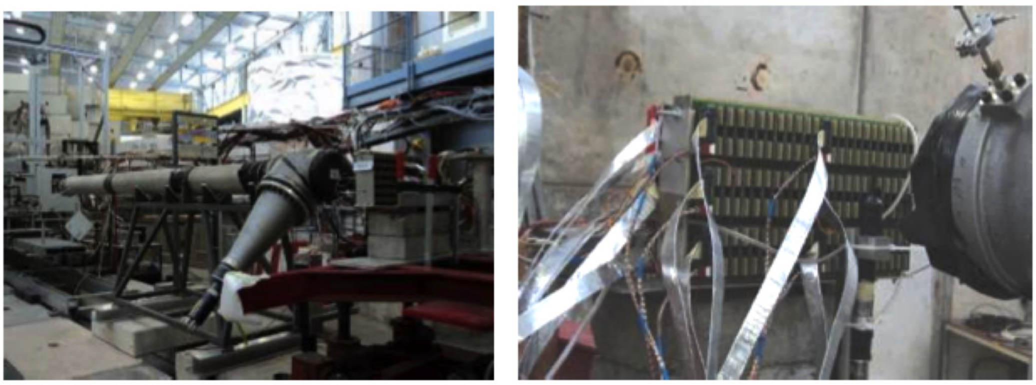

Figure 3.7: Pictorial view of the test beam setup.

Data readout was done using one CROCUS. Each module was connected to

CROCUS through 6 patch bus cables. Two FRT boards were used to integrate all 12 patch bus cables. The connections were made in such a way that it maintains offline mapping configuration of the modules installed at ALICE Cavern to ensure exact geometrical orientations.

Trigger

To generate the trigger there were four scintillator paddles (S1, S2, S3, S4), a 3mm $\times$ 3mm finger scintillator (F) to concentrate the hits on a single cell and a Cherenkov counter (ch). Triggers for the pion beam were generated in two different ways. One is two scintillator paddles S1 and S2 and the finger scintillator produce 3-Fold trigger (S1.S2.F). Other is four scintillator paddles together produces a 4-Fold trigger (S1.S2.S3.S4). In the first case data was more clean than the second one, but the trigger rate was very slow due to very small finger scintillator. To enhance the trigger rate 4-Fold trigger was used. Cherenkov counter (ch) is added to the scintillators to produce the electron trigger. There were two types of electron triggers were used one is 3-Fold (F.S1.Ch) and another is 4-Fold (F.Ch.S1.S4) respectively. A schematic view of the arrangement of the test beam experiment is shown in the Fig. 3.8.

Data taking and Analysis

Data were taken for different combination of beam energy, converter thickness, gas mixture, operating voltage as given in the Table 3.1.

There is a pedestal run corresponding to each run. The intrinsic noise of electronics summed with offset of each channel gives rise to a finite read out value known as pedestal. The actual signal is a combination of pedestal and true signal. The data was taken in zero suppression mode i.e. the pedestal plus true signal is greater

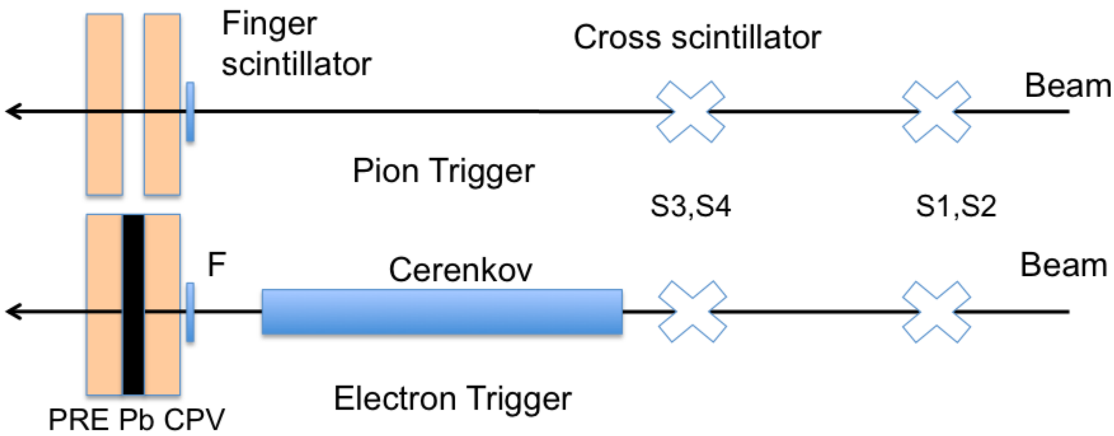

Figure 3.8: Schematic view of the test beam setup. Top: for pion beam; bottom: for electron beam.

Particle	Energy	Radiation length	HV	Remark
Pion	3 GeV	0	1200 -1350 1275,1300,1325	Voltage scan Gas mixture study
Electron	1 GeV	$1X_0, 2X_0, 3X_0, 4X_0$	1300, 1325	Conversion study
Electron	2 GeV	$1X_0, 2X_0, 3X_0$	1300, 1325	-do-
Electron	3 GeV	$3X_0$	1300	-do-

Table 3.1: Data taken during the test beam

than some threshold. Data was reconstructed in the AliRoot framework. During data analysis pedestal was subtracted from the true signal. Clustering was done with the default setting of Crude Clustering (collection of all cells having nonzero energy deposition and connected to each other) as used for the analysis of LHC p-p data.

Fig.3.9 shows the distribution of the mean and RMS of the pedestals for all the channels of both preshower and CPV plane of the PMD. The variation of the pedestal for individual channels are also studied over a long period of time. It is shown that means of the pedestals for a particular channel from both preshower and

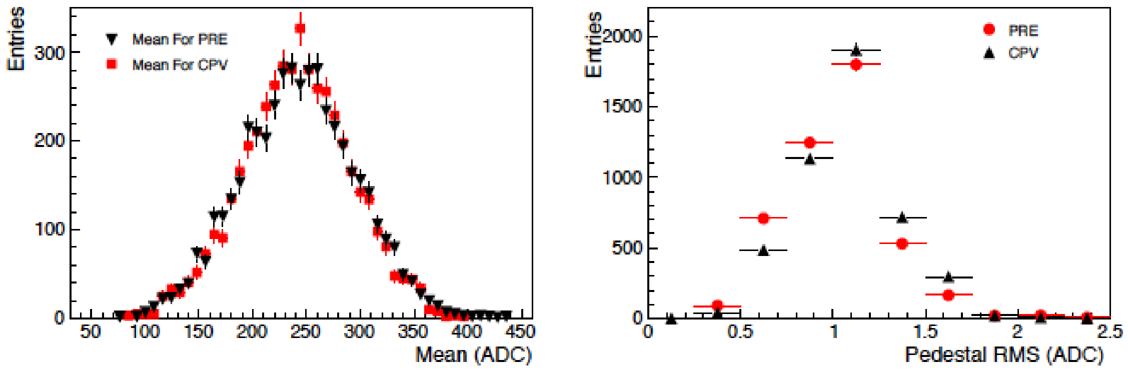

Figure 3.9: Left: Mean of the pedestals for both preshower (triangles) and CPV plane (squares). Right: RMS of the pedestals for both preshower (circles) and CPV plane (triangles).

CPV are constant as a function of pedestal runs (Fig.3.10).

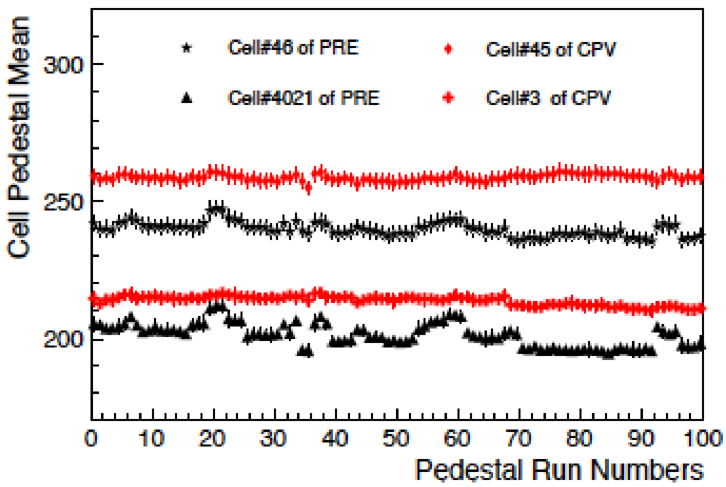

Figure 3.10: Pedestals of individual cell for entire run range for both preshower and CPV planes.

3.2.2 Results and discussions

The pions generally hit one or two cells where as the electrons produce shower in the Pb converter and hit several cells. This is shown in the Fig. 3.11

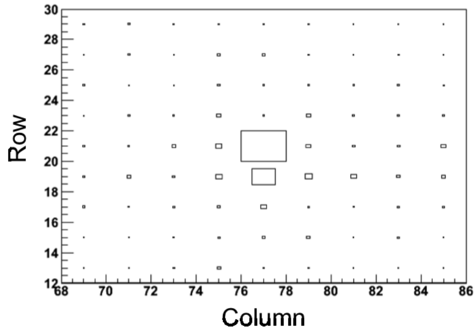

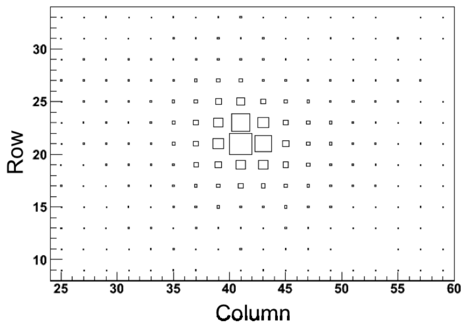

Figure 3.11: Left: row-column view of the module for pion beam. Right: row-column view of the module for electron beam.

Simulation study

For the simulation study with the pions and electrons AliRoot framework was used. Single pions and electrons were generated per event for different combinations of the converter thickness and same beam energy as the experiment. For each of the particles a total of 10k events were generated. Both simulation and data were processed with similar noise cuts and same clustering algorithm. The results of the simulated data are compared with real data and presented below.

Response to pion beam

The experimental setup for the pion beam is shown on the upper part of the Fig.3.8. The ADC distribution and the distribution of number of hit cells are shown in the Fig.3.12

The ADC distribution is fitted with a Landau function and the Most Probable Value (MPV) of the function is found to be 72 ADC. The energy deposition of the pion is calculated in the simulation in terms of keV and after fitting with Landau function the MPV value is found as 0.56 keV. It is observed that almost 90% times pions are confined in single cell and 7% times they hit 2 cells. Similar behavior is

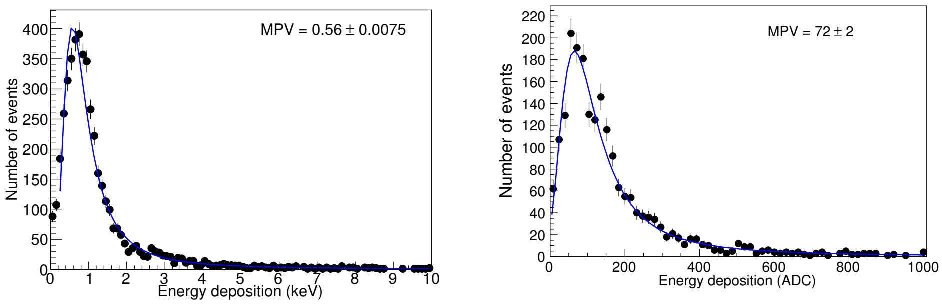

Figure 3.12: Left: energy deposition of 3 GeV pion in keV (simulation). Right: energy deposition of 3 GeV pion in ADC (data). The solid lines are the Landau fits.

also observed in the simulation (Fig.3.13).

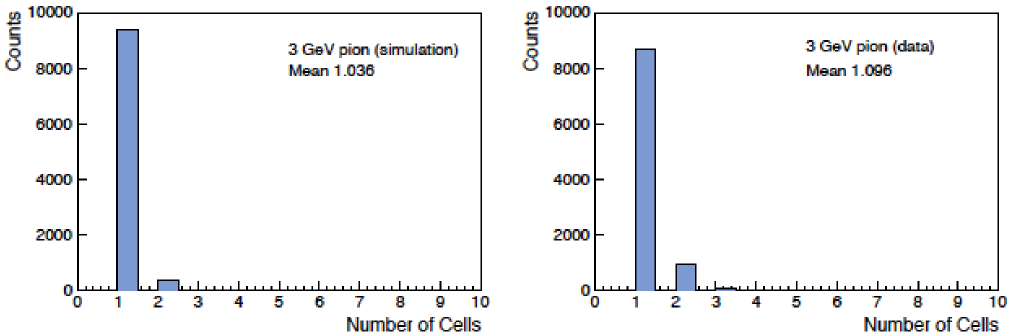

Figure 3.13: Number of cells hit by the 3 GeV pion. Left: in simulation. Right: in data.

Charged particle detection efficiency

The Charged particle detection efficiency is calculated using the 3 GeV pion beam. It is defined as a ratio between the detected pion events and incident pion events. The detected event is defined as any hit within 6cells $\times$ 6cells window around the beam position. The incident events are the triggered events. The efficiency is calculated for different operating voltages and it is observed that efficiency becomes almost constant from 1300V. The Most Probable Value (MPV) of the energy deposition of pion is also presented as a function of operating voltages (Fig.3.14).

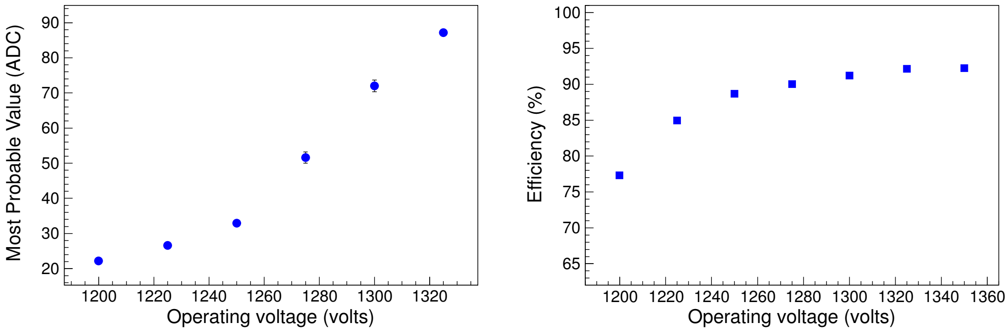

Figure 3.14: Left: MPV as a function of operating voltage for 3 GeV pion. Right: efficiency as a function of operating voltage for 3 GeV pion.

Gas mixture study

A mixture of Ar and CO_2 gas with the ratio of 70:30 (by mass) has been used in PMD at an operating voltage 1300V. Three different ratios of gas mixture (Ar : CO_2 = 65:35, 70:30, 75:25) have been used at two different operating voltages (1300V, 1325V). It is noticed that MPV values are increasing with increasing of Ar percentage for a fixed operating voltage. But the increasing of Ar content causes the increasing of spark rate. Efficiency is about 92% in all the cases and increases marginally with the increasing of Ar content and also with the increasing of operation voltage (Fig.3.15).

Response to electron beam

To understand the preshower properties of the detector electron beams of different energies (1GeV, 2GeV, 3GeV) wad used and for each beam energy thickness of the Pb converter was varying from $1X_0$ to $4X_0$. The electrons produce shower in the Pb converter and hit several numbers of cells. Fig.3.16 shows the number of cells hit for 3 GeV electrons passing through $3X_0$ Pb converter. It is shown the transverse shower size is slightly larger in data than that of the simulation. It was

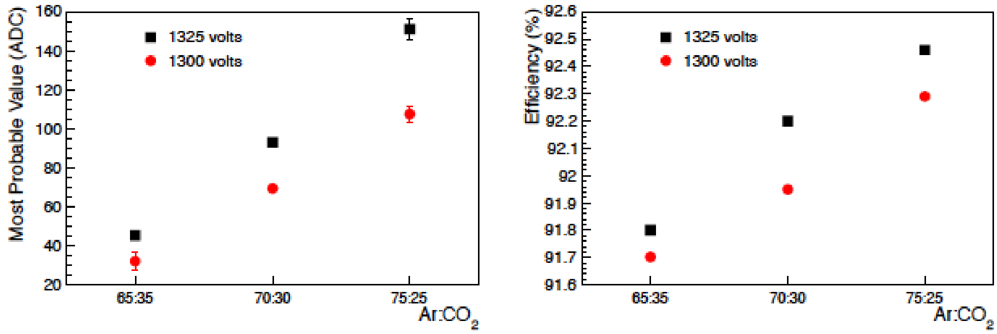

Figure 3.15: Left: MPV versus ratio by mass of the gas mixture. Right: efficiency for different mixture of Ar and CO_2. Different symbols stand for two different operating voltages.

also observed in case of pion (Fig.3.13). It may be due to the material effect, which is not present in the simulation.

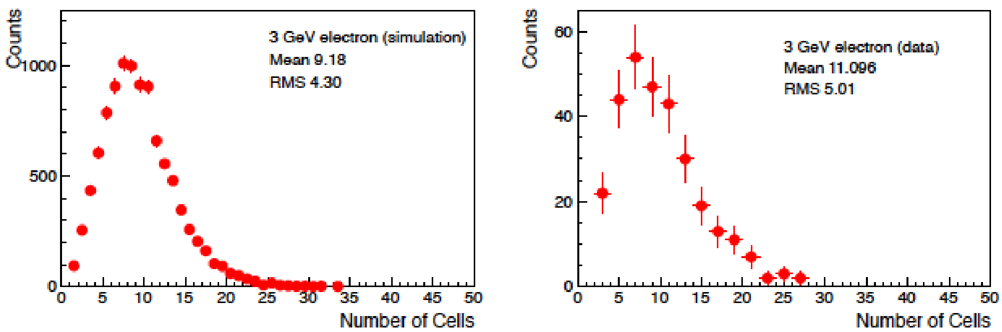

Figure 3.16: Number of cells hit i.e. the transverse shower size for the 3 GeV electron passing through $3X_0$ radiation length in simulation (left) and in data (right).

The energy deposition of the electron is measured both in data and simulation. In simulation it is measured in terms of keV and in data in terms of ADC. The energy deposition spectra are shown in the Fig.3.17 and it is observed that the spectra are slightly broader in case of data than the simulation. It is obvious since the contribution of fluctuation in processes involved in signal formation from the energy deposition and all the stages in electronics.

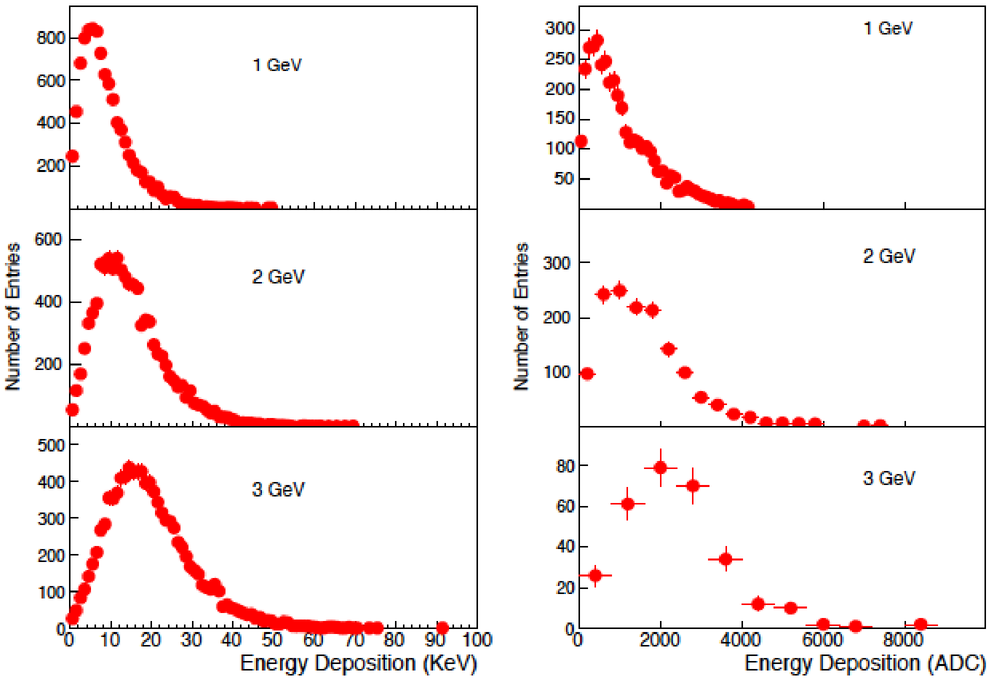

Figure 3.17: Left: energy deposition spectra of the electrons in keV in simulation. Right: energy deposition spectra of the electrons in ADC in Data. Upper, middle and lower panels of the figures represent 1 GeV, 2 GeV and 3 GeV respectively.

The mean values of the energy depositions are studied as a function of radiation length of the Pb converters for different beam energies both in simulation and data. It is shown that the electrons deposit more and more energies with the increase of radiation length as well as the beam energy (Fig.3.18).

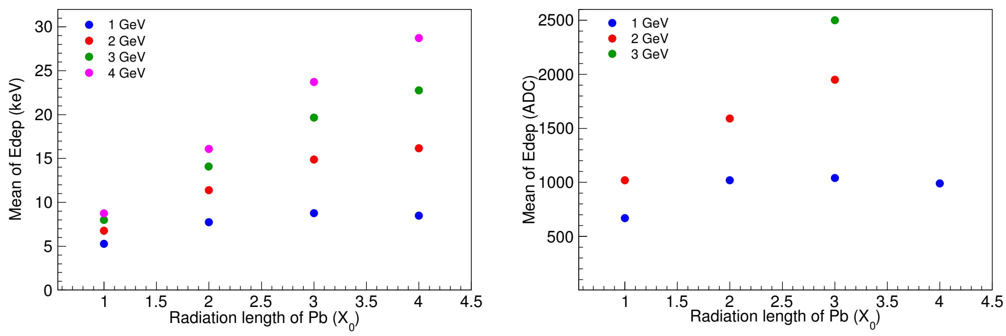

Figure 3.18: Mean of the energy deposition spectra in simulation (left) and in data (right) for different beam energies.

Calibration Relation

In simulation the energy deposition is measured in keV unit whereas in data it is measured in the unit of ADC. To make the simulation as close as data it is important to know the relation between them, which is known as the calibration relation. The data points are obtained from various combinations of electron beam energy and thickness of the Pb converter at an operating voltage of 1300V as shown in the Fig.3.18. The mean values of the energy depositions in ADC are plotted as a function of the mean values of the energy depositions in keV and fitted with a straight line (Fig.3.19). The parameters obtained from the straight line fit are used to convert energy deposition in keV to ADC in the simulated PMD data.

Readout Resolution

Readout resolution is defined as:

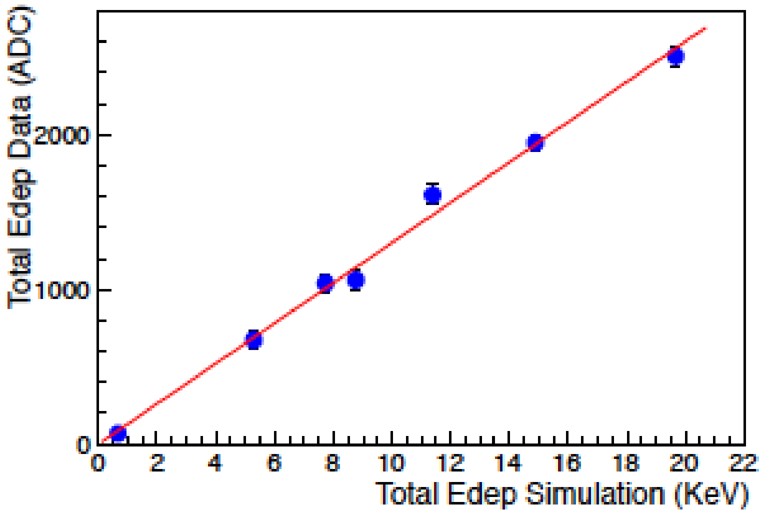

Figure 3.19: keV to ADC conversion. Solid line is linear fit to data.

$$ReadoutResolution = \sqrt{(\frac{\Delta E_{data}}{Mean_{data}}) - (\frac{\Delta E_{sim}}{Mean_{sim}})}, \tag{3.1}$$

where $Mean_{data}$ and $Mean_{sim}$ are the mean of the ADC distributions and ΔE_{data} and ΔE_{sim} are the variations of the energy depositions in data and simulation respectively.

It is observed that the widths of the distribution of energy deposition of both pion and electron are smaller in simulation compared to the test beam. The increased width of the energy in test beam is coming because of the extra fluctuation due to electronics. This extra fluctuation is known as readout resolution. Fig. 3.20 shows the readout resolution as a function of mean energy deposition. The data points are fitted to a polynomial of second order. It is found that that after implementing the readout resolution in the simulation, both Monte Carlo and data agree well as

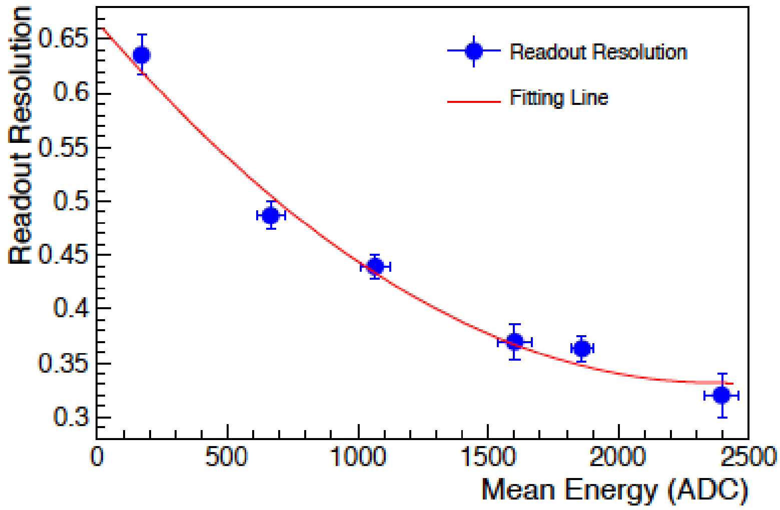

Figure 3.20: Readout resolution as a function of ADC. Solid line is the linear fit to data.

shown in Fig. 3.21.

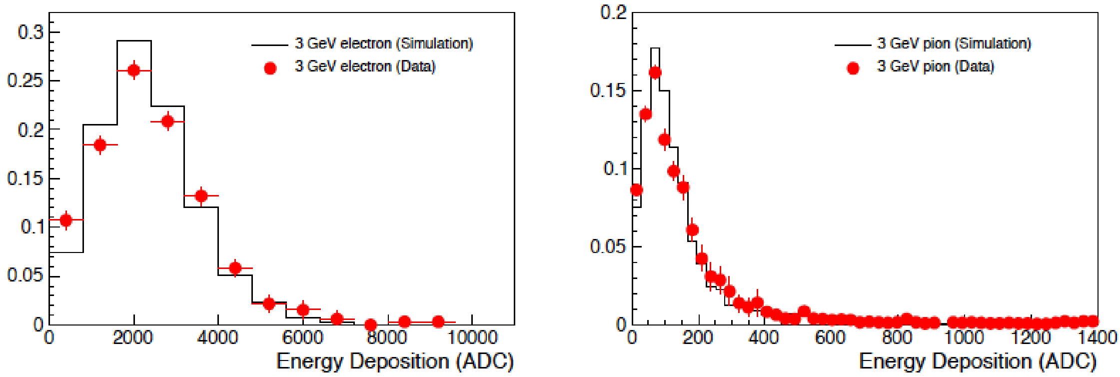

Figure 3.21: ADC distribution of electrons (left) and pions (right) after implementing the readout resolution. Solid points represent the data and the lines represent the simulation.

3.2.3 Split Cluster study

As the electron passes through the Pb converter, it produces electromagnetic showers. This shower of electron and positron hits many cells on the preshower plane. While in most of the cases these cells are all connected to give a single cluster, sometimes these may give two or more clusters. These additional clusters are called split cluster. The splitting of clusters may arise due to physical reasons like one of the shower particles being emitted at a large angle within the converter and landing at a distance from the main cluster on the preshower plane or due to imperfections in the detector like dead cells appearing in between to break the contiguity of cells. It could also arise due to imperfections in clustering algorithm.

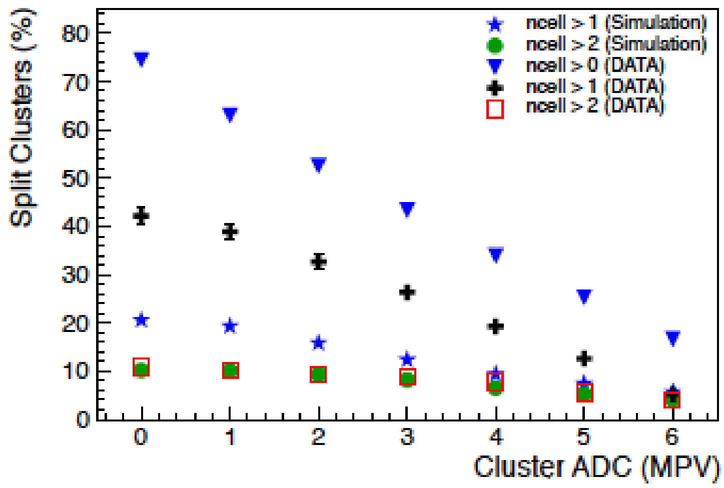

Figure 3.22: Percentage of split clusters as function of the MPV of cluster ADC. Different symbols represent different ncell cuts. Stars and circles represent the simulation and the rest of the symbols represent test beam data.

The split cluster study has been done both in simulation and data. The data from the preshower plane are used for 2 GeV electron passing through $3X_0$ radiation length of the Pb converter. Fig.3.22 shows the split cluster percentage as a function of different ADC values for ncell > 0, ncell > 1 and ncell > 2. Simulation results are also produced in a same condition. It is observed that with the increase of threshold and ncell cuts the percentage of split clusters decreases. In the case of clusters with ncell > 2 simulation and test beam results are very close to each other.

4 Multiplicity and pseudorapidity distributions of photons in p-p collisions at forward rapidity

The measurements of photon multiplicity using the Photon Multiplicity Detector (PMD) will be discussed in this chapter. The details of the analysis procedure will be described and the results along with the different model comparisons will be presented.

4.1 Introduction

The Large Hadron Collider (LHC) at CERN offers unique opportunities to study the particle production in proton-proton (p-p) collisions. Measurements of multiplicity and pseudorapidity distributions of produced particles in p-p collisions are important for the study of particle production mechanisms and to provide the baseline for the study of heavy ion collisions. ALICE has published charged particle multiplicity and pseudorapidity distributions in p-p collisions [78, 25, 24]. These measurements, performed at midrapidity show a more substantial increase in the pseudo-rapidity density of p-p collisions as the energy goes from 0.9 TeV to 7 TeV relative to what was expected based on theoretical calculations [78]. The photon measurements provide complementary information to the one provided by charged particles since the majority of the photons are decay products of produced particles such as π^0. This work focuses on the particle production mechanism in the forward rapidity region and, additionally, provides information about the longitudinal scaling of produced particles which was found at lower energy [79]. The beam energy dependence of the particle production in midrapidity has been published [78]. It will be interesting to study this in the forward rapidity since the particle production mechanisms may differ at forward rapidity than that of midrapidity.

4.2 Simulation framework

The ALICE Offline Project has developed a coherent simulation framework known as "AliRoot", an object oriented (C++) framework, based on "ROOT". AliRoot provides the primary event simulation, transport of the produced particle using GEANT3 and response of the detectors in simulation. "AliEn" framework has been developed to produce simulated data in ALICE detector environment, to reconstruct the data and to provide the analysis environment [chap 2, section 2.7.3].

The particles generated by the event generator produce hits in the detector while passing through it. The hit information is stored in terms of energy deposition and position. Summing up the energy deposited by all particles passing through a given cell in an event summable digits (Sdigits) are produced. The GEANT energy deposition is now converted in ADC using the keV to ADC conversion relation obtained from test beam experiment [75]. The digits are then transformed to raw data by introducing mapping between the cells and corresponding electronics channels. This is now in the same level as in the experimental raw data. Reconstruction is performed in this raw data level both in simulation and real data. The clustering is performed on the hit cells as in the real data (section 4.4.4). In the simulated data, each cluster can be associated with the incoming photon or hadron track [27].

4.2.1 Photon-hadron discrimination

It has been observed from the test beam data that charged hadrons hit mostly one or two cells and the response in terms of ADC distribution can be described by a Landau distribution (Fig. 3.12). It is observed that the MPV (most probable value) of the ADC distribution is 72±2 ADC. On the other hand, photons or electrons produce showers in the converter plane, and affect a larger number of cells as well as deposit a large amount of energy (Fig. 3.17). We take advantage of this very different response of the detector to discriminate between incident charged hadrons and photons. Thus, the discrimination between photons and hadrons is performed by applying thresholds on the number of cells in a cluster as well as the ADC content. Detailed simulation studies have been done in order to find proper thresholds so that the obtained photon samples are of high values of purity and efficiency.

The number of selected clusters which pass the discrimination threshold are called γ-like clusters ($N_{\gamma_{like}}$). The number of identified photon in $N_{\gamma_{like}}$ sample are called $N_{\gamma_{detected}}$. We define two quantities which are important for this analysis:

Efficiency = $\frac{N_{\gamma_{detected}}}{N_{\gamma_{incident}}}$

Purity = $\frac{N_{\gamma_{detected}}}{N_{\gamma_{like}}}$

The efficiency and purity depend strongly on the cuts on the discrimination threshold (the cluster ADC and number of cells in the cluster). We need to choose a proper cut where we have high purity and good efficiency. In the present analysis, two sets of cuts were chosen:

- ADC>6 MPV and $N_{cell} > 2$
- ADC>9 MPV and $N_{cell} > 2$

The efficiency and purity values obtained with these thresholds will be shown later in Fig. 4.9.

4.3 Effect of upstream material in front of the PMD

Since PMD is in the forward η region, effects of the upstream material in front of the PMD should be taken into account. To do this a very detail study has been made on the material budget in the simulation using the PHOJET [33, 34] event generator. So, before going to the "data analysis" part, the "Effect of upstream material in front of the PMD" will be discussed.

4.3.1 Distribution of upstream material

PMD is situated at a distance of 367 cm in the forward direction from IP. Between the IP and the PMD there are some detectors or part of the detectors. These are frames of the Time Projection Chamber (TPC), services of the Inner Tracking System (ITS), Forward Multiplicity Detector (FMD), VZERO detector and the beam pipe. They could affect different η regions of the PMD. All the materials, i.e. all the detectors and its services have been implemented in the GEANT of the AliRoot as proper as possible. Material effect has been studied in the simulation using the latest AliRoot version (v5-03-Rev-28).

Fig. 4.1 shows the pictorial presentation of the FMD, V0A and ITS in front of the PMD as implemented in Aliroot.

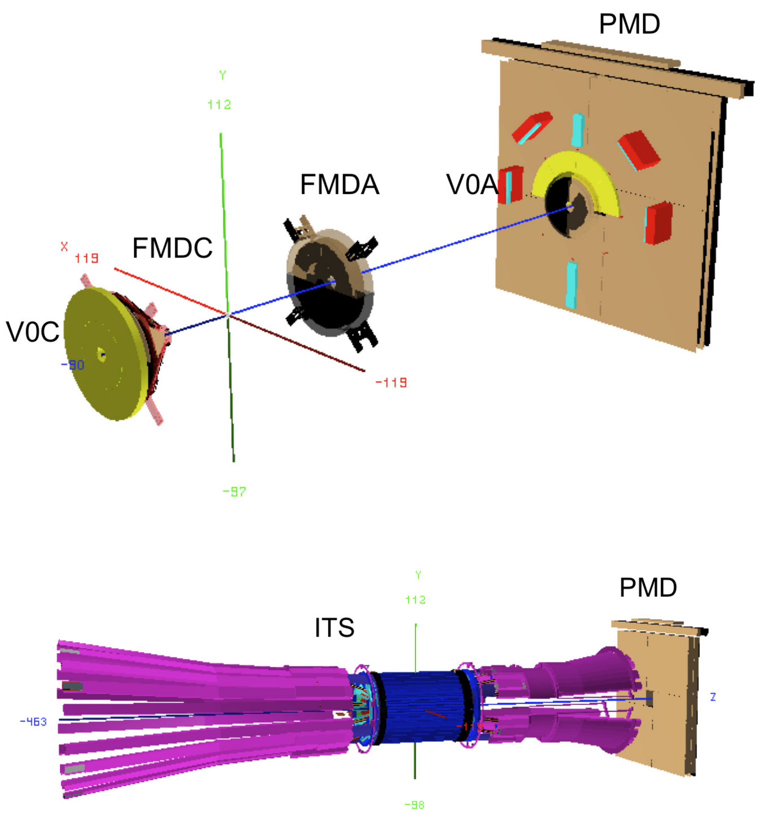

Figure 4.1: Pictorial view of the V0, FMD and ITS in front of PMD.

Fig. 4.2 shows the contribution of the upstream material in terms of radiation length in η - ϕ acceptance. It is observed that contribution of all the detectors are very less within the acceptance of the PMD ($2.3 < \eta < 3.9$).

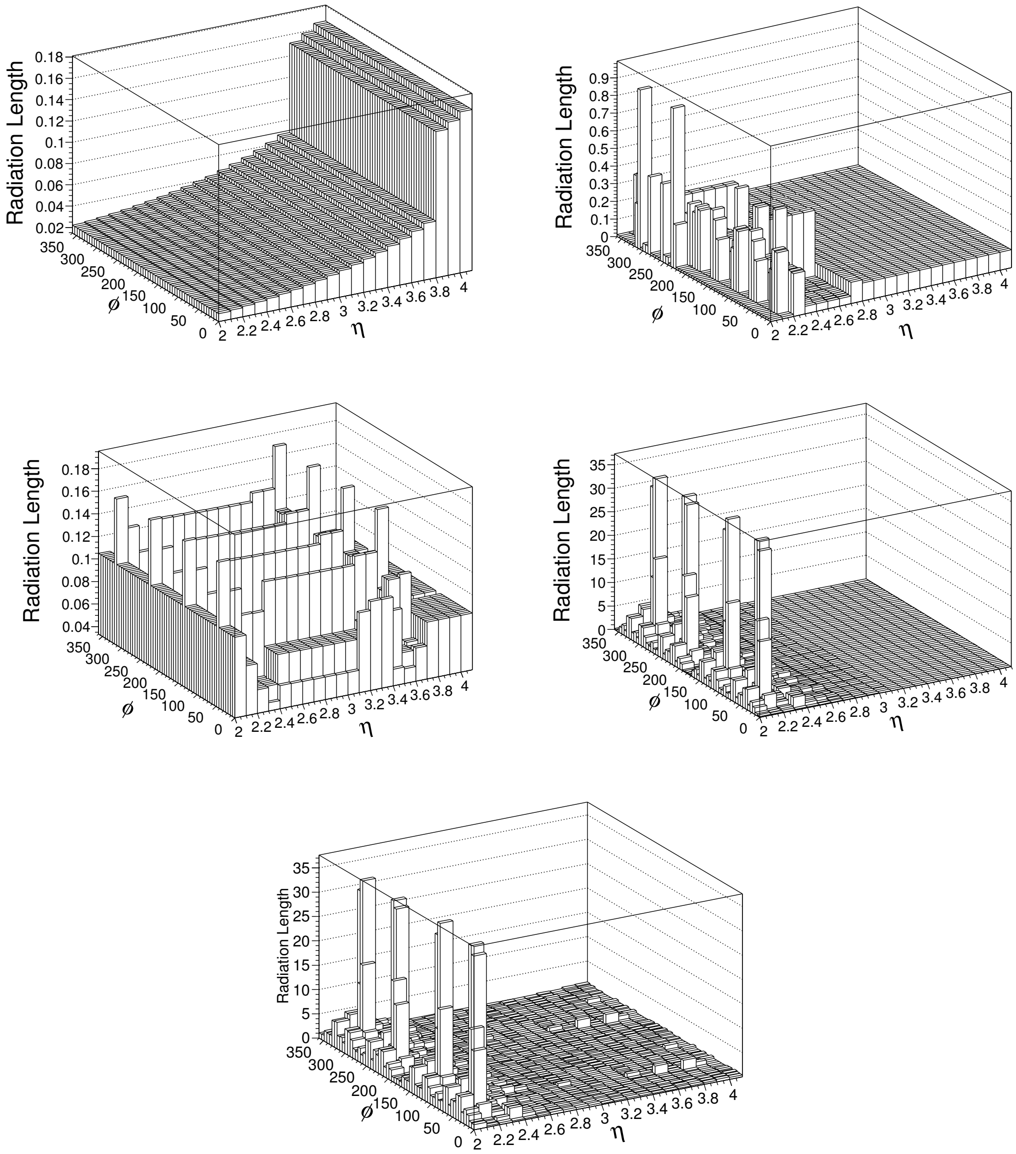

Figure 4.2: An η-ϕ lego plot showing the amount of material in front of the PMD for different cases: upper left: only the beampipe, upper right: only VZERO, middle left: only FMD, middle right: only ITS, and bottom: all detectors and services as implemented in Aliroot in front of PMD.

4.3.2 Deflection of original photon tracks

One of the main effects due to the upstream material is the deflection of the photon tracks. The original photon tracks are scattered and landed on the detector after deflection. The effect of upstream material can be assessed by plotting the distribution of the deflection of the photons in terms of η - η_{orig} and ϕ - ϕ_{orig} for PMD in air and PMD in the presence of all the upstream material. Here, (η_{orig}, ϕ_{orig}) is the location of the original (incident) photon track and (η,ϕ) is that of the detected photon track. Thus, η - η_{orig} and ϕ - ϕ_{orig} denote the deviation of incoming photon tracks with the identified cluster location on the detector. These distributions have been studied for different beam energies. In all cases, large deviations are observed in the PMD with all detector with respect to PMD in air case. The deviations depict the effect because of the presence of upstream material.

Fig. 4.3 and Fig. 4.4 show the η - η_{orig} and ϕ - ϕ_{orig} for PMD in air (dotted line) and PMD in the presence of all the upstream material (solid line) at $\sqrt{s} = 2.76$ and 7 TeV respectively. It is observed that the amount of deviation from the original tracks has been reduced a lot after applying the photon-hadron discrimination thresholds.

To estimate the background in photon tracks due to material in front of the PMD we computed the root mean square (RMS) values of distributions of η - η_{orig} in the PMD only case (dotted curves in Fig. 4.3 and Fig. 4.4). The percentage of area outside this dotted curves have been calculated using different RMS values of the dotted curves. Fig. 4.5 shows the percentages of the background as a function of RMS values of the dotted curve (1×RMS, 2×RMS, 3×RMS, etc.). The open circles show the background percentage for no threshold and other points show the backgrounds for two different sets of thresholds. This shows that the background from upstream material is minimized with the application of the discrimination thresholds.

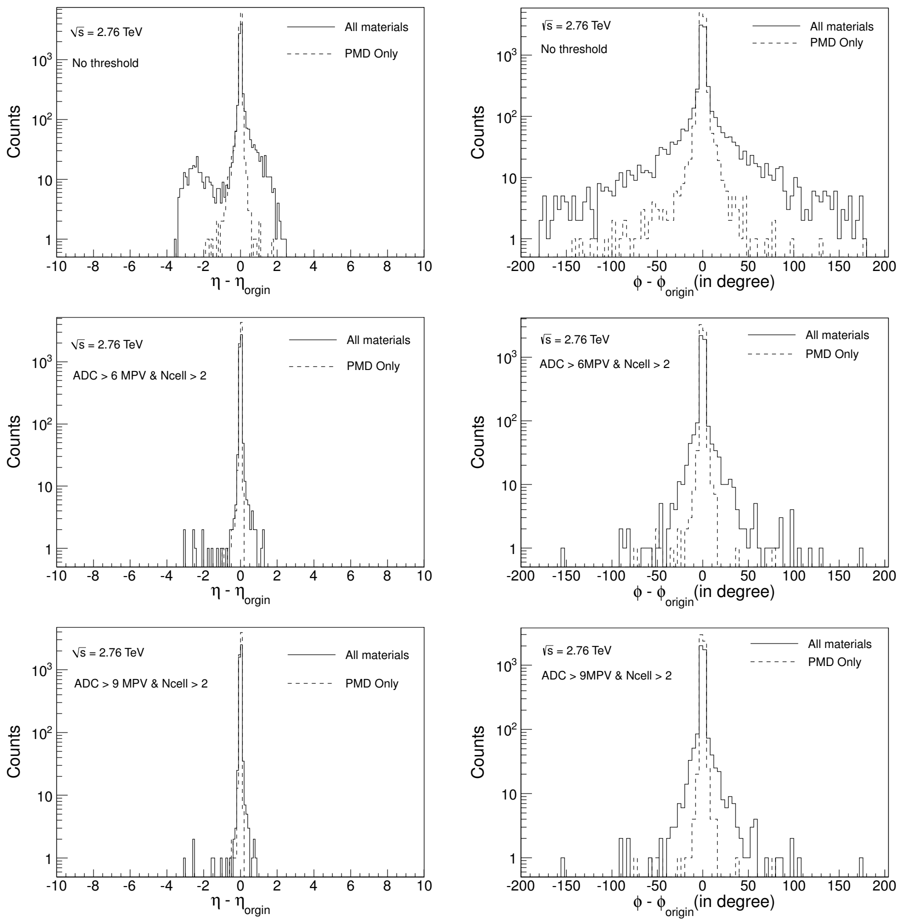

Figure 4.3: At $\sqrt{s} = 2.76$ TeV: deflection of photon tracks. The upper panel shows the case where there is no discrimination threshold, whereas the middle and lower panels show the results for two different discrimination thresholds. Solid line is for PMD with all detectors and dotted line is for PMD in air.

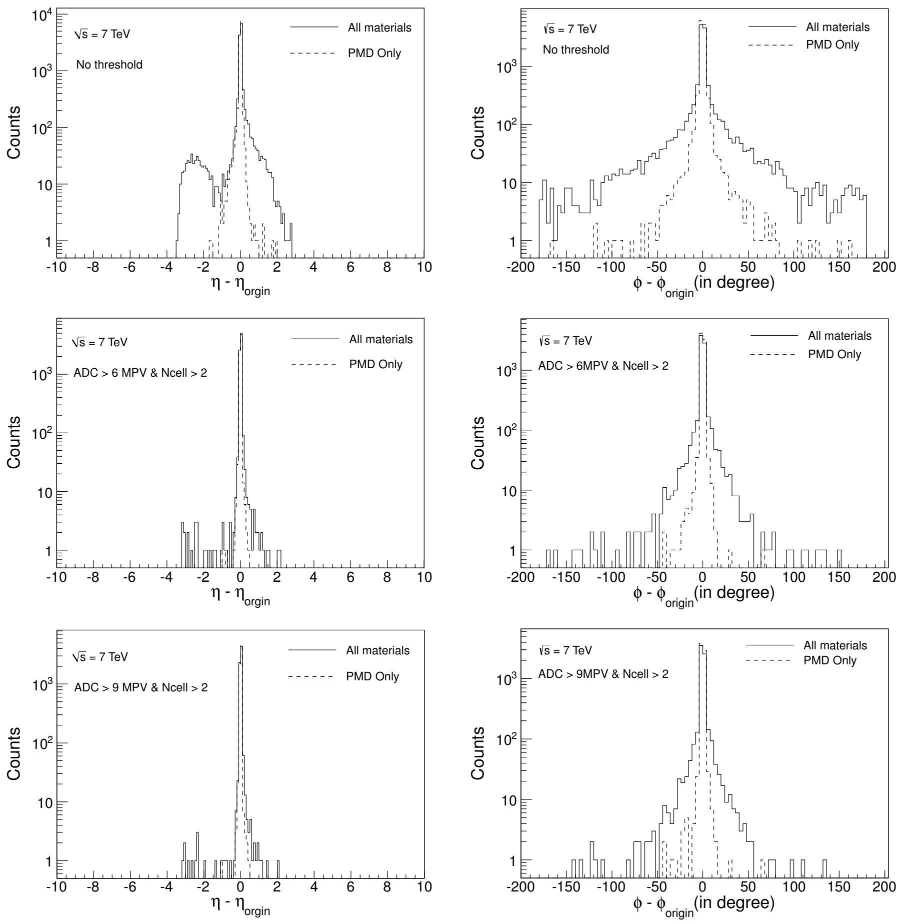

Figure 4.4: At $\sqrt{s} = 7$ TeV: deflection of photon tracks. The upper panel shows the case where there is no discrimination threshold, whereas the middle and lower panels show the results for two different discrimination thresholds. Solid line is for PMD with all detectors and dotted line is for PMD in air.

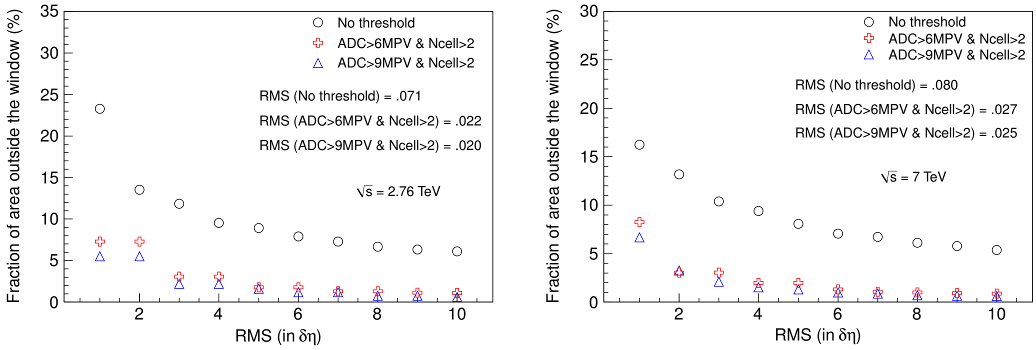

Figure 4.5: Fraction of area of solid curve outside the dotted curve as a function of different RMS values of the dotted curve for no threshold (open circles), and for two different thresholds (open crosses and open triangles). left: 2.76 TeV, right: 7 TeV.

4.3.3 Study of split clusters

Usually one photon track produces one cluster in the preshower plane. Each cluster is then tagged by the track number corresponding to the incident photon. In some cases it is found that different clusters have the same associated track number. In these cases the cluster with the highest ADC value is identified as the main cluster and the remaining are called split clusters.

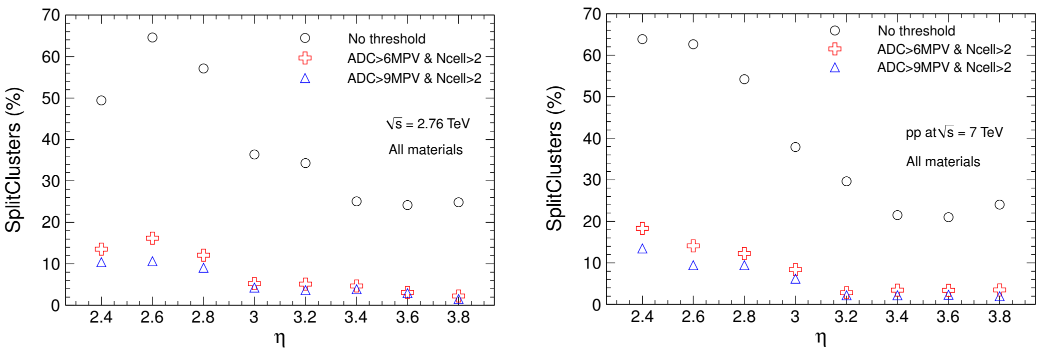

Figure 4.6: Number of split clusters in % versus η for no threshold (open circles) and two different thresholds.

These split clusters have low ADC values. The split clusters arise because of the photon conversion in lead and also from the upstream material. In Fig. 4.6 the open circles denote the percentage split clusters when no threshold is applied. After applying photon hadron discrimination thresholds, the percentage split clusters are significantly reduced.

4.3.4 Study of efficiency and purity

The definitions of the efficiency and purity have been given in the section 4.2.1. Here, efficiency and purity have been presented with the PHOJET event generator as well as with the PHOJET with 10% increased material at 0.9 TeV. For both cases efficiency and purity have been plotted as a function of the different thresholds in the Fig. 4.7. Ratio between the PHOJET + 10% and PHOJET has been plotted and it is observed that ratios are roughly one considering the statistical error bars in the points (Fig. 4.8).

Efficiency and Purity have been plotted as a function of the different thresholds in the Fig. 4.9 for PHOJET and PYTHIA event generator. It is shown that the values are similar for all the thresholds. It indicates the robustness of the results.

4.3.5 Occupancy

Occupancy is defined as:

$$occupancy = \frac{number\ of\ cells\ fired\ in\ an\ \eta\ bin}{total\ number\ of\ cells\ in\ that\ \eta\ bin}, \tag{4.1}$$

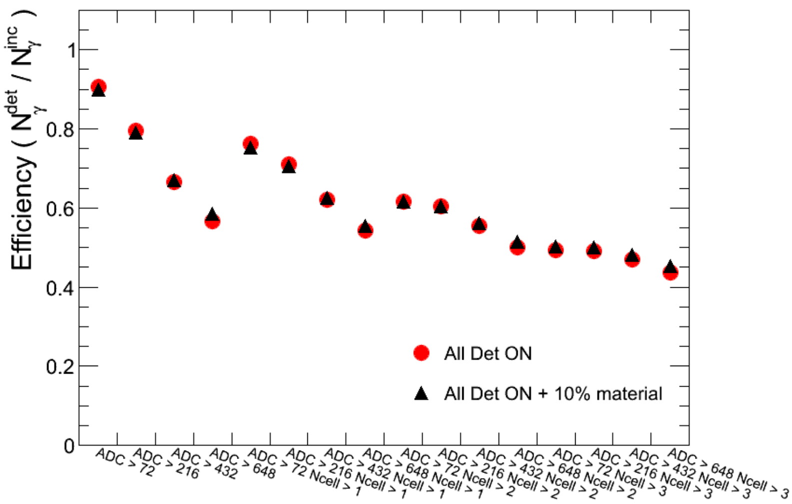

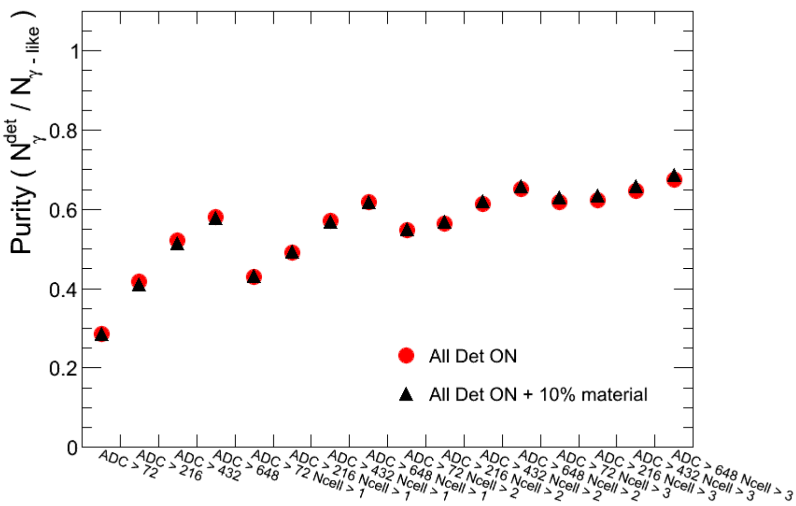

Figure 4.7: Efficiency and purity are plotted as a function of different thresholds. ADC > 6MPV ; $N_{cell} > 2$ and ADC > 9MPV; $N_{cell} > 2$ have been used due to their high purity and good efficiency. The circles represent the result from PHOJET with default material and the triangles represent the result from PHOJET with 10% increased material.

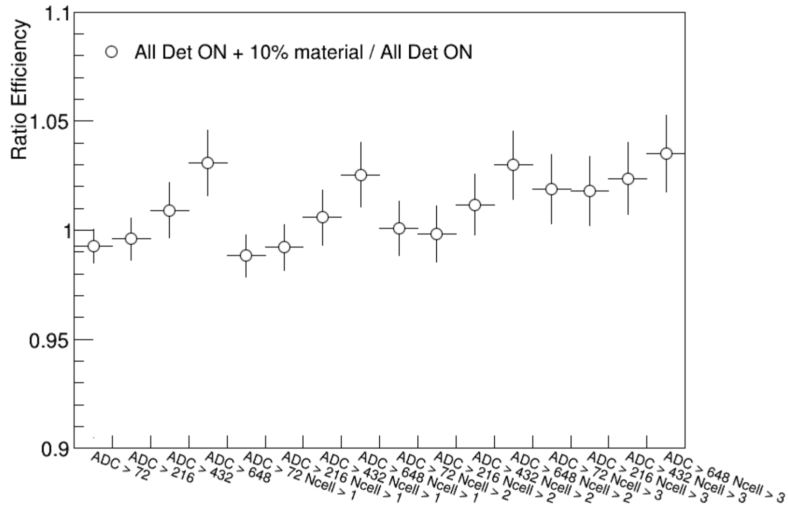

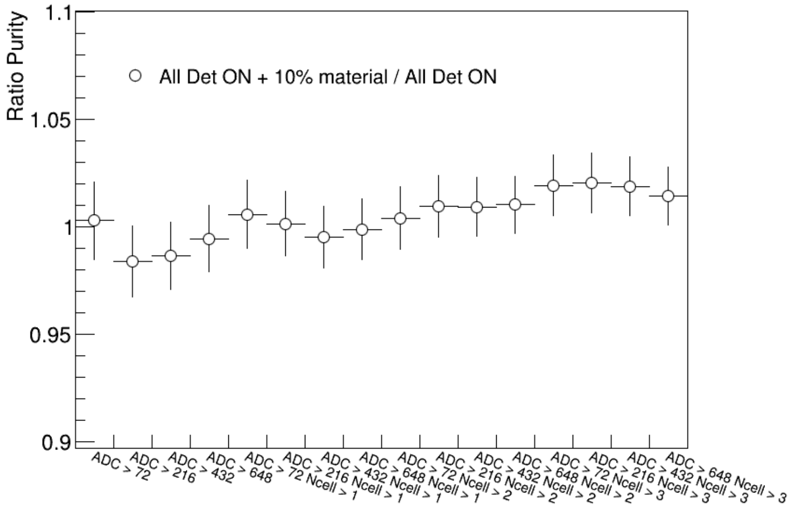

Figure 4.8: Ratio of efficiency (upper) and purity (lower) between PHOJET and PHOJET+10% material.

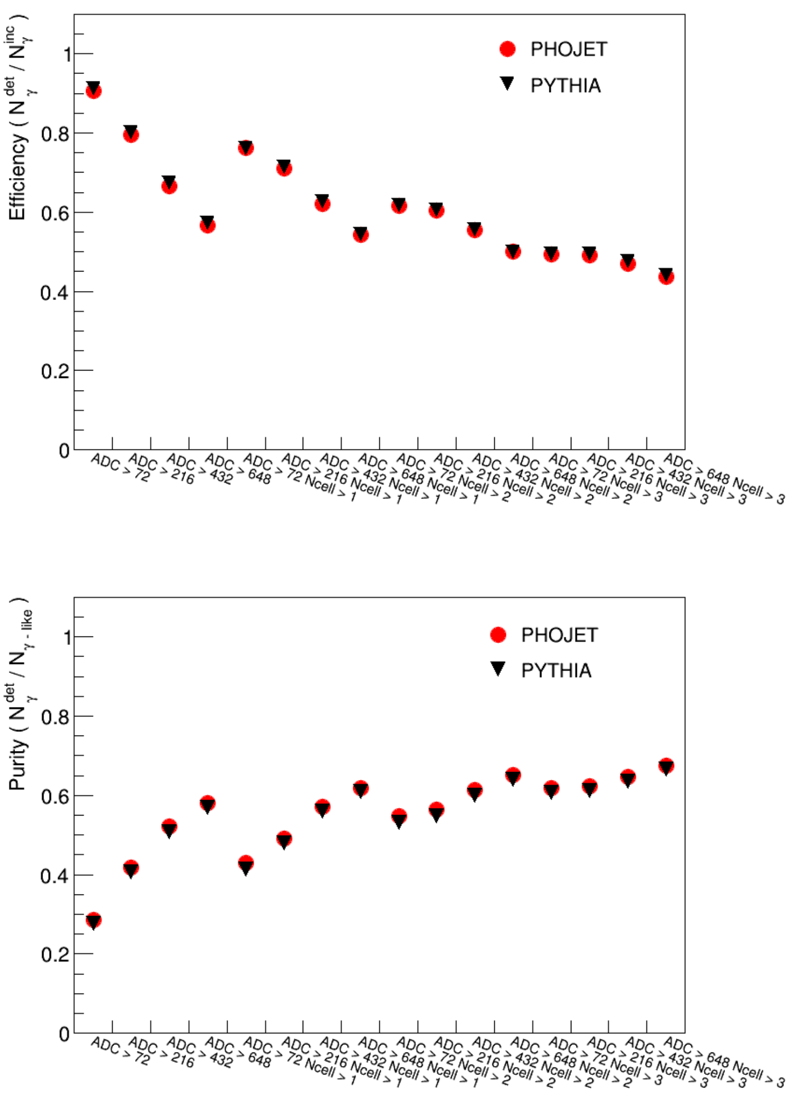

Figure 4.9: Efficiency (upper) and purity (lower) are plotted as a function of different thresholds. The circles represent the result from PHOJET and the triangles represent the result from PYTHIA.

For our study, occupancy may indicate how well simulations describe the data. The cell occupancies for the preshower detector plane is plotted in Fig. 4.10 as a function of pseudorapidity, with a bin size of 0.2 units. The occupancy is shown for experimental p-p data at 0.9 TeV along with results from PHOJET event generator in the presence of all the materials. The occupancy is overall low for p-p collisions at 0.9 TeV, going from less than 0.1% to 0.5%. The PHOJET generator underestimates the occupancy compared to the experimental data. The material budget is overall increased by 10% and the resulting occupancy is presented in the Fig. 4.10.

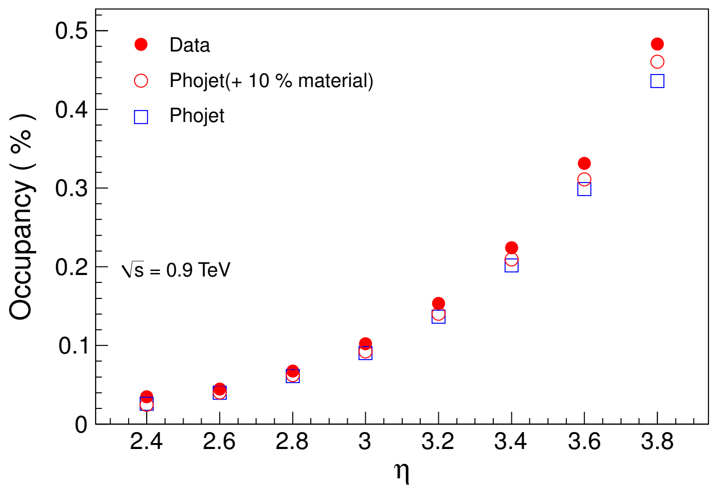

Figure 4.10: Occupancy as a function of pseudorapidity for p-p collisions at 0.9 TeV for data, PHOJET and PHOJET with 10% increased material.

This effect has been studied in detail for p-p at 0.9 TeV. The main reason is that at this energy, the multiplicity of charged particles for experimental data and MC (PHOJET) are close to each other. The occupancy study makes sense only if the multiplicities match. This is true only for 900 GeV. At higher energies, MC (PHOJET) multiplicities are much lower compared to the experimental data. Therefore, the study is not done for higher energies. While calculating the systematic error, it is assumed that the effect of upstream material is the same for all p-p collision energies.

4.3.6 Estimation of systematic uncertainties due to upstream material in front of the PMD

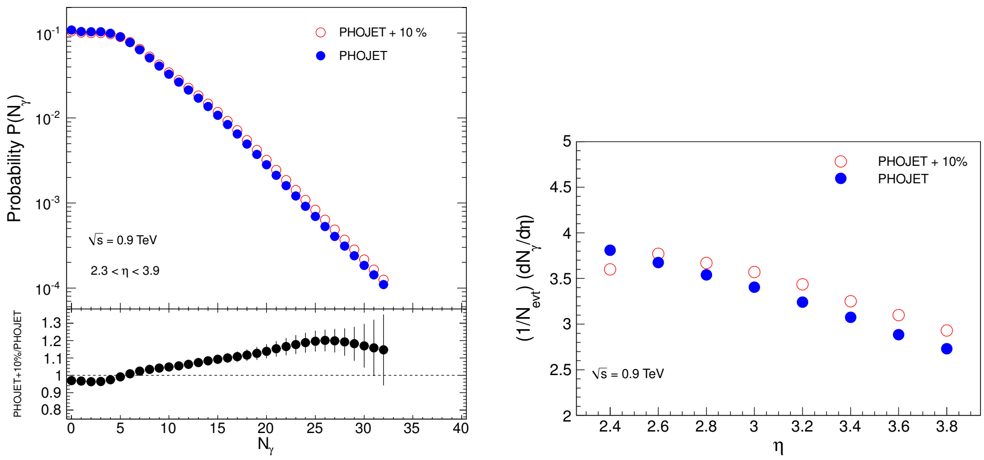

Figure 4.11: Left panel shows the unfolded multiplicity distributions of photons from PHOJET and PHOJET + 10% increased material at $\sqrt{s}$ = 0.9 TeV, lower half of the left panel shows the ratio of these distributions. In right panel, unfolded pseudorapidity distributions are shown for both the cases.

To estimate the systematic uncertainties due to upstream material in front of the PMD, PHOJET with default material and PHOJET with 10% increased material of AliRoot including PMD material (denoted as PHOJET + 10%) have been used. Response matrix has been taken from the PHOJET with default material and unfolding method has been performed over the measured multiplicities from the default PHOJET and PHOJET + 10% increased material at $\sqrt{s}$ = 0.9 TeV.

The two unfolded multiplicity distributions are shown in the left panel of Fig. 4.11. The lower half of the left panel shows the ratio of the two distributions. In the case of pseudorapidity distribution the unfolding method has been performed in each η bin for both cases. The difference between the two cases is quoted as the systematic errors due to material budget.

4.4 Data flow

The physics analyses have been performed over the reconstructed data. Pedestal subtraction, calibration and data clean up have been done before the reconstruction. The detailed procedure are discussed in the next sections. The schematic of simulation framework and the data flow of the PMD is shown in the Fig. 4.12.

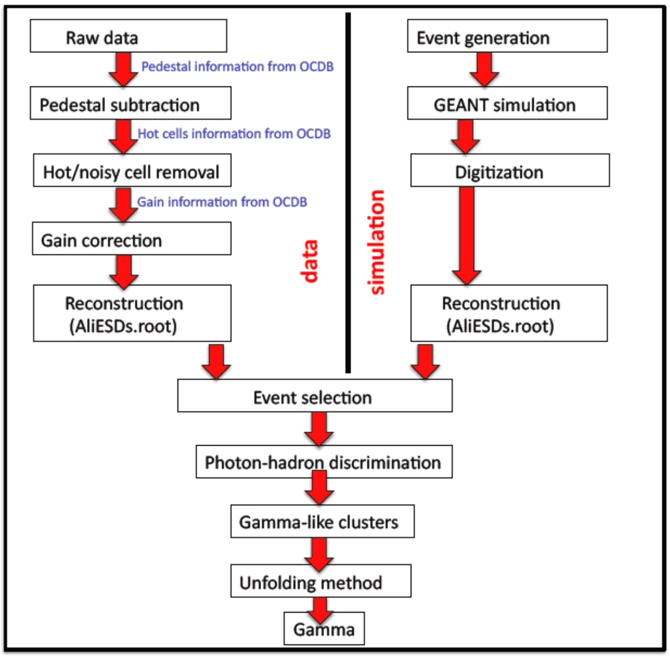

Figure 4.12: Schematic view of the simulation framework (right side of the line) and the data flow (left side of the line)

4.4.1 Zero suppression

After collisions occurred, signals are produced by the particles passing through the detector. The signals are stored above a threshold value which is basically electronic noise. This process is known as zero suppression and this is performed to reject the noise.

4.4.2 Pedestal Subtraction

Pedestal has been taken before each data run or a set of data runs taken consecutively. These pedestal runs are stored in the Offline Conditioned Data Base (OCDB). The pedestal values are subtracted from the real signals during the reconstruction of the data. In this way the electronic noise has been removed from the actual signal.

4.4.3 Data clean up

It is observed that some of the cells are fired very frequently in comparison to the other cells. The hit frequency of these cells are very high compared to others and ADC values of these cells are low. These cells are known as *hot cells*. To get clean data for analysis, these cells have to be removed before the reconstruction. Fig. 4.13 shows the hit frequency of each cell of a module. Hot cells are marked by the lines in the figure. It is found that there are some spikes in the lower ADC values of ADC distribution of the module due to the hot cells.

An algorithm is developed to find these hot sells. It is found that the cells within a particular η ring of width 0.1 over full ϕ are fired uniformly, i.e. the distribution of the number of hits in the cells within the η ring are expected to be Gaussian. For

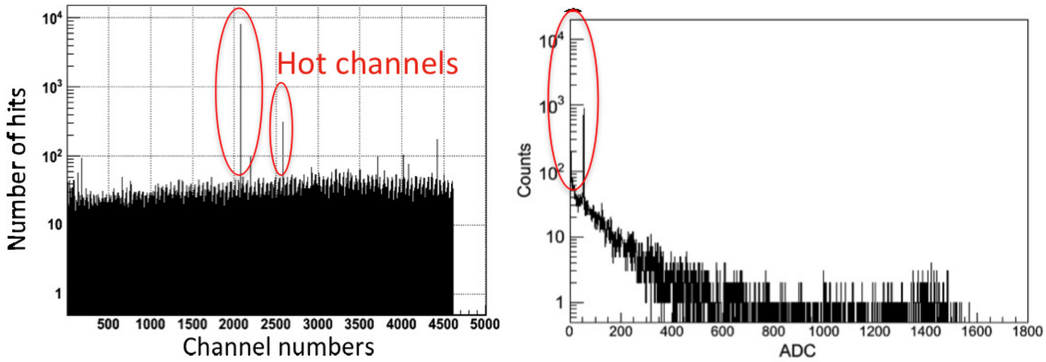

Figure 4.13: Left: number of hits of all the cells for a particular module before hot cells removal. Contours indicate the hot cells. Right: ADC distribution of the same module before the hot cells removal. spike inside the contour indicates the presence of hot cells.

noisy cells, distribution will deviate from the gaussian. The PMD planes have been divided into different η rings of width 0.1 and distributions of number of cells have been made for each of the η rings from the *raw data*. Each of the distribution has been fitted with a Gaussian function. One of such distributions are shown in the Fig. 4.14.

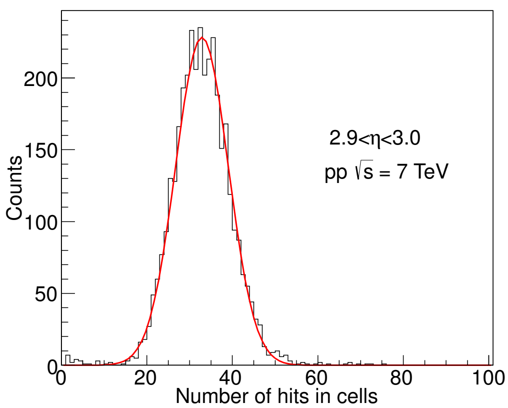

Figure 4.14: Distribution of number of hits of the cells within 2.9< η <3.0. The solid line is the Gaussian fit to data.

Mean and rms of the function have been obtained and *mean + constant* $\times$ *rms* has been set as a threshold. The cells where the number of hits exceed the threshold value are declared as "*hot cells*". The row-column information of these *hot cells* have been obtained and stored in the OCDB. These cells are excluded during the reconstructions of the raw data. Clean reconstructed data has been produced to analyze.

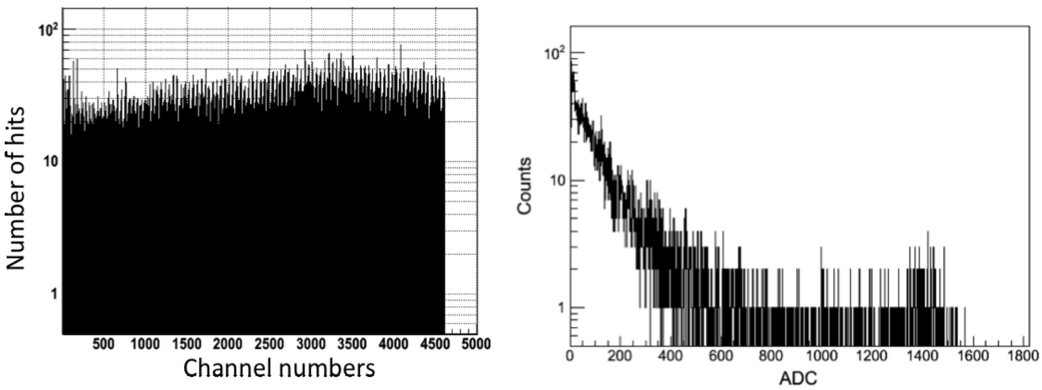

Figure 4.15: Left: number of hits are plotted for all the cells for a particular module after the hot cells removal. Right: ADC distribution of the same module after the hot cells removal.

4.4.4 Data reconstruction

As we discussed earlier when a photon passes through the Pb converter, it produces shower and produces signals in several cells. Thus, a cluster of cells are affected by a single photon. Where as, a charged particle affects one cell most of the time. Therefore, a clustering algorithm is developed to identify the cluster corresponding to each particle falling in the detector [80, 81]. According to this algorithm, a cluster is formed taking all the connected cells having non-zero energy deposition. This cluster is called super cluster and two super clusters are separated by the cells having zero energy deposition. This is called *crude clustering*, which is used in p-p collisions. In the case of Pb-Pb collisions particle density is very high which results in the overlap of the super clusters. Therefore, super clusters need to be divided by smaller clusters which are called $refined\ clusters$.

After the reconstruction, all information have been stored in terms of clusters. Total ADC of all the cells of the cluster is stored as a cluster ADC. Center of the cluster is stored as a cluster position (x, y, z). The cluster containing single cell stored as a isolated-cell cluster.

4.5 Data Analysis

The reconstructed data has been analyzed to get the multiplicity and pseudorapidity distribution of photons. In this section, the details of the data analysis have been presented for p-p collisions at $\sqrt{s}$ = 2.76 and 7 TeV.

4.5.1 Data sets and event selection

In this analysis the data set is chosen such a way that the acceptance is same for all the runs of that energy. The simulation data sets have been generated with the same acceptance as in the corresponding experimental data sets. These simulation data sets are called the anchor runs. The details of the data sets used in the analysis has been provided in the Table below (4.1).

The Fig. 4.16 shows the reconstructed z-vertex distribution for 2.76 and 7 TeV. The dotted lines represent the -10 to 10 cm of the distributions.

System	p + p
Collision energy	$\sqrt{s}$ = 2.76 and 7 TeV
Data sets used	2.76 TeV : LHC11a (pass3), 7 TeV : LHC10e (pass2)
Vertex cut	$-10 < V_z(cm) < 10$
Simulation data set	2.76 TeV : LHC12i1a, LHC12i1b, LHC13d17b 7 TeV : LHC11c3a, LHC11c3b, LHC13d17c
Material budget study	LHC11d4a (0.9 TeV)
Event generators used	PYTHIA6D6T, PYTHIA Perugia - 0, PHOJET

Table 4.1: Data sets

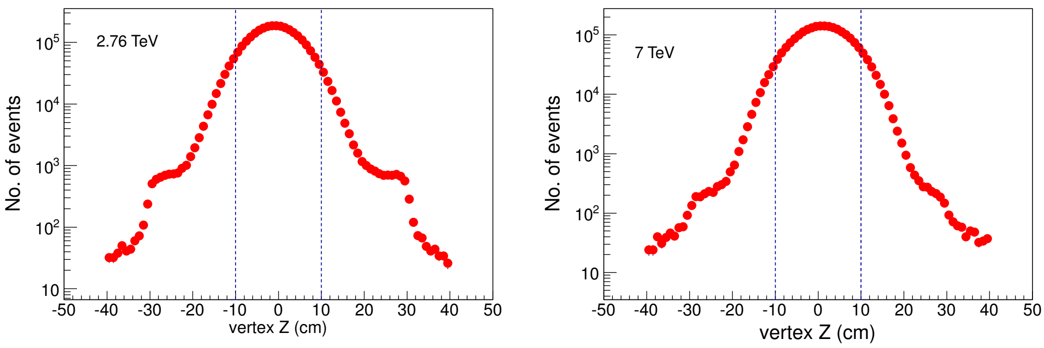

Figure 4.16: z-Vertex distributions in cm at $\sqrt{s}$ = 2.76 and 7 TeV. The dotted line indicate the selection of the z-vertex used in the analysis.

4.5.2 Trigger selection

For INEL analysis, we have used the triggered event sample requiring a logical OR between the signals from the SPD and VZERO detectors (MB_{OR}). For the NSD analysis, we have selected the event requiring a coincidence between the two sides of the VZERO detectors ($VZERO_{AND}$) [25].

4.5.3 Corrections for trigger and vertex reconstruction efficiency

Trigger and vertex reconstruction efficiency have been calculated using the latest simulated data where new diffraction tune has been implemented.

Trigger reconstruction efficiency is defined as :

$C_{trg} = \frac{\frac{1}{N_{All}}\frac{dN_{\gamma}}{d\eta}(All)}{\frac{1}{N_{Trigg}}\frac{dN_{\gamma}}{d\eta}(Trigg)}$;

Vertex reconstruction efficiency is defined as :

$C_{vtx} = \frac{\frac{1}{N_{Trigg}}\frac{dN_{\gamma}}{d\eta}(Trigg)}{\frac{1}{N_{TriggVtx}}\frac{dN_{\gamma}}{d\eta}(Triggvtx)}$;

Where,

$\frac{1}{N_{All}}\frac{dN_{\gamma}}{d\eta}(All)$ for all events.

$\frac{1}{N_{Trigg}}\frac{dN_{\gamma}}{d\eta}(Trigg)$ for all events which would have triggered the event to be recorded

$\frac{1}{N_{TriggVtx}}\frac{dN_{\gamma}}{d\eta}(TriggVtx)$ for all events which would have triggered the event to be recorded and a vertex would have been found

The resultant $\frac{dN_{\gamma}}{d\eta}$ is :

$\frac{1}{N}\frac{dN_{\gamma}}{d\eta}(Measured) \times C_{trg} \times C_{vtx}$;

The values of the trigger and vertex reconstructed efficiencies are shown in the table 4.2 below:

$\sqrt{s}(TeV)$	MB(OR) Trigger efficiency	Vertex reconstruction efficiency
2.76	0.886	0.924
7	0.851	0.928

Table 4.2: Trigger and vertex reconstruction efficiency

4.5.4 Acceptance of the PMD

During the data taking period some of the cells or some modules could be off due to some technical problems. This will reduce the geometrical acceptance of the detector. Therefore, we need to correct the results for detector acceptance. The correction has been performed using the simulation. The experimental data for the three energies are taken during different beam periods. Therefore, acceptance of the detector at each energy is different. The geometrical acceptance effect is taken into account in the simulation using anchor runs. In the MC anchor runs, the exact x-y (η - ϕ) acceptance of the detector has been produced as in experimental data. For two different collision energies XY scattered plots of hits of the preshower plane of PMD for experimental data is shown in the Fig. 4.17. X-axis shows the x position in *cm* and Y-axis represents the y positions in *cm*. The boxes with the numbers represent each module. The empty areas correspond to non-functional part of the PMD during the data taking time.

4.5.5 Uncorrected multiplicity ($N_{\gamma-like}$) and psedorapidity distribution ($dN_{\gamma-like}/d\eta$) of photons

To get the uncorrected photon multiplicity, which is generally called $N_{\gamma-like}$ distribution, a photon-hadron discrimination threshold has been applied over the total number of clusters. $N_{\gamma-like}$ is the photon rich sample but it also contains the charged particles contamination, which passes the threshold cut and split clusters of photons. To correct the $N_{\gamma-like}$ distribution for efficiency, acceptance and other detector effects, unfolding method with χ^2 minimization has been used [82, 83,

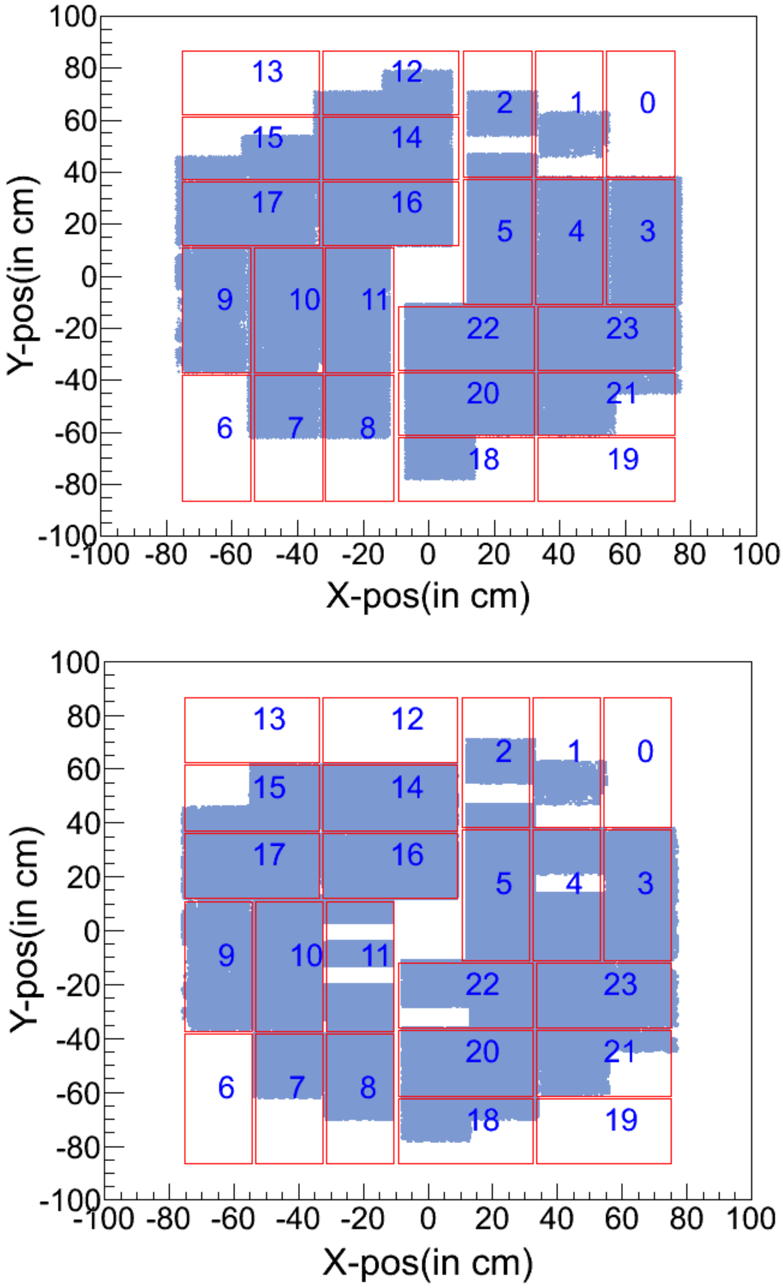

Figure 4.17: X-Y display of hits of the preshower plane of PMD for the experimental data. Different boxes represent different modules of the detector. Upper: at $\sqrt{s}$ = 2.76 TeV. Lower: at $\sqrt{s}$ = 7 TeV.

18]. Two different thresholds ($ADC > 432$ $(6\ MPV)$ $and\ ncell > 2$, $ADC > 648$ $(9\ MPV)$ $and\ ncell > 2$) have been used to check the robustness of the results (Fig. 4.18).

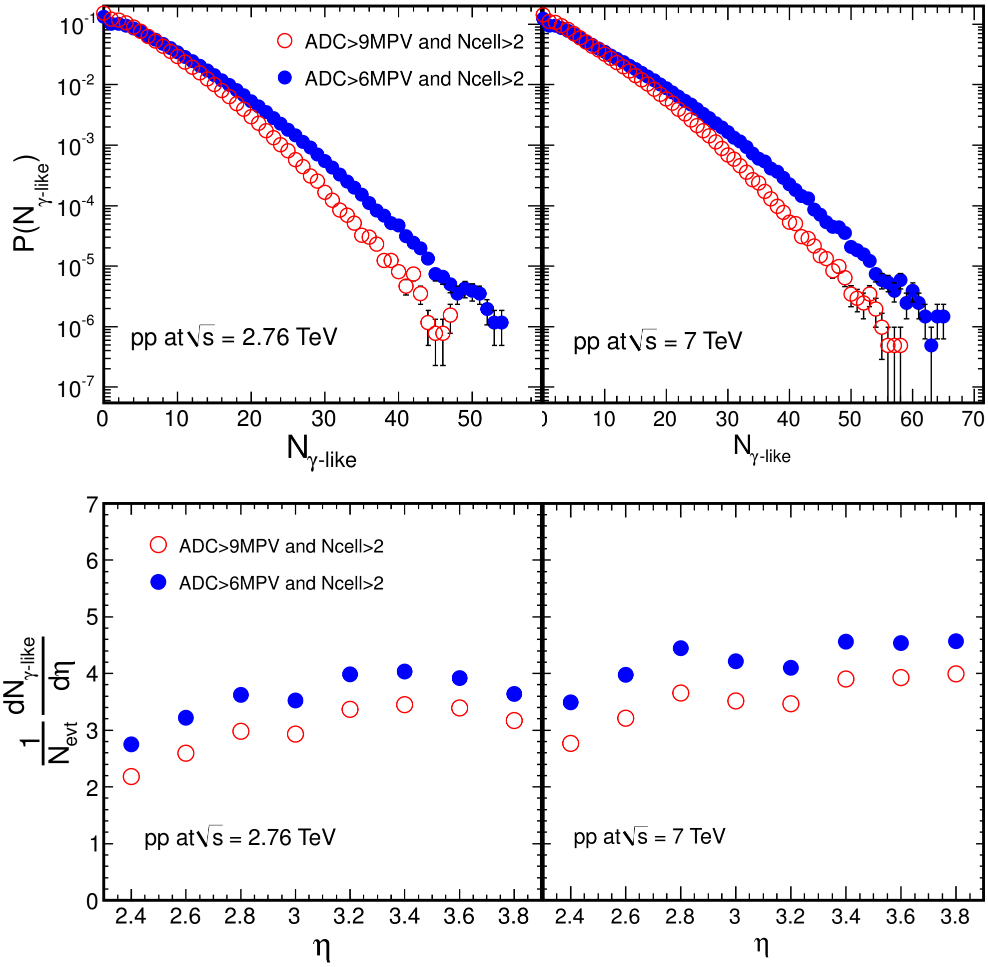

Figure 4.18: Top panel: $N_{\gamma-like}$ distributions for two different thresholds at both energies. Bottom panel: pseudorapidity distributions of $N_{\gamma-like}$ clusters for two different thresholds at both energies.

The bottom panel of Fig. 4.18 shows the uncorrected pseudorapidity distribution i.e. $dN_{\gamma-like}/d\eta$ as a function of η. Width of the each η bin is 0.2. To get the $dN_{\gamma}/d\eta$

unfolding method has been performed in each η bin.

4.5.6 Method of Unfolding

The detector effects can be described by a matrix R. In matrix notation R can be written as R_{mt} which gives the conditional probability that a collision with a true multiplicity t is measured as an event with the multiplicity m.

A true multiplicity spectrum $\hat{f}$ is corrupted by the detector effects, described by the detector response function R. So, the measured multiplicity spectrum $\hat{g}$ can be written as:

$$\hat{g} = R\hat{f} \tag{4.2}$$

From the detector only measured multiplicity $\hat{g}$ can be available. From the previous equation we can get the measured multiplicity as:

$$\hat{f} = R^{-1}\hat{g} \tag{4.3}$$

Determination of the true multiplicity $\hat{f}$ from the measured multiplicity $\hat{g}$ is called the unfolding.

χ^2 *minimization method* and *Bayesian method* have been utilized to unfold the $N_{\gamma-like}$ distributions.

χ^2 **minimization method**

Because of statistical fluctuations caused by the limited statistics of events used to create the response matrix, the matrix inversion can give large oscillation in results. A method of χ^2 minimization has been adopted to handle this problem. The unfolded multiplicity distribution is found by minimizing the χ^2 function, which is defined as:

$$\hat{\chi}^2(u) = \sum_m (\frac{g_m - \sum_t R_{mt} u_t}{e_m})^2 + \beta P(u) \tag{4.4}$$

Where e_m is the error in the measurement and $\beta P(u)$ is the regularization term that suppress the oscillation in the final solution. The regularization coefficient β is chosen such that, after minimization, the contribution of the first term in eq. 4.4 is of the same order as the number of degrees of freedom (the number of bins in the unfolding).

Bayesian method

An alternative method of unfolding is based on Bayes' theorem. According to this theorem, if A and B are two events, then the conditional probabilities of A with B given and B with A given, are related by the relation:

$$P(A|B) = \frac{P(B|A)P(A)}{P(B)} \tag{4.5}$$

where $P(A)$ and $P(B)$ are the probabilities for the event A and B respectively. $P(A|B)$ denotes the probability of event A under the condition of event B is true. $P(B|A)$ denotes the probability of event B under the condition of event A is true.

In our notation,

$$\bar{R}_{tm} = \frac{R_{mt} P_t}{\sum_{t'} R_{mt'} P_{t'}} \tag{4.6}$$

where P_t is a prior distribution of the true distribution. After obtaining $\bar{R}_{tm}$, the unfolded distribution (u) can be obtained as

$$u_t = \sum_m \bar{R}_{tm} g_m \tag{4.7}$$

The resultant f of an iteration is used as the new a prior distribution for the next iteration.

- χ^2 minimization method has been used to unfold the data and the bayesian method has been used to do study of the systematic error due to the two different methods of unfolding.

4.5.7 Performance of the unfolding method using simulated data

Two different sets of simulated data have been used to test the performance of the unfolding method. PHOJET [33, 34] and PYTHIA 6.4 [31, 32] tune D6T [84] event generators provide the simulated data. One set of the simulated data has been used to construct the response matrix which unfold the measured photon multiplicity from the other set.

Fig. 4.19 shows the response matrix constructed using the PHOJET event generator within $2.3 < \eta < 3.9$ in p-p collision at $\sqrt{s} = 2.76$ and 7 TeV. x-axis corresponds to true photon multiplicity and y-axis corresponds to measured photon multiplicity. True photon multiplicity refers to the distribution of the incident photons and measured photon multiplicity refers to the distribution of reconstructed photons after aplying photon-hadron discrimination thresholds. As discussed earlier, measured photon multiplicity is called $N_{\gamma-like}$ distribution.

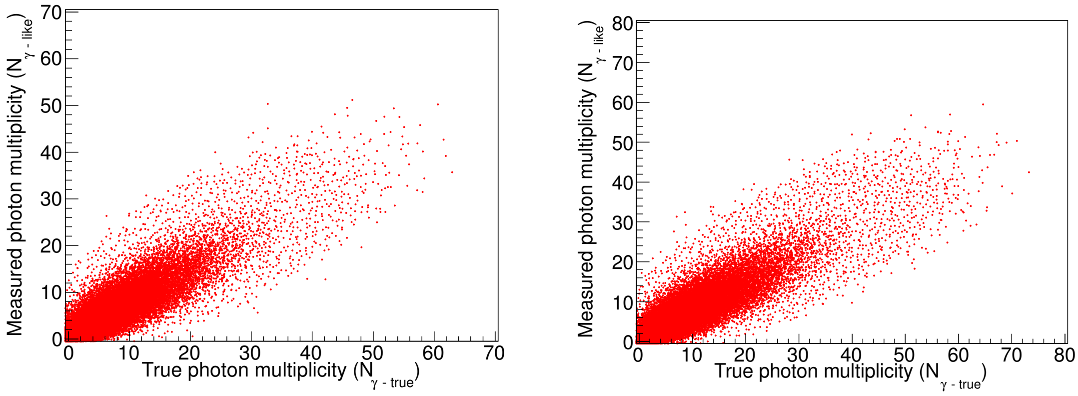

Figure 4.19: Response matrices for two different energies. left panel: 2.76 TeV, right panel: 7 TeV.

Different regularization functions like polynomial (degree 0), polynomial (degree1) and logarithmic, are used with various β values. The best combination has been found for the logarithmic function with the β value of 10^5 for both the energies. Fig. 4.20 shows the true, measured and unfolded photon multiplicity within $2.3 < \eta < 3.9$ in p-p collision at $\sqrt{s} = 2.76$ and 7 TeV with the best combination of regularization function and β value.

Similar procedure has been performed in each of the η bin from 2.3 to 3.9 in the case of pseudorapidity distribution of photons. The best combination has been found for each of the η bin is logarithmic function with the 10^3 β value. Fig. 4.21 shows the pseudorapidity distribution of the true photons, measured photons and unfolded photons.

From the Fig. 4.20 and Fig. 4.21 it is observed that after unfolding one can get back the true photon multiplicity from the measured one, which implies that this method can be used to unfold the measured spectrum from real data.

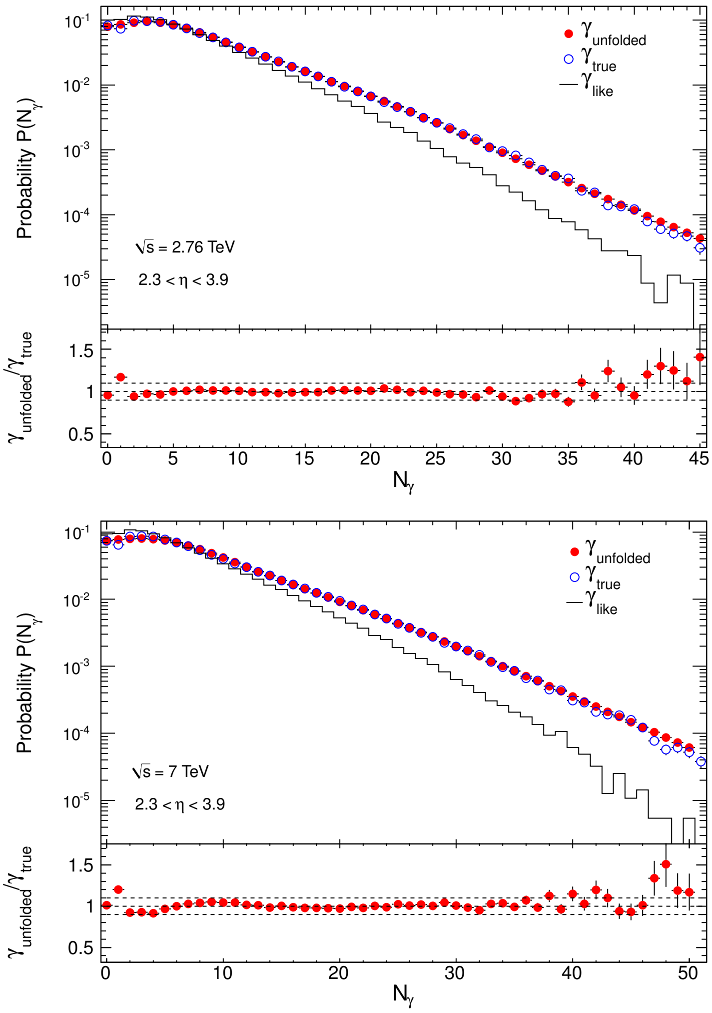

Figure 4.20: Test of the unfolding method using PHOJET event generator. Solid line represents measured photon multiplicity. Open circles and solid circles are stand for true and unfolded photon spectrums. Lower half of the figure represents the ratio between unfolded and true photon spectrum. upper panel: 2.76 TeV, lower panel: 7 TeV

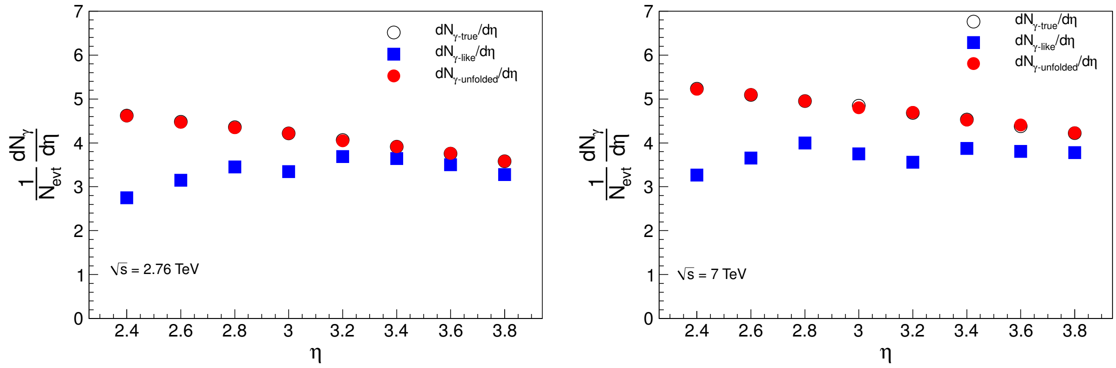

Figure 4.21: Test of the unfolding method in pseudorapidity distribution using PHOJET event generator. Left panel: 2.76 TeV; right panel: 7 TeV.

4.5.8 Corrected photon spectra

$N_{\gamma-like}$ distributions described in the section 4.5.5 have been unfolded using the response matrices described in the section 4.5.7 with the best combination of the regularization functions and β values. The unfolded spectrum is corrected further for trigger and vertex reconstruction efficiencies (see section 4.5.3). Fig. 4.22 shows the corrected multiplicity and pseudorapidity distribution of photons within $2.3 < \eta < 3.9$ for different thresholds at both the energies.

It is shown that after unfolding the corrected results are independent of the applied thresholds. This shows the robustness of our results.

4.5.9 Study of the systematic uncertainties

In order to study the systematic uncertainties the analysis has been performed varying different conditions, such as:

- Two different photon-hadron discrimination thresholds have been applied.

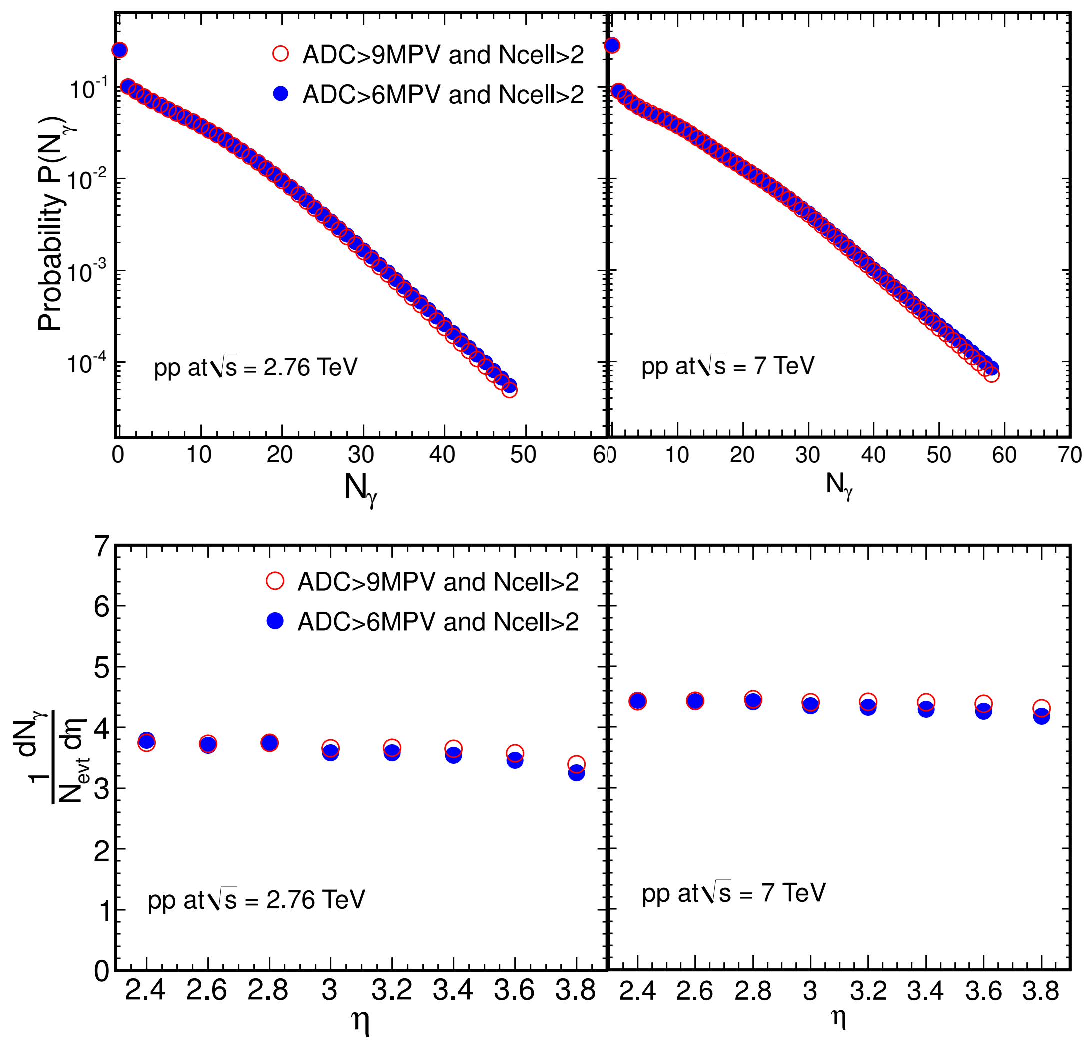

Figure 4.22: Multiplicity and pseudorapidity distributions of photons for two different thresholds after unfolding. Left panel: 2.76 TeV, right panel: 7 TeV.

- Two different event generators, PHOJET and PYTHIA6D6T have been used to unfold the data.
- The density of the material in the tracking system i.e. the material budget has been increased by 10%.
- Two different method of the unfolding χ^2 minimization and Bayesian method have been performed.
- Different regularizations functions have been used to unfold the distributions.

For each of the sources photon spectra have been obtained (upper panel of the Fig 4.23). The lower panel of the Fig. 4.23 shows the pseudorapidity distributions of photons for different sources. These are used to calculate the systematic uncertainties.

Source	2.76 TeV (0 -10)	7 TeV (0 -10)
Effect of upstream material	3 - 5 %	3 - 5 %
Discrimination thresholds (MIP and ncell cuts)	0.02 - 0.11 %	0.11 - 0.25 %
Method of unfolding (Event generators)	0.89 - 7.5 %	1.19 - 7.8 %
Method of unfolding (χ^2 and Bayesian method)	1.18 - 8.47 %	4.68 - 11.68 %
Different regularizations functions	0.78 - 2.5 %	2.6 - 2.8 %
Total	3.4 - 12.6 %	6.2 - 15.1 %

Table 4.3: The magnitude of the different sources of systematic errors in multiplicity distribution at each energy. The values are quoted here for 1-10 multiplicity.

The contribution from different sources of systematic errors have been quoted in the Table 4.3 and 4.4 both for multiplicity and pseudorapidity distribution of the photons.

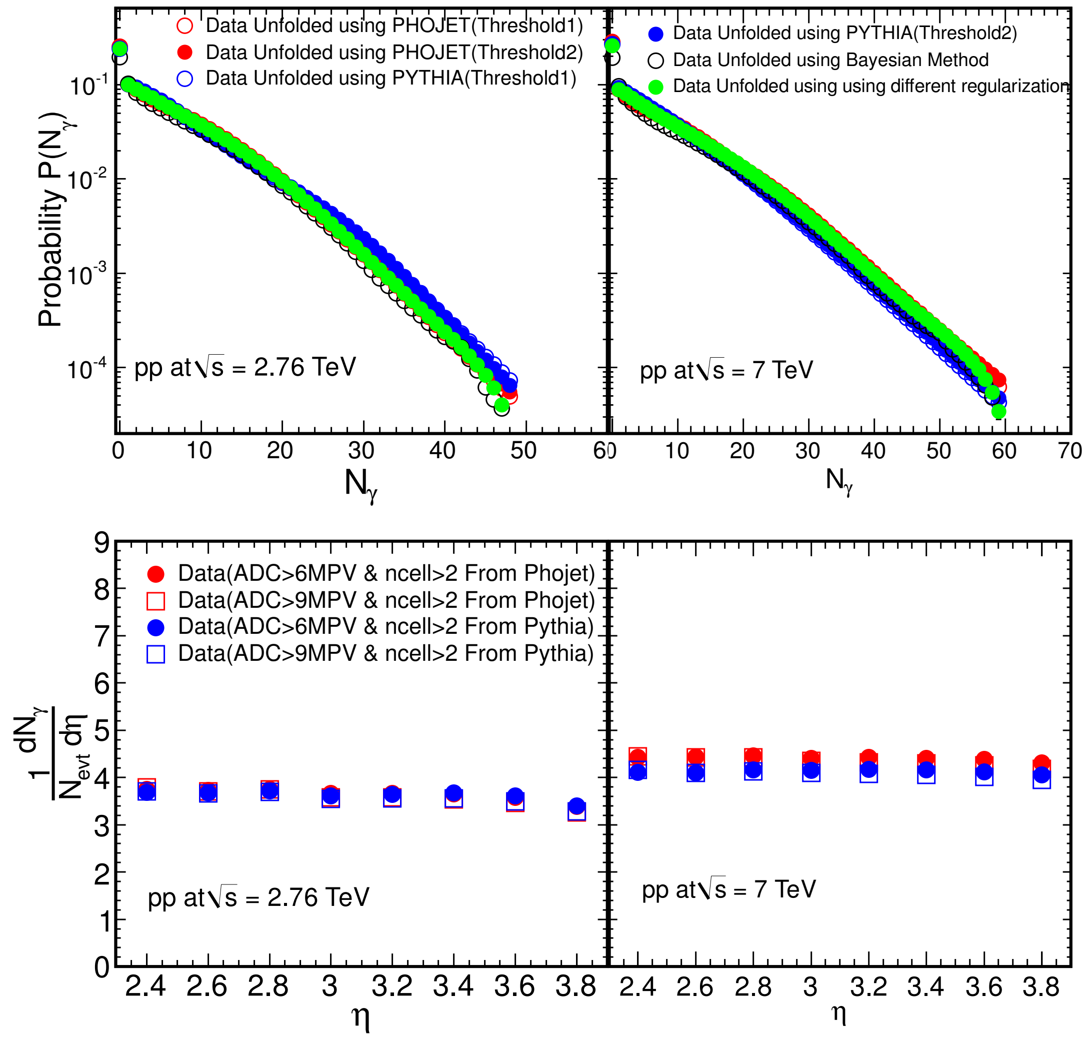

Figure 4.23: Multiplicity and pseudorapidity distributions of photons for different sources of systematic uncertainties. Left panel: 2.76 TeV; right panel: 7 TeV.

Source	2.76 TeV	7 TeV
Effect of upstream material	7 %	7 %
Discrimination hresholds (MIP and cell cuts)	1 - 2 %	1 - 2%
Method of unfolding (Event generators)	1 - 2 %	3 - 5 %
Method of unfolding (χ^2 and Bayesian method)	negligible	negligible
Different regularizations functions	negligible	negligible
Total	7 - 7.5 %	8 - 8.5 %

Table 4.4: The magnitude of the different sources of systematic errors and their contributions in the pseudorapidity distributions.

4.6 Results and discussions

In this section, multiplicity and pseudorapidity distributions of photons are presented for two centre-of-mass energies and compared to results of other experiments and to models.

4.6.1 Comparison to model predictions

Two different event generators PHOJET and PYTHIA Perugia-0 [85] have been used for model comparisons. Fig. 4.24 shows the multiplicity spectra of photons for INEL events within $2.3 < \eta < 3.9$ with the systematic errors as a shaded region. Two different lines correspond to two different models. It is observed that both the models underpredict the data at both energies. The difference between the data and the MC predictions is more in the higher multiplicity region at both the energies.

Fig. 4.25 shows the pseudorapidity density of the photons for the INEL events with the models predictions from PHOJET and PYTHIA Perugia-0. It is observed that PHOJET is closer to the data but both the models under predict the data at both energies.

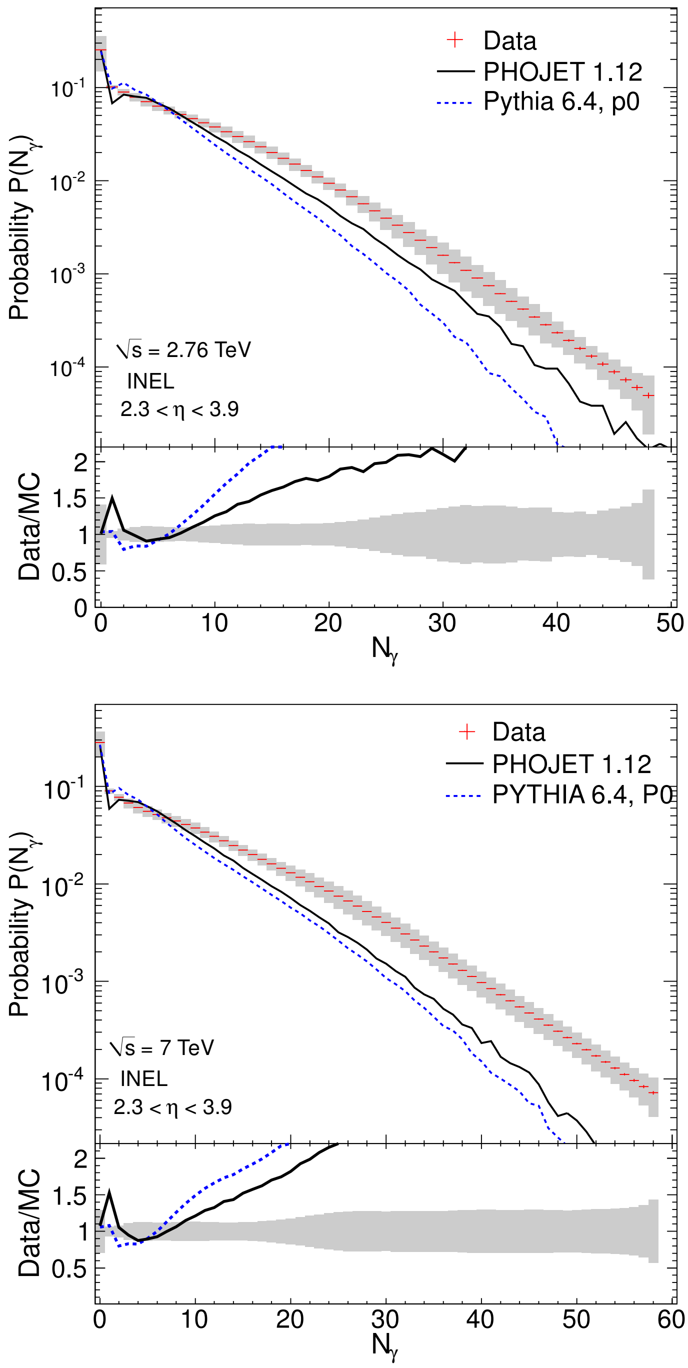

Figure 4.24: Multiplicity distribution of photons for INEL events within $2.3 < \eta < 3.9$. The error bars in the data points are statistical uncertainties and the shaded regions represents the systematic uncertainties. Predictions are shown from the PHOJET (solid line) and PYTHIA Perugia-0 (dashed line) event generators. Lower half of the panel shows the ratio between the data and MC. Upper panel: 2.76 TeV, lower panel: 7 TeV.

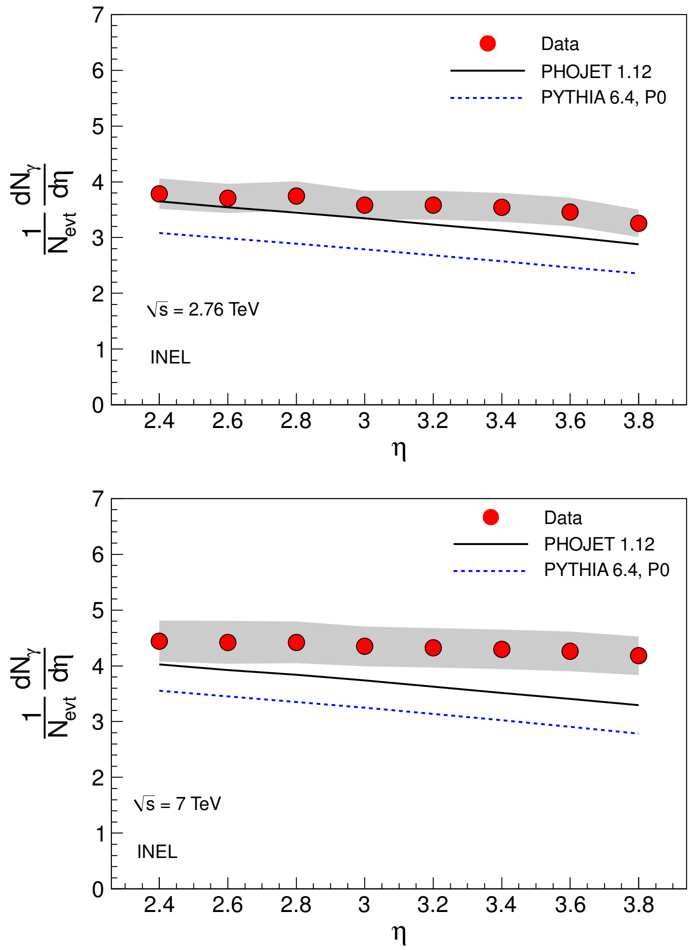

Figure 4.25: Pseudorapidity distribution of photons for INEL events within 2.3 $< \eta <$ 3.9. The shaded regions represents the systematic uncertainties. Statistical error bars are within the symbol size. Predictions are shown from the PHOJET (solid line) and PYTHIA Perugia-0 (dashed line) event generators. Upper panel: 2.76 TeV, lower panel: 7 TeV.

4.6.2 NBD fitting to the multiplicity distribution

The photon multiplicity distributions have been fitted with a Negative-Binomial Distribution (NBD) at both energies. The results have been presented in the upper panel of the Fig. 4.26. It is observed that single NBD function could not explain the high multiplicity region of the spectra. Lower panel of the Fig. 4.26 shows the multiplicity distribution fitted with a double NBD function, which is the sum of two NBD functions. It is found that double NBD function describes the spectra better than the single NBD at both energies.

The fit parameters for both the fitting functions have been shown in the Table 4.5 and 4.6.

$\sqrt{s}$ in TeV	k	m	χ^2/ndf
2.76	1.41 ± 0.05	6.999 ± 0.130	26.99 / 45
7	1.276 ± 0.053	8.724 ± 0.185	18.2 / 55

Table 4.5: Fit parameters for single NBD function.

$\sqrt{s}$ in TeV	k (k1, k2)	m (m1, m2)	W	χ^2/ndf
2.76	2.59 ± 0.19 1.39 ± 0.66	9.72 ± 0.30 2.13 ± 0.26	0.34 ± 0.01	0.08 / 42
7	6.329 ± 0.49 3.11 ± 0.35	14.39 ± 1.45 6.33 ± 0.49	0.29 ± 0.01	0.59 / 52

Table 4.6: Fit parameters for double NBD function.

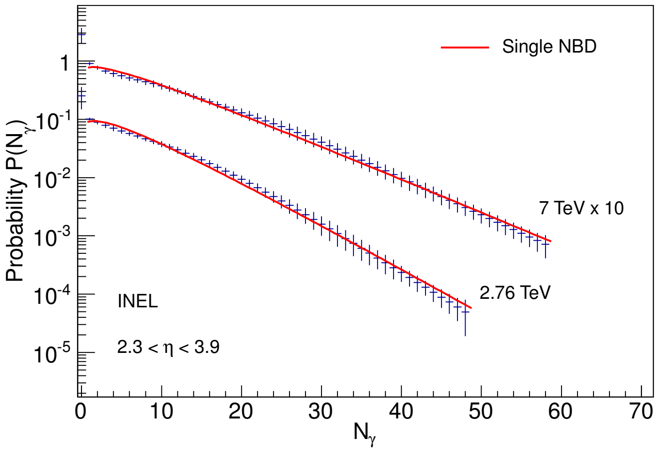

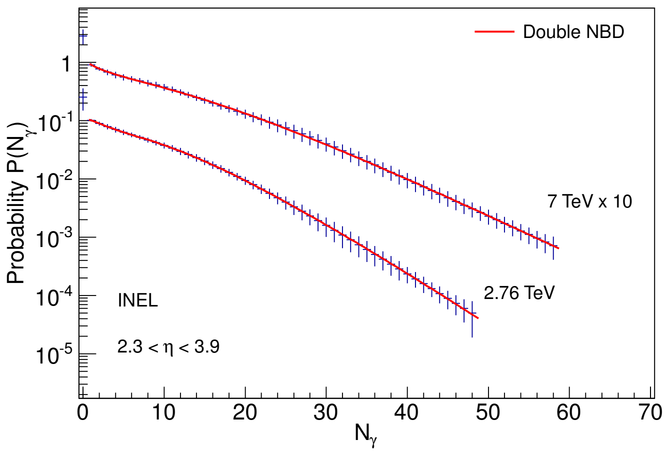

Figure 4.26: Multiplicity distribution of photons for INEL events within $2.3 < \eta < 3.9$ fitted to NBD functions. The solid lines represent the NBD functions. The error bars in the data points are both statistical and systematic uncertainties. Upper panel: spectra fitted to single NBD function, Lower panel: spectra fitted to double NBD function.

4.6.3 Centre of mass energy dependence of photon multiplicity

Centre of mass energy dependence of the average photon multiplicity has been presented for NSD events within $2.3 < \eta < 3.9$ from $\sqrt{s} = 0.2$ TeV to 7 TeV in the Fig. 4.27. For lower centre of mass energies data points have been taken from the UA5 experiment [86]. 0.9 TeV data point of the ALICE experiment has been taken from the [87]. The data points have been fitted with a logarithmic function as well as a power law. The fit parameters have been shown in the figure. It is observed that the average photon multiplicity within ($2.3< \eta <3.9$) increases with $\sqrt{s}$ as $\ln\sqrt{s}$ as well as a power law.

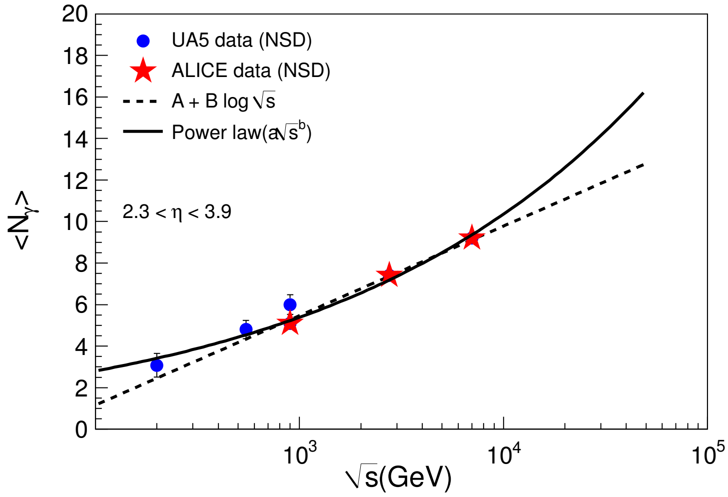

Figure 4.27: Average photon multiplicity as a function of centre of mass energy. Solid circles represent the data points from UA5 experiment and the stars are from the ALICE experiment.

4.6.4 Limiting fragmentation behavior

Fig. 4.28 shows the energy dependence of limiting fragmentation for inclusive photons at $\sqrt{s}$ = 0.9, 2.76 and 7 TeV within $2.3 < \eta < 3.9$. 0.9 TeV data points have been taken from the ref [87]. The different lines represent the expectation from the PHOJET event generator at different energies. The beam rapidities (y_{beam}) at $\sqrt{s}$ = 0.9, 2.76 and 7 TeV are 6.86, 7.98 and 8.97 respectively.

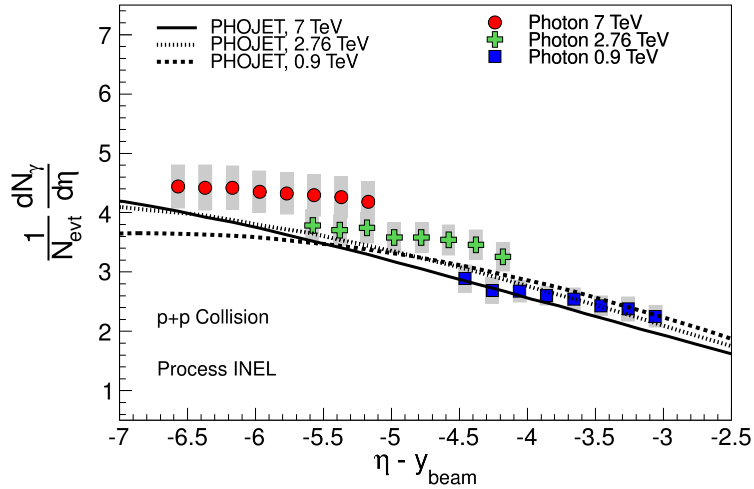

Figure 4.28: Pseudorapidity density as a function of $\eta - y_{beam}$. Different symbols stand for different centre of mass energies. The expectations from the PHOJET are shown in different lines.

4.7 Summary

Multiplicity and pseudorapidity distributions of photons have been presented for p-p collisions at $\sqrt{s}$ = 2.76 and 7 TeV in the forward rapidity region ($2.3 < \eta < 3.9$) using the Photon Multiplicity Detector (PMD) in ALICE. A detailed study has been made to understand the effects of the upstream material in front of the PMD. It is found that the within PMD coverage there are very less material in front of PMD. It has been shown that the material effects could be reduced a lot after applying the photon-hadron discrimination cut used in the analysis. The corrected results have been compared with the different models like PYTHIA and PHOJET. None of them describes the multiplicity and pseudorapidity distribution of photons. The photon multiplicity spectra have been fitted with both single and double NBD functions. It is found that double NBD function fits better than that of single NBD. Centre of mass energy dependence of average photon multiplicity has been presented from 0.2 to 7 TeV and fitted with both logarithmic and power law functions. The energy dependence of the longitudinal scaling of inclusive photons has been discussed.

5

Pseudorapidity distributions of photons in p-Pb collisions at forward rapidity

Measurement of the pseudorapidity density of the inclusive photons in p-Pb collisions at $\sqrt{s_{NN}} = 5.02$ TeV using the Photon Multiplicity Detector (PMD) will be discussed in this chapter. The analysis procedure will be described in detail. The results along with the model predictions will be presented.

5.1 Introduction

The effects of thermalization and collective evolution are thought to play an important role in heavy-ion collisions [88]. p-Pb collisions at the LHC provide an opportunity to study the physics of the initial states of the heavy-ion collisions without these effects. In addition, this measurement can shed insight on the effect of an extended nuclear target on the dynamics of soft and hard scattering processes and subsequent particle production. Historically, measurements of charged particle pseudorapidity distributions have provided important insight on particle production dynamics in p-A collisions [89] and have provided new constraints on the existing models.

Recently ALICE experiment has published the pseudorapidity density of the inclusive charged particles at $\sqrt{s_{NN}}$ = 5.02 TeV for non-single diffractive (NSD) events within $|\eta_{lab}| < 2$ [90]. The results have been presented with different model predictions in the Fig. 5.1. It is noticed that DPMJET [40] and HIJING 2.1 [37], where the gluon shadowing parameter was tuned to describe the experimental data in d-Au collisions at $\sqrt{s_{NN}}$ = 0.2 TeV, give values that are closest to data and also describe the shape of distribution very well.

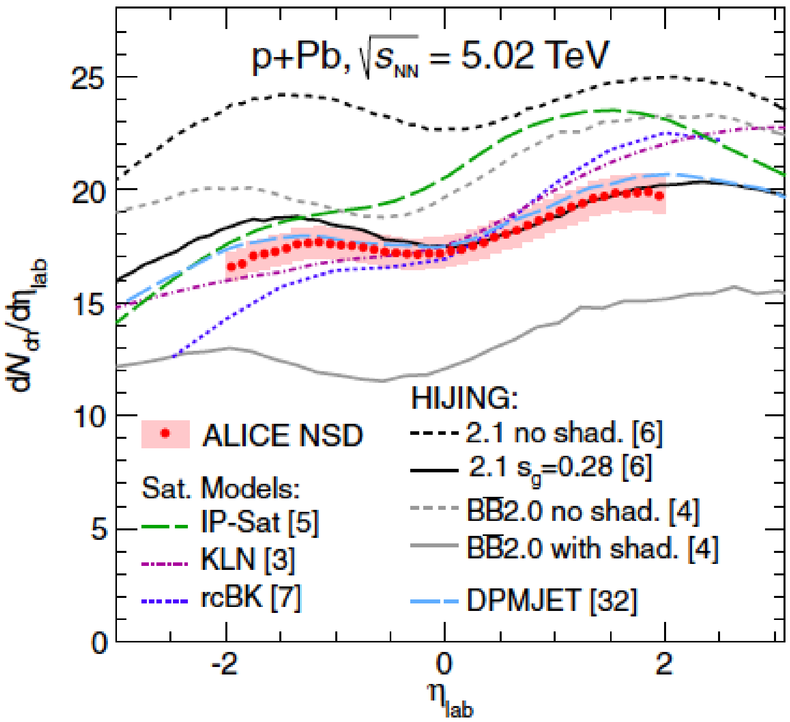

Figure 5.1: Pseudorapidity distributions of inclusive charged particles in p-Pb collisions at $\sqrt{s_{NN}}$ = 5.02 TeV within $|\eta_{lab}| < 2$ for NSD events from ALICE experiment [90]. The solid points are data. The shaded region is the systematic uncertainty to the data points. The different lines represent the expectations from different theoretical models and event generators.

In this work pseudorapidity density of the inclusive photons in p-Pb collisions at $\sqrt{s_{NN}} = 5.02$ TeV have been performed for Minimum-Bias (MB) events as well as different centrality classes within $2.3 < \eta < 3.9$. The new measurement extends the study of particle densities in proton-nucleus collisions into the forward rapidity and provides new constrains on the description of particle production at forward rapidity region.

5.2 Analysis details

The data reconstruction procedure such as zero suppression, pedestal subtraction, data clean up and clustering are the same as in the p-p collisions and already discussed in the *chapter 3*. As discussed earlier, the analysis has been performed over the data sets which have the same geometrical acceptance. The simulation data sets have been generated with the same acceptance as in the corresponding experimental data sets. The details of the data sets used in the analysis has been provided in the Table below (5.1).

System	p + Pb
Collision energy	$\sqrt{s_{NN}} = 5.02$ TeV
Data sets used	LHC13b (pass3)
Trigger class	kINT7
Vertex cut	$-10 < V_z(cm) < 10$
Centrality selection	V0A
Simulation data set	LHC13b-efix-p4
Event generators used	DPMJET

Table 5.1: Data sets

Fig. 5.2 shows the reconstructed z-vertex distribution in p-Pb collisions. The dotted line represents the -10 to 10 cm of the distribution.

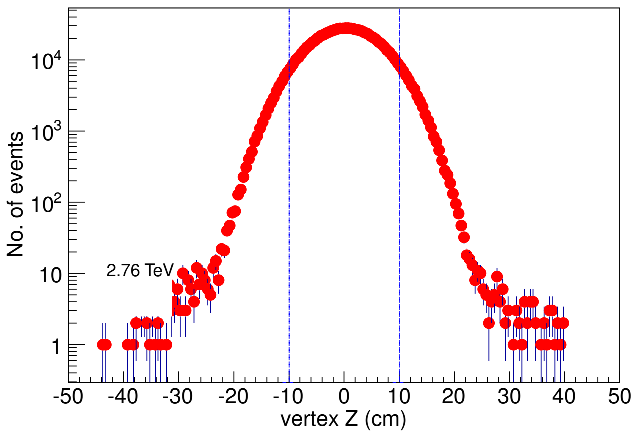

Figure 5.2: z-vertex distributions in p-Pb collisions.

5.3 Acceptance of the detector

Acceptance of the preshower plane has been presented for the experimental data of the p-Pb collisions. Fig 5.3 shows the X-Y display of the hits of the preshower plane of the detector. X axis is the x position in *cm* and Y axis represents the y position in *cm*. Each box represents the each module. The empty areas correspond to non-functional part of the PMD during the data taking time. Same acceptance has been produced in the simulated data to take care of the acceptance correction.

5.4 Centrality selection

In ALICE experiment centrality has been determined using VZERO-A (V0A) detector (*chapter2, section 2.4.3*) for p-Pb collisions [91]. Multiplicity distribution from

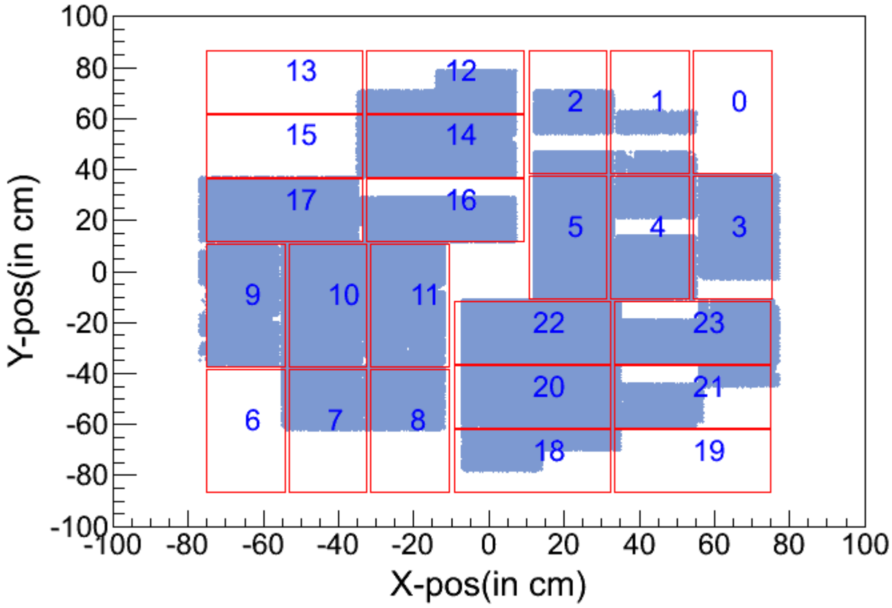

Figure 5.3: X-Y display of the preshower plane of PMD in p-Pb collisions. Different boxes represent different modules of the detector.

the V0A detector has been fitted with a MC Glauber model and NBD function. The centrality has been measured from the fitted line. Fig. 5.4 shows multiplicity distribution fitted with NBD-Glauber function.

5.5 Uncorrected psedorapidity distribution ($dN_{\gamma-like}/d\eta$) of photons

Photon-hadron discrimination threshold has been applied over the total number of clusters to get the $N_{\gamma-like}$ clusters. These are the photon rich clusters. The pseudorapidity density of $N_{\gamma-like}$ clusters have been corrected for detector efficiency and purity using the simulation. Two different thresholds *(ADC > 432 (6 MPV)*

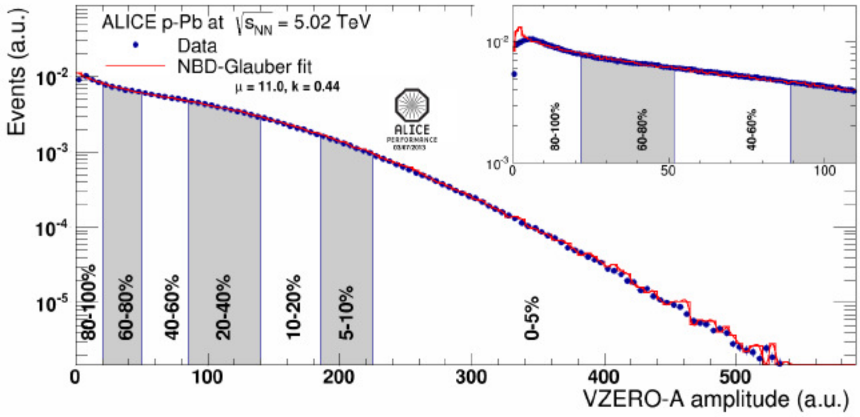

Figure 5.4: V0A multiplicity with NBD-Glauber fit showing different centrality classes [91].

and ncell > 2, ADC > 648 (9 MPV) and ncell > 2) have been used to check the robustness of the results (Fig. 5.5).

5.6 Efficiency and Purity

As discussed earlier, $N_{\gamma-like}$ clusters are obtained after applying the photon-hadron discrimination thresholds. $N_{\gamma-like}$ sample contains some contaminations from the charged particles and there is a loss of a fraction of photons. The contamination and losses are quantitatively determined in simulation in terms of *purity* and *efficiency* respectively.

As discussed in the *chapter 3*, the *efficiency* (E_γ) is defined as the ratio of number of identified photons ($N_{\gamma_{detected}}$) over the discrimination threshold to the number of incident photons ($N_{\gamma_{incident}}$) within the same coverage:

$$E_\gamma = \frac{N_{\gamma_{detected}}}{N_{\gamma_{incident}}}. \tag{5.1}$$

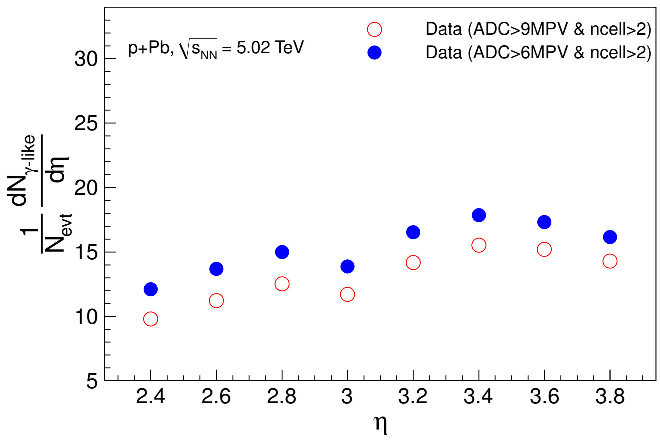

Figure 5.5: $dN_{\gamma-like}/d\eta$ as a function of η. Two different symbols are for two different thresholds.

The *purity* P_γ is defined as the ratio of number of identified photons ($N_{\gamma_{detected}}$) over the discrimination threshold to the number of γ_{like} clusters within the same coverage:

$$P_\gamma = \frac{N_{\gamma_{detected}}}{N_{\gamma_{like}}}. \tag{5.2}$$

Experimental data provides the $N_{\gamma-like}$ clusters. To get the number of photons incident to the detector (N_γ), $N_{\gamma-like}$ clusters are corrected by E_γ and P_γ which are calculated using simulation:

$$N_\gamma = N_{\gamma-like} \times \frac{P_\gamma}{E_\gamma}. \tag{5.3}$$

To calculate the efficiency and purity values DPMJET MC event generator has been used in an identical experimental situation corresponding to p-Pb collisions at $\sqrt{s_{NN}}$ = 5.02 TeV. As discussed in the *chapter 3*, acceptance of the detector has been implemented in the simulation as it is in the experimental data. Therefore, the efficiency and purity calculated using this simulation are the acceptance folded.

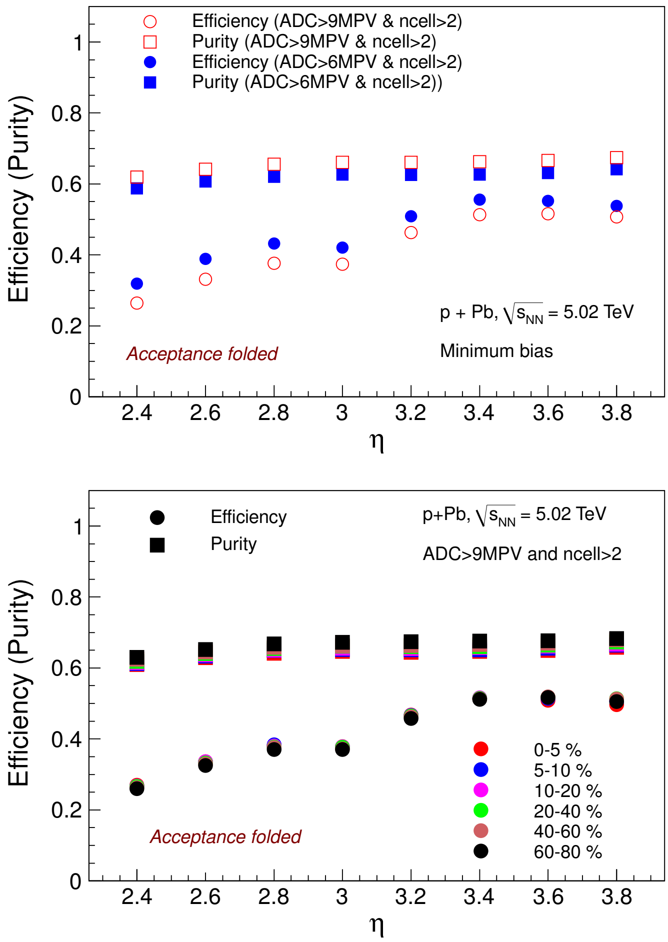

Figure 5.6: Efficiency and purity (acceptance folded) as a function of η in p-Pb collisions at $\sqrt{s_{NN}} = 5.02$ TeV. Top panel for minimum bias events. Different symbols are for different thresholds. Bottom panel: efficiency and purity as a function of η for different centrality classes.

Upper panel of the Fig. 5.6 shows the efficiency and purity as function of η for two different discrimination thresholds. It is observed that for higher threshold cut purity is higher, but efficiency becomes low. Centrality dependence of efficiency and purity have been presented in the lower panel of the Fig. 5.6. It is observed that efficiency and purity change very marginally with centrality.

5.7 Corrected results

Pseudorapidity density of the γ_{like} clusters has been corrected using the acceptance folded efficiency and purity values described in the previous section. Fig. 5.7 shows the corrected pseudorapidity density ($dN_{\gamma-like}/d\eta$) as a function of η for two different thresholds for minimum bias (MB) events. It is found that after the correction the pseudorapidity distributions are very similar for two different discrimination thresholds. This shows the robustness of the result. The difference will contribute as the systematic uncertainty to the data. Dashed line shows the expectation from the DPMJET event generator. It is observed that DPMJET explains the data well.

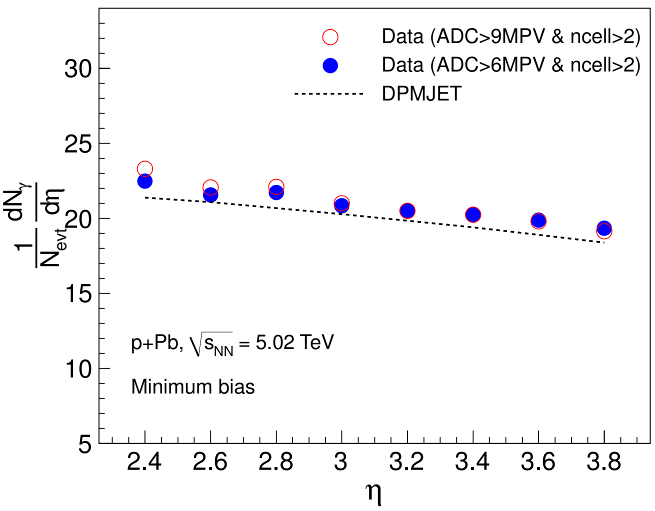

Figure 5.7: Pseudorapidity distribution of photons in p-Pb collisions at $\sqrt{s_{NN}}$ = 5.02 TeV. Two different symbols are for two different thresholds. The dashed line represents the expectation from DPMJET event generator.

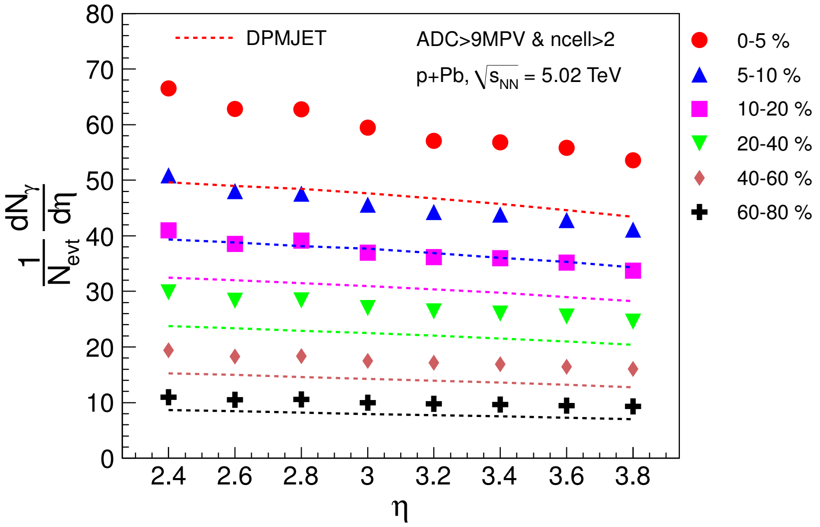

Figure 5.8: Pseudorapidity distribution of photons in p-Pb collisions at $\sqrt{s_{NN}}$ = 5.02 TeV for different centrality classes. The dotted lines represent expectations from DPMJET event generator for different centralities

Centrality dependence of the pseudorapidity distribution of photons has been shown in the Fig. 5.8. The results are presented for 0-5%, 5-10%, 10-20%, 20-40%, 40-60% and 60-80% centrality. The results are corrected for efficiency and purity for each centrality class (see Fig. 5.6). It is observed that top central collisions produce the largest number of photons and photon production reduces towards the peripheral collisions. The results are compared with the expectation from DPMJET event generator. It is observed that DPMJET underestimates the data at all centrality classes.

5.8 Summary

Pseudorapidity density of inclusive photons in p-Pb collisions at $\sqrt{s_{NN}} = 5.02$ TeV has been presented in this chapter. Data has been corrected using the simulation, generated with same conditions as in the data. The results have been presented for both MB events and different centrality classes. The centrality has been determined from V0A detector. The results have been compared with DPMJET event generator. It is observed that the expectation from DPMJET is close to data for MB events, but underestimates the data for different centrality classes.

The results resented in this chapter are in very preliminary stage. To finalize the result the followings steps should be performed:

- The analysis should be performed over all the available data sets.
- Systematic uncertainties to be calculated as discussed in the *chapter 3*.
- Another event generator should be used to correct the data.
- Different event generators and theoretical models could be used for comparison with final result to understand the existing underlying physics.

6

Forward-backward multiplicity correlations in p-p collisions at $\sqrt{s}$ = 0.9, 2.76 and 7 TeV

In this chapter the forward-backward multiplicity correlations in p-p collisions at $\sqrt{s}$ = 0.9, 2.76 and 7 TeV will be discussed. Data from the ALICE experiment along with different model predictions will be presented.

6.1 Introduction

The study of correlations among particles produced in different rapidity regions may provide an understanding of the elementary (partonic) interactions which lead to hadronization. Since it is believed that, correlation of particles produced in the early stage of the collisions spread over a large rapidity interval, the measurement of the long-range rapidity correlations of the produced particle multiplicities could give us some insight into the space-time dynamics of the early stages of the collisions.

Forward-backward (F-B) multiplicity correlations have been studied across a wide range of energies and colliding species [92, 93, 94, 95, 96, 97, 43, 98, 99, 47]. From these previous measurement of forward backward correlation several physical interpretations have been made. The correlations over small range in rapidity are believed to be dominated by short-range correlations which are due to the particles produced from cluster decay, resonance decay or jet correlation and those extending over a wide range in pseudorapidity could be interpreted due to multiple parton interactions [100]. It is argued that dual parton model (DPM) [101] and Color Glass Condensate model [42, 102] explain the long range forward-backward (F-B) correlations by introducing strong color fields extended longitudinally in rapidity.

The present study is devoted to the forward-backward multiplicity correlations in minimum bias p-p collisions at $\sqrt{s}$ = 0.9, 2.76 and 7 TeV measured with the ALICE at the Large Hadron Collider (LHC). Since this study has been made in p-p collisions, it provides important benchmark for the future analysis in heavy-ion collisions at LHC energies. This work can also highlight the particle production mechanism in p-p collisions comparing the results with different model predictions.

6.2 Definition

Forward-backward correlations have been characterized by the forward-backward correlation strength, $b_{corr.}$, the slope extracted from a linear relationship between the average multiplicity measured in the backward rapidity hemisphere ($< N_b >$) and the multiplicity in the forward rapidity hemisphere, N_f. This relationship was predicted theoretically, seen in hadron-hadron experiments, and expressed as [103, 104],

$$< N_b(N_f) >= a + b_{corr.}N_f \tag{6.1}$$

In this definition, the correlation strength $b_{corr.}$ can be positive or negative with a range of $|b_{corr.}| < 1$. This maximum (minimum) represents total correlation (anti-correlation) of the produced particles separated in rapidity. $b_{corr.} = 0$ is the limiting case of entirely uncorrelated particle production. Experimentally, the slope $b_{corr.}$ in hadron-hadron experiments is found to be positive. The intercept a of equation 6.1 is related to the number of uncorrelated particles.

The correlation strength can be expressed as the ratio of the covariance of the forward-backward multiplicity and the variance of the forward multiplicity. This is done by performing a linear regression of equation 6.1. Thus, equation 6.1 can be expressed in terms of the following calculable average values,

$$b_{\mathrm{corr.}} = \frac{\langle N_f N_b \rangle - \langle N_f \rangle \langle N_b \rangle}{< N_f^2 > - < N_f >^2} = \frac{D_{\mathrm{bf}}^2}{D_{\mathrm{ff}}^2}, \tag{6.2}$$

where D_{ff}^2 and D_{bf}^2 are the forward-forward and backward-forward dispersions.

6.2.1 Analysis method

In a center-of-mass coordinate system, the forward and backward windows have been conventionally defined to be opposite to each other, as shown in the schematic diagram of Fig 6.1. N_f and N_b are the charged particle multiplicities within the forward and backward windows respectively. The width of the each window is denoted as $\delta\eta$. The results have been presented for the different width from 0.2 to 0.8 of the $\delta\eta$. The distance between the two windows is denoted as η *gap*. The F-B correlations are measured symmetrically around $\eta = 0$ with varying the η *gap* values. Thus, depending on the available η windows within -0.8< η <0.8, the values of η *gap* are chosen.

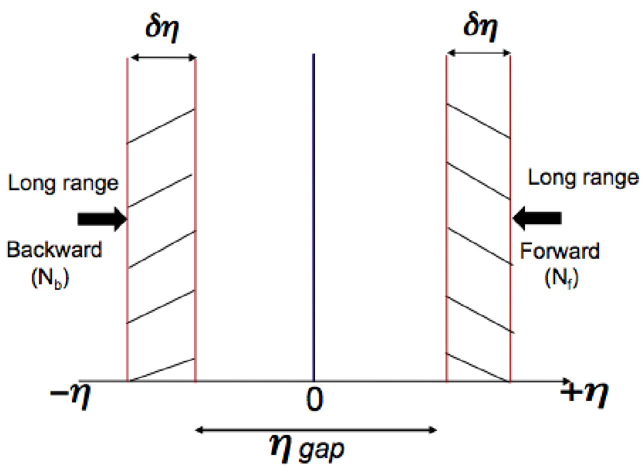

Figure 6.1: Schematic diagram of the measurement of a forward-backward correlation.

6.3 Analysis details

Charged particle multiplicity correlations have been studied using the data measured by the Time Projection Chamber (TPC) and the Inner Tracking System (ITS) within the pseudorapidity coverage of $|\eta| < 0.8$ with full azimuthal (ϕ) acceptance. Minimum bias events have been selected within the z-vertex coverage of ± 10 cm. Charged particles tracks have been selected using the ALICE usual quality conditions. Tracking efficiency correction has been performed using the official production of the PYTHIA and PHOJET event generators. Analysis was done using the standard ALICE Event Summary Data (ESD). The details of the data sets and analysis cuts used in the analysis are listed below:

Data :

0.9 TeV : LHC10c (pass3) : 118506, 118518, 118556, 118558, 118560

2.76 TeV : LHC11a (pass3 With SDD): 146806, 146805, 146804, 146803, 146802, 146801,146858, 146859, 146860

7 TeV : LHC10d (pass2) : 126097, 126090, 126088, 126082, 126081, 126078, 126073, 126008, 126007, 126004

Simulation :

0.9 TeV : LHC10e13 (PYTHIA -Perugia) : 118556, 118558, 118560

2.76 TeV : LHC11e3a (PYTHIA -Perugia) : 146856, 146857, 146858, 146859,146860, 146805

7 TeV : LHC10f6a (PYTHIA -Perugia) : 125850, 125851, 125855, 126004, 126007, 126008, 126078, 126081, 126082

No. of events analyzed :

0.9 TeV : 4M

2.76 TeV : 8M

7 TeV : 5.6M

Event Selection cuts :

Trigger selection: Physics selection

Reconstructed Vertex: yes

Vertex Selection: $|Vz|$ <10 cm

Track selection cuts:

Global tracks are used in this analysis.

Number of TPC clusters (min): 80

χ^2 per number of TPC clusters (max): 4.0

Number of ITS clusters (min): 2

At least one SPD point: kTRUE

DCA(xy) (max): 0.5 cm

DCA(z): 0.5 cm

kITSrefit: kTRUE

kTPCrefit: kTRUE

pT (GeV): 0.3 < pT (GeV/c) <1.5

All the parameters of the event selection and track selection have been varied to calculated systematic uncertainties. Results have been presented changing the different pT intervals.

6.4 Correction procedure

Correlation strength has been measured using the equation 6.2. Each of the quantity of equation 6.2 has been measured in event by event basis to calculate the correlation strength. Tracking efficiency correction has been performed using the MC events passing through the detailed GEANT simulation describing the ALICE detector system. Efficiency is defined as:

$$efficiency = \frac{MC + Geant(Reconstructed)}{MC(Generated)} \tag{6.3}$$

Efficiency of each of the quantity of equation 6.2 has been calculated and each quantity of data is corrected. Taking the corrected values of $< N_f >, < N_b >$ $, < N_f N_b >, < N_f^2 >$ correlation strength "$b_{corr.}$" is calculated. The method are performed for each η *gap*. PYTHIA Perugia - 0 and PHOJET event generator have been used to measure the efficiencies. Fig. 6.2 shows the efficiency values for all the energies.

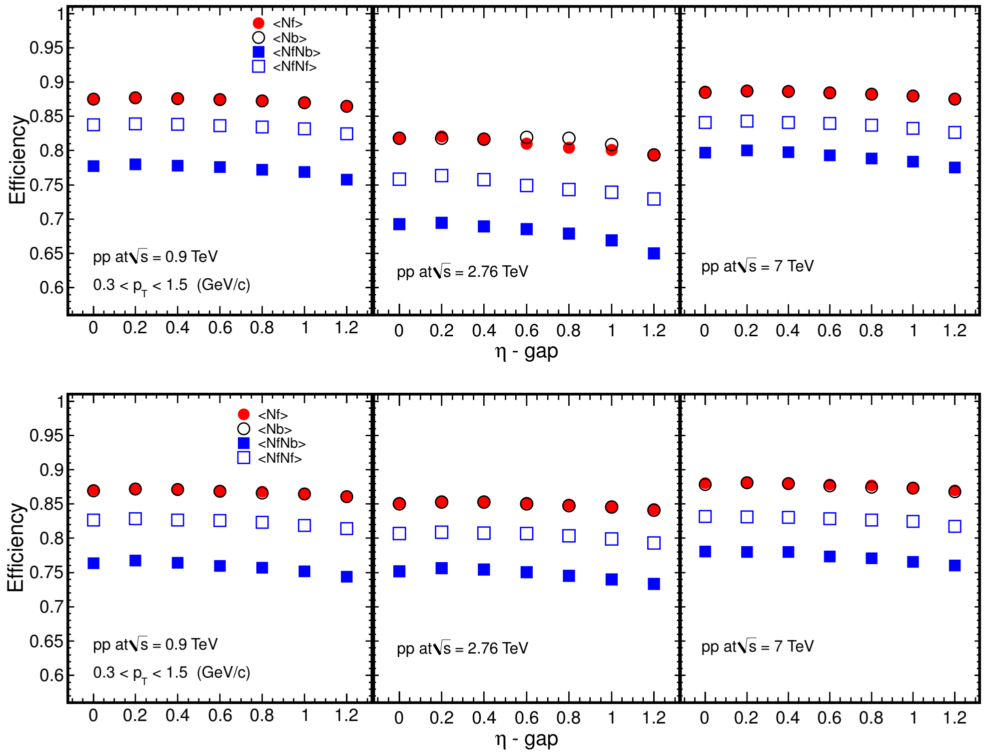

Figure 6.2: Efficiencies of the average multiplicities. Upper plot is from the PYTHIA Perugia - 0 and the lower plot is from the PHOJET event generator.

6.5 Systematic uncertainties

Systematic uncertainties have been calculated by (1) varying the event selection and track selection parameters, (2) taking pile up events, (3) considering different methods of $b_{corr.}$ calculation and efficiency corrections [105].

For each set of selection criteria the multiplicities and the correlation coefficients were determined for every F-B windows pair. Efficiency corrections have been performed in each case and the differences are added in quadrature to get total systematic uncertainties. Statistical uncertainties are small and within the symbol sizes.

Fig. 6.3 correlation strength vs η *gap* for each of the sources. The source of the systematic uncertainties and contribution of the each sources are given in the table 6.1:

Sources	0.9 TeV	2.76 TeV	7 TeV
TPC clusters	0.5 - 3%	0.01 - 0.13%	0.2 - 0.7%
ITS clusters	0.6-1.9%	- -	0.15 - 1.4%
DCA	3 - 4%	0.98 - 1.8%	0.1 - 0.98%
VertexZ	0.2 -1.1%	0.016 - 1%	0.015 - 0.7%
Method	2.5 - 4%	2.2 - 4.2%	1.6 - 2.8%
Pile Up	<1%	<1%	<1%
Total	3.4 - 4.5%	2.8-4.2%	2-3%

Table 6.1: Sources of systematic errors and their contributions.

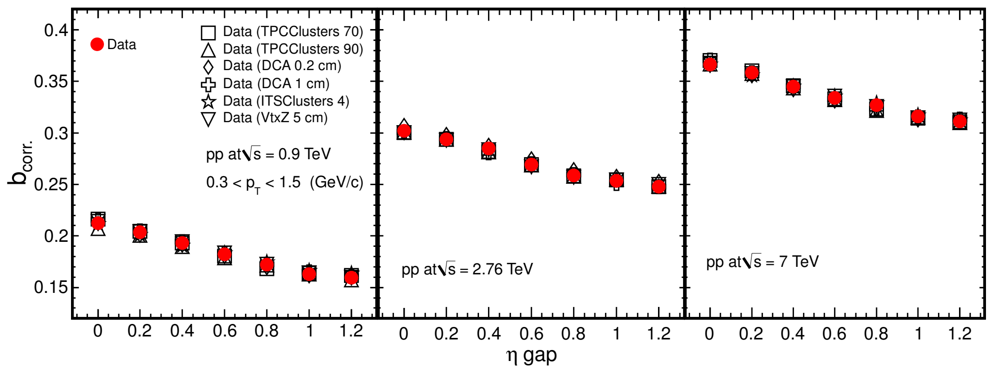

Figure 6.3: Correlation strengths are plotted as a function of η *gap* for different sources of systematic uncertainties. Solid circles are ideal data points and open symbols are for different sources.

6.6 Results and discussions

After the tracking efficiency corrections, the results are presented with the systematic uncertainties and different model predictions.

6.6.1 Correlation strength vs η *gap*

Fig. 6.4 shows the corrected correlation strength, $b_{corr.}$ as a function of η *gap* at $\sqrt{s}$ = 0.9, 2.76 and 7 TeV for 0.2 bin-width of the η windows ($\delta\eta$). It is observed that $b_{corr.}$ decreases slowly with increasing η *gap* and increases with centre of mass energies. The results have been compared with different model predictions such as PYTHIA Perugia - 0, PYTHIA Perugia -11 and PHOJET. It is seen that the expectations from these models show similar trends as data for all the energies. All the model predictions are very close to the data at $\sqrt{s} = 0.9$ TeV, while discrepancies are found at 2.76 TeV and become larger at 7 TeV. It is observed that at these two energies PYTHIA describes the data better than that of PHOJET.

6.6.2 Dispersion

Fig. 6.5 shows the dependence of D^2_{bf} and D^2_{ff} as a function η *gap*. The behavior of D^2_{bf} is similar to FB correlation strength. So correlation strength is dominated by the D^2_{bf} in eq. 6.2.

6.6.3 Bin-width dependence of correlation strength ($b_{corr.}$)

Fig. 6.6 shows the correlation strength as a function of η *gap* for different widths of the pseudorapidity windows ($\delta\eta$). The results have been presented for 0.2, 0.4,

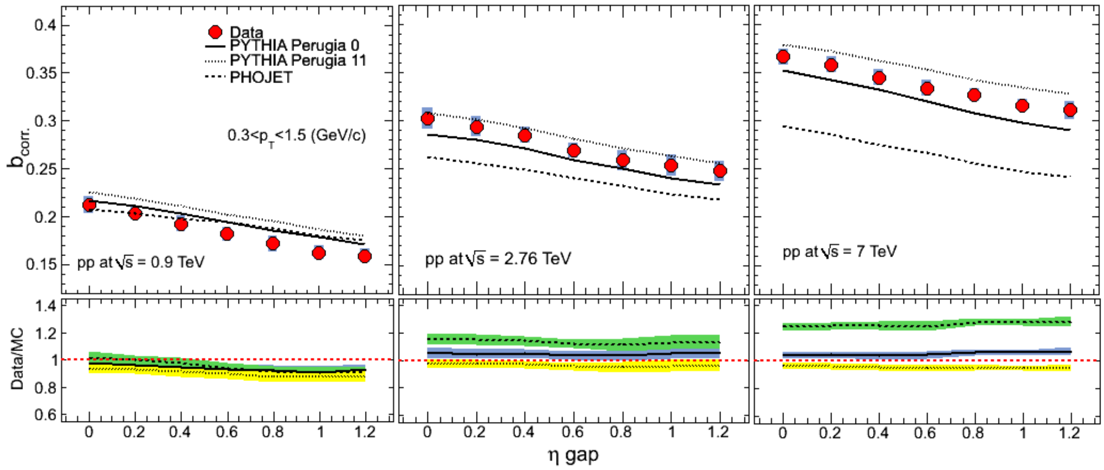

Figure 6.4: $b_{corr.}$ as a function of η *gap*. Solid circles represent the data and shaded regions are for systematic uncertainties. The different lines stand for different model predictions. The lower halves of each panel show the ratio between the data and model prediction. Left: 0.9, middle: 2.76 and right: 7 TeV.

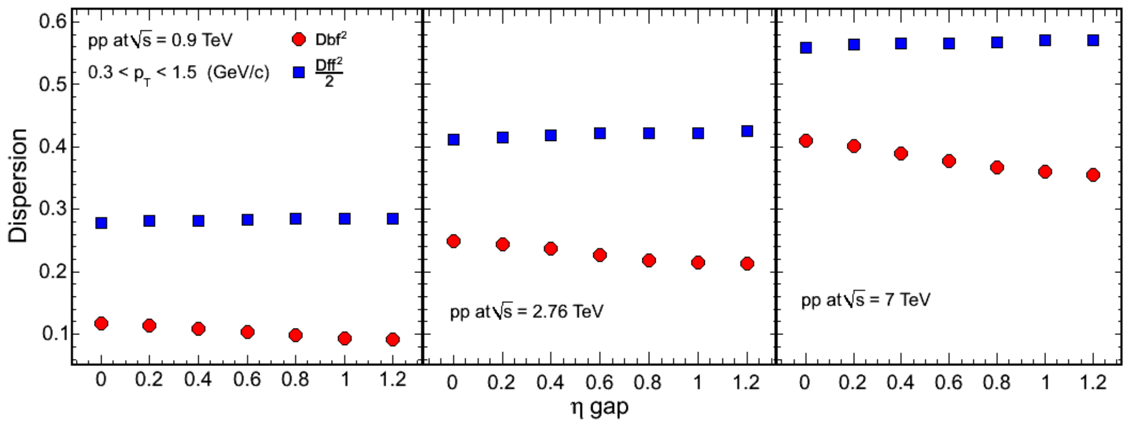

Figure 6.5: dispersions (D^2_{bf} - circles; D^2_{ff} - rectangles) are plotted with η *gap* for $\sqrt{s} = 0.9$, 2.76 and 7 TeV.

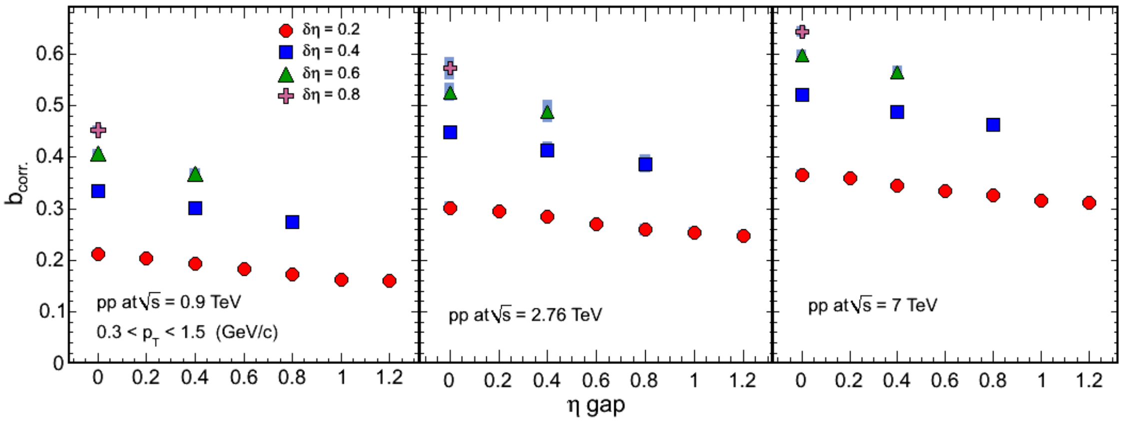

Figure 6.6: $b_{corr.}$ as a function of η *gap* for different $\delta\eta$ at $\sqrt{s} = 0.9$, 2.76 and 7 TeV. Different symbols represent the different widths of the η bins.

0.6 and 0.8 $\delta\eta$. It is found that $b_{corr.}$ increases with increasing $\delta\eta$. $b_{corr.}$ of zero η *gap* have been plotted as a function of $\delta\eta$ in the Fig. 6.7 and a non linear increase of correlation strength with $\delta\eta$ has been observed. A trend of saturation of $b_{corr.}$ with growth of the pseudorapidity windows size has been seen. Different model predictions also show similar behavior as data.

6.6.4 Relative correlation strength

The ratios of the correlation strength of 2.76 and 7 TeV have been presented with respect to 0.9 TeV in the Fig. 6.8 These ratios increase with the increase the η *gap*. The results are compared with the different model predictions and it is found that PYTHIA Perugia - 11 is closer to data while PYTHIA Perugia - 0 and PHOJET values are almost constant and also underestimate the data.

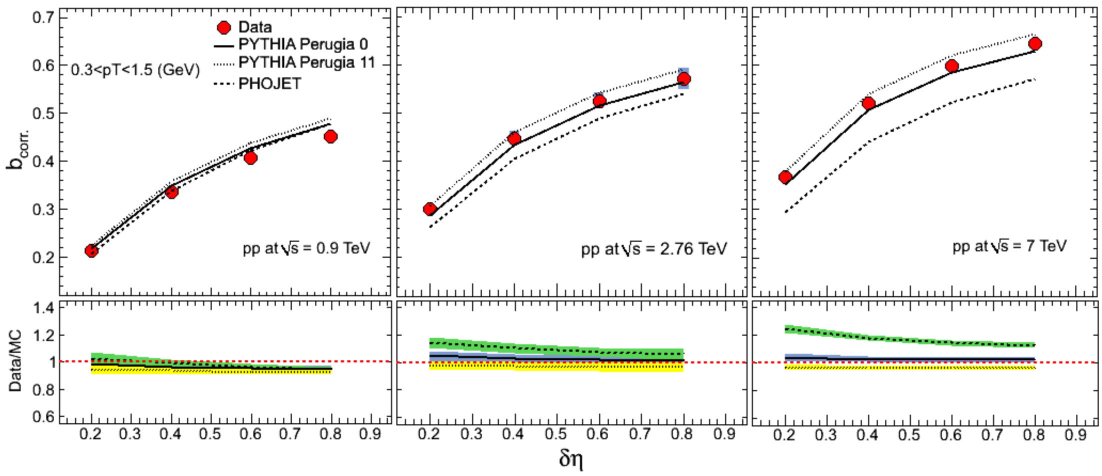

Figure 6.7: $b_{corr.}$ as a function of $\delta\eta$ when $\eta\ gap = 0$. Different lines represent the model predictions from PYTHIA Perugia - 0, PYTHIA Perugia - 11 and PHOJET.

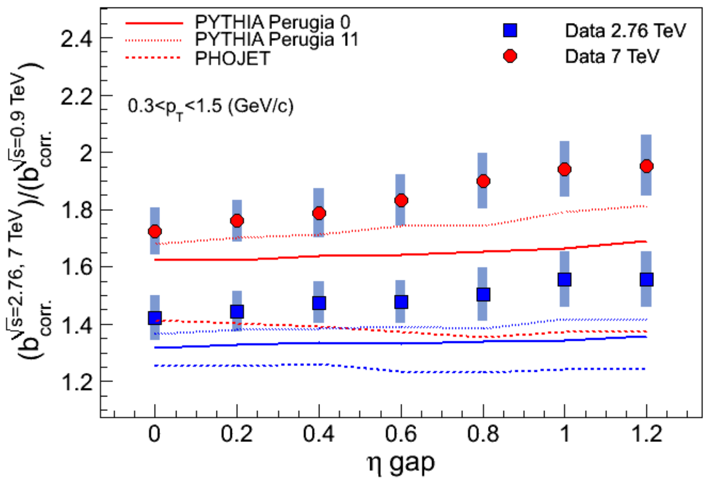

Figure 6.8: Ratio of $b_{corr.}$ of 2.76 and 7 TeV with respect to the $b_{corr.}$ of 0.9 TeV. Shaded regions in data points represent the systematic uncertainties. Different lines represent the model predictions from PYTHIA Perugia - 0, PYTHIA Perugia - 11 and PHOJET.

6.6.5 p_T dependence of multiplicity correlations

Correlation strength $b_{corr.}$ has been studied as a function of minimum p_T cult-off ($p_{T_{min}}$) (Fig. 6.9). The fall of correlation strength has been observed with the growth of the $p_{T_{min}}$ of charged particles. Similar study was made in the ALTLAS experiment [106] and the conclusion was *"This illustrates well the transition between the soft, non-perturbative regime of parton string or cluster fragmentation and the jet-dominated regime of perturbative quantum chromodynamics."*.

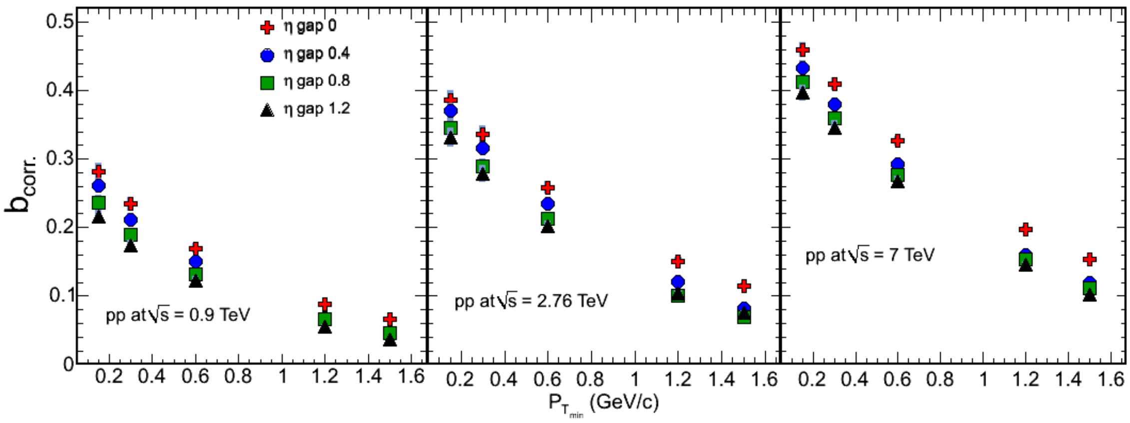

Figure 6.9: $b_{corr.}$ as a function of $p_{T_{min}}$. Different symbols represent the different η *gap* from 0 to 1.2

A different approach has been used to study the p_T dependence of multiplicity correlations. In order to avoid the multiplicity dependence, p_T intervals are chosen such a way that each p_T window has the same average multiplicity ($< n_{ch} >$). In this analysis five p_T intervals are considered within p_T range from 0.3 to 6.0 GeV/c such as: 0.30.396, 0.3960.519, 0.5190.699, 0.6991.031 and 1.0316. The results have been presented for η *gap* $= 0$ and 1.2 at $\sqrt{s} = 7$ TeV in the Fig. 6.10. It is observed that if average mean multiplicity is same for all p_T intervals, the correlation strength increases at p_T intervals with higher p_T.

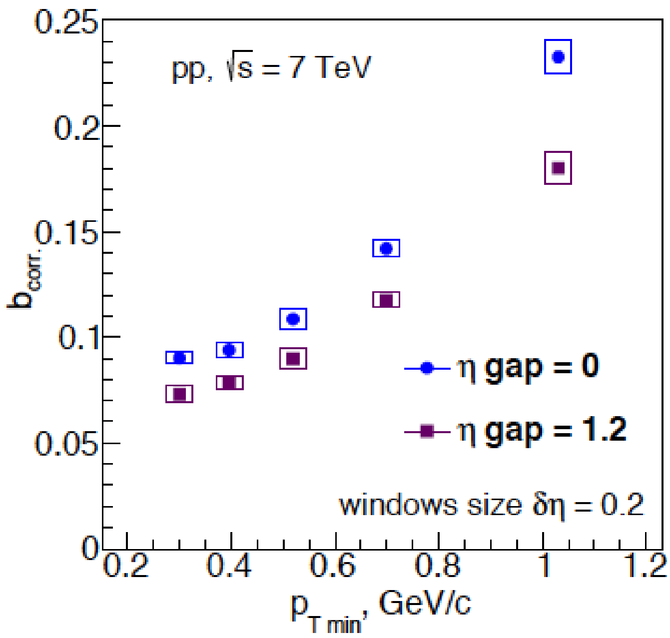

Figure 6.10: $b_{corr.}$ as a function of different p_T intervals having same average multiplicity at $\sqrt{s}$ = 7TeV for two different η *gap*. Systematic uncertainties are shown as rectangles behind the data points.

6.7 Summary

Correlation strength ($b_{corr.}$) between the multiplicity of forward and backward pseudorapidity windows has been measured using the experimental data from the p-p collisions at $\sqrt{s}$ = 0.9, 2.76 and 7 TeV. $b_{corr.}$ has been measured as a function of different η *gap* from 0 to 1.2. The results have been presented for the different width of the pseudorapidity windows ($\delta\eta$). It is found that $b_{corr.}$ decreases with increasing η *gap* for a fixed $\delta\eta$. Non-linear increase of $b_{corr.}$ has been seen with the increase of width of the $\delta\eta$ for the zero η *gap*. A saturation trend of $b_{corr.}$ has been found as a function of $\delta\eta$. A considerable increase of the FB correlation strength with the growth of the collision energy from $\sqrt{s} = 0.9$ to 7 TeV is observed. Correlation strength has been investigated in different transverse momentum ($p_{T_{min}}$) intervals. It is found that $b_{corr.}$ decreases with the increase of the upper limit of the transverse momentum i.e. with increase of $p_{T_{min}}$. It is very similar to the results obtained in the ATLAS experiment [106]. If the p_T intervals is chosen such a way that the average multiplicity remains same, correlation strength is found to increase with the higher p_T window. Results are compared with the expectations from different tunes of PYTHIA and PHOJET event generators. It is observed that both the models are close to data at $\sqrt{s} = 0.9$ TeV and with the increase of beam energy deviations between data and models increase. It is found that PYTHIA describes the data better than that of the PHOJET event generator.

7 Method for the study of forward-backward multiplicity correlations in heavy-ion collisions

In this chapter we will discuss two different methods for the study of forward-backward multiplicity correlations in heavy-ion collisions using the HIJING event generator.

7.1 Introduction

It is a major challenge to experimentally probe the *quark-gluon plasma* state, created very early in the heavy-ion collisions, as majority of the detected particles are emitted at freezeout. Correlations, that are produced across a wide range in rapidity are thought to reflect the earliest stages of the heavy-ion collisions, free from final state effects [42]. The study of correlations among particles produced in different rapidity regions may provide an understanding of the elementary (partonic) interactions which lead to the hadronization.

Recently, F-B correlations have been studied extensively with different model simulations particularly Color Glass Condensate (CGC) [107] and Color String Percolation model (CSPM) [108]. The CGC provides a QCD based description and predicts the growth of LRC with collision centrality [107]. It is argued that long-range rapidity correlations are due to the fluctuations of the number of gluons and can only be created in early times shortly after the collisions [102, 107]. In CGC the long range component has the form:

$$b_{\rm corr} = \frac{1}{1 + c\alpha_s^2}, \tag{7.1}$$

where α_s^2 is coupling constant and is related to the saturation momentum Q_s^2 and c is a constant. From the above expression it is observed that as the centrality increases the F-B correlation also increases because α_s^2 decreases [108]. The similar behavior is also obtained in the CSPM approach. In the CSPM $b_{\rm corr}$ is expressed in terms of the string density ξ which is related to the no of strings formed in the collisions:

$$b_{\rm corr} = \frac{1}{1 + \frac{d}{(1-e^{-\xi})^{3/2}}}, \tag{7.2}$$

which at low string density vanishes, and at high density grows becoming 1/(1+d), d being a constant independent of the density and energy [108]. The experimental data for Au-Au at $\sqrt{s_{NN}}$= 200 GeV [47] shows the similar trend as given by CGC and CSPM.

F-B correlation strength has also been studied in the framework of wounded nucleon model [109, 110]. The results are compared to the STAR data [47] in Au-Au collisions at $\sqrt{s_{NN}}$ = 200 GeV. It has been concluded that F-B correlation strength for central collisions are due to the fluctuations of wounded nucleons at a given centrality bin. Thus it is essential to control the centrality of the collisions while reporting the experimental results on correlations.

In this work two different methods have been studied to extract the correlation strength, b_{corr} and the results from the two method have been discussed.

7.2 Method

In a center-of-mass coordinate system, the forward and backward hemispheres have been conventionally defined to be opposite to each other, as shown in the schematic diagram of Fig. 7.1 N_f and N_b are the charged particle multiplicities in forward and backward pseudorapidity windows. The width of each window is chosen as $\delta\eta = 0.2$. The FB correlation has been measured symmetrically around $\eta = 0$ with varying η *gap* ($\Delta\eta$) measured from the centre of each bin.

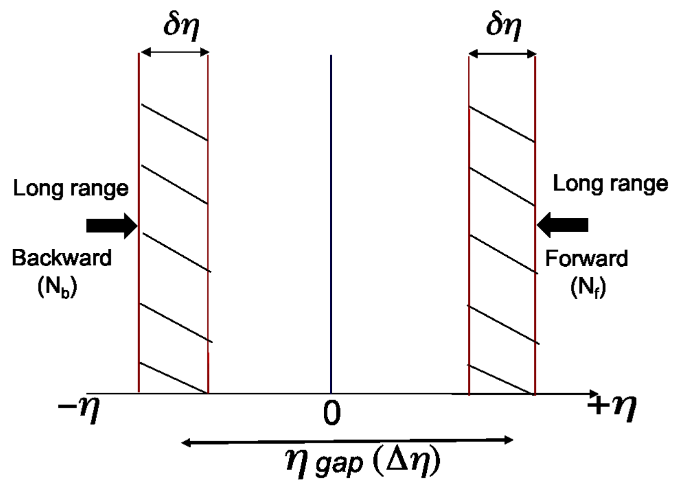

Figure 7.1: Schematic diagram for the measurement of forward-backward correlations.

The data from the HIJING [37] event generator has been used to perform this study at Au-Au 200 GeV and Pb-Pb 2.76 TeV. The centrality of the collision is normally designated in terms of the impact parameter of the collision. In the experiments, it is not possible to determine the impact parameter directly, hence one uses charged particle multiplicity within a range of η, which is not overlapping with the η range where the analysis is performed. This is called reference multiplicity (N_{ref}). Non-overlapping pseudorapidity region has been used to select centrality measurement to avoid the bias in the correlation measurements. In the experiments, it is ideal to obtain reference multiplicity from very forward measurement of charged particles. But if this is not available, then the centrality can be defined from the central windows as well. For example, in the present study, for determining FB correlations in $\Delta\eta = 0.2$, 0.4 and 0.6 reference multiplicity has been obtained within $0.5 < |\eta| < 1.0$, while for $\Delta\eta = 0.8$ and 1.0 the sum of the multiplicities from $\eta < 0.3$ and $0.8 < |\eta| < 1.0$ used for centrality determination. For $\Delta\eta = 1.2$, 1.4, 1.6 and 1.8 the centrality is taken from $|\eta| <0.5$. Within a given centrality window, the FB multiplicity correlations can be affected by the fluctuations in impact parameter and number of participants. In order to extract true correlation, it is desirable to control the centrality and minimize the effect of centrality fluctuations.

To calculate the correlation strength as a function of η *gap* ($\Delta\eta$) for different centrality bins two different method have been discussed. In the first method, the quantities such as, $\langle N_f \rangle$, $\langle N_b \rangle$, $\langle N_f^2 \rangle$ and $\langle N_f N_b \rangle$, can be obtained by averaging over the events within a centrality bin, and thereby calculating the dispersions, D^2_{ff} and D^2_{bf}. This method of event averaging does not take the fluctuation within a centrality window into account. This method is called as $FB_{average}$ method.

In order to eliminate or reduce the effect of the impact parameter (centrality) fluctuations on the measurement the second method has been introduced. In this method the above quantities have been plotted as a function of each of the reference multiplicity, N_{ref}. Linear fits to $\langle N_f \rangle$, $\langle N_b \rangle$ and second order polynomial fits to $\langle N_f^2 \rangle$ and $\langle N_f N_b \rangle$ have been made. These distributions, along with the fits are shown in Fig. 7.2. These fit parameters are used to extract the D^2_{ff} and D^2_{bf}, binned by centrality, and normalized by the total number of events in each bin. This is called as $FB_{profile}$ method. This method removes the dependence of the F-B correlation strength on the width of the centrality bin.

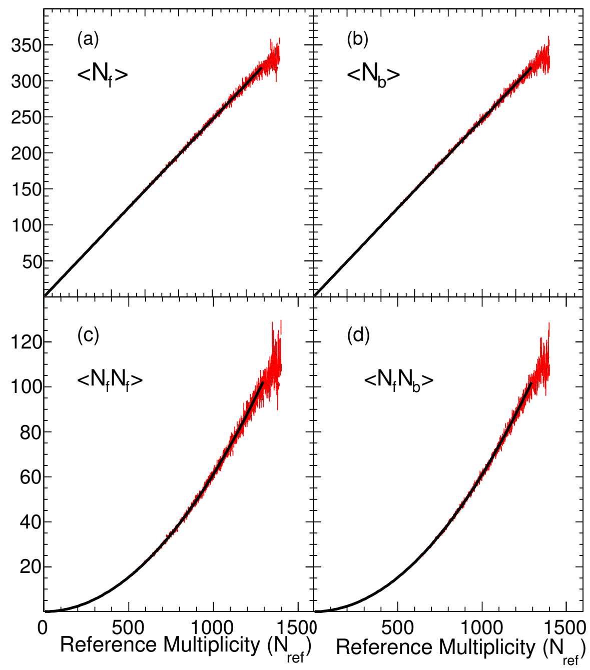

Figure 7.2: Average multiplicities and their products for Pb-Pb collisions at $\sqrt{s_{NN}}$= 2.76 TeV as a function of reference multiplicity (N_{ref}). The upper panels show: (a) mean forward charged particle multiplicity ($\langle N_f \rangle$), (b) mean backward charged multiplicity ($\langle N_b \rangle$), both fitted with linear polynomial functions. The lower panels show (c) $\langle N_f * N_f \rangle$) and (d) $\langle N_f * N_b \rangle$), both fitted with a second order polynomials.

In the next section, results from both the average and profile methods will be presented and compared.

7.3 Results and discussions

The results from the HIJING event generator have been discussed in Pb-Pb collisions at $\sqrt{s_{NN}} = 2.76$ TeV. The forward-forward and backward-forward dispersions are calculated as a function of centrality, within a pseudorapidity gap extending up to 2.2 units, using both average and profile methods. Fig. 7.3 shows D^2_{ff} and D^2_{bf} as a function of $\Delta\eta$ for two overlapping centralities, 0-5% and 0-10% of total cross sections. The dispersions remain approximately constant over the rapidity ranges covered. It is observed that $FB_{average}$ yields higher values of both D^2_{ff} and D^2_{bf} compared to $FB_{profile}$. This is true for both the centrality windows.

It is expected that the correlation strength increases with the increase of the centrality of the collision. The correlation strengths, b_{corr}, are calculated from the ratios of the dispersions for six different centrality windows, 0-2.5%, 0-5%, 0-10%, 10-20%, 20-30%, and 30-40% of the cross section. These centralities are determined from the reference multiplicities as discussed above. Results from both the methods are presented in the top of the Fig. 7.4, where the upper panel shows the values of b_{corr} using $FB_{average}$ method and the lower panel gives the results for $FB_{profile}$ method. We observe that b_{corr} for $FB_{average}$ method does not follow any regular pattern in terms of centrality selection. For example, the b_{corr} is seen to be higher for the 0-10% centrality bin compared to 0-2.5% and 0-5% centrality bin, which is counter intuitive to our expectation. This shows that the impact parameter fluctuations are not completely removed when $FB_{average}$ method is used. On the other hand, it can

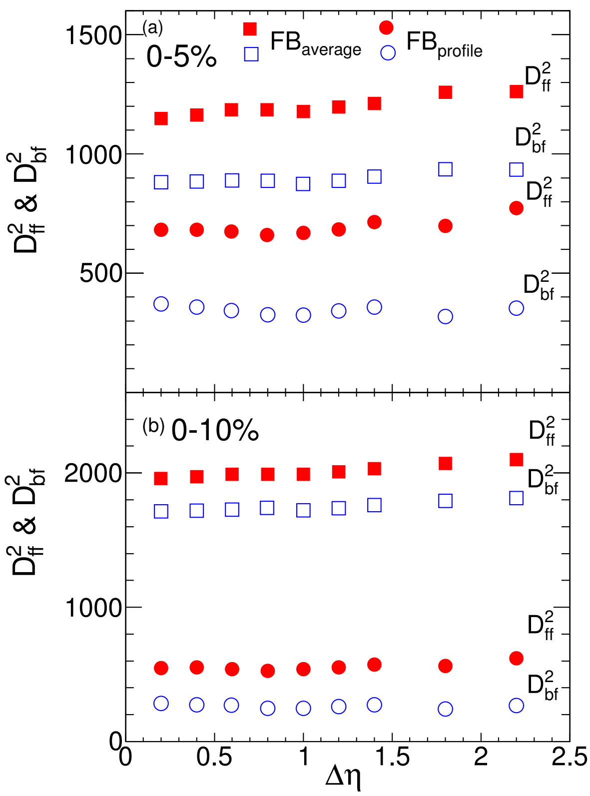

Figure 7.3: Comparison of $D^2_{\rm ff}$ and $D^2_{\rm bf}$ using FB$_{average}$ and FB$_{profile}$ methods. The results are shown for 0-5% and 0-10% centrality for Pb-Pb collisions at $\sqrt{s_{NN}} = 2.76$ TeV. The centrality is selected using charged particle multiplicity from $|\eta| < 0.5$ window. Squares are from $FB_{\rm average}$ method and circles are from $FB_{\rm profile}$ method.

be seen that using the $FB_{profile}$ method, the values of b_{corr}, have an increasing trend with the increase of centrality of the collisions. The correlation strength is highest for 0-2.5% centrality, as expected.

In order to confirm the above observation, a study using the impact parameter window for centrality selection, rather than the reference multiplicity, has been made. Results for b_{corr} for various impact parameter selections are shown in the bottom of the Fig. 7.4 for the average and profile methods, respectively. The average method arrives at improper results. In this example, the larger centrality window yields highest correlation strength, which should not be the case. On the other hand, the $FB_{profile}$ method gives similar results whether centrality selection is made using impact parameter or the reference multiplicity.

A similar study has been made for Au-Au collisions at $\sqrt{s_{NN}} = 200$ GeV using HIJING event generator for top 10% in central collisions. The upper panel of Fig. 7.5 shows D^2_{ff} and D^2_{bf} and the lower panel shows b_{corr}, respectively, for both the average and profile methods. The $FB_{average}$ results yield higher values for b_{corr} compared to $FB_{profile}$. The profile results are similar to what had been reported by the STAR Collaboration at RHIC [47].

Finally, a comparison has been made between the results from Au-Au collisions at $\sqrt{s_{NN}} = 200$ GeV and Pb-Pb collisions at $\sqrt{s_{NN}} = 2.76$ TeV using the results from HIJING event generator, and following the $FB_{profile}$ method. The results are presented for the two centrality windows (0-10% and 30-40%) in Fig. 7.6. It is observed that, for the non-central collisions of 30-40% cross section, the correlation strengths are very similar. For central collisions, a decreasing trend is observed for Au-Au collision at $\sqrt{s_{NN}} = 200$ GeV, whereas for Pb-Pb collisions at $\sqrt{s_{NN}} = 2.76$

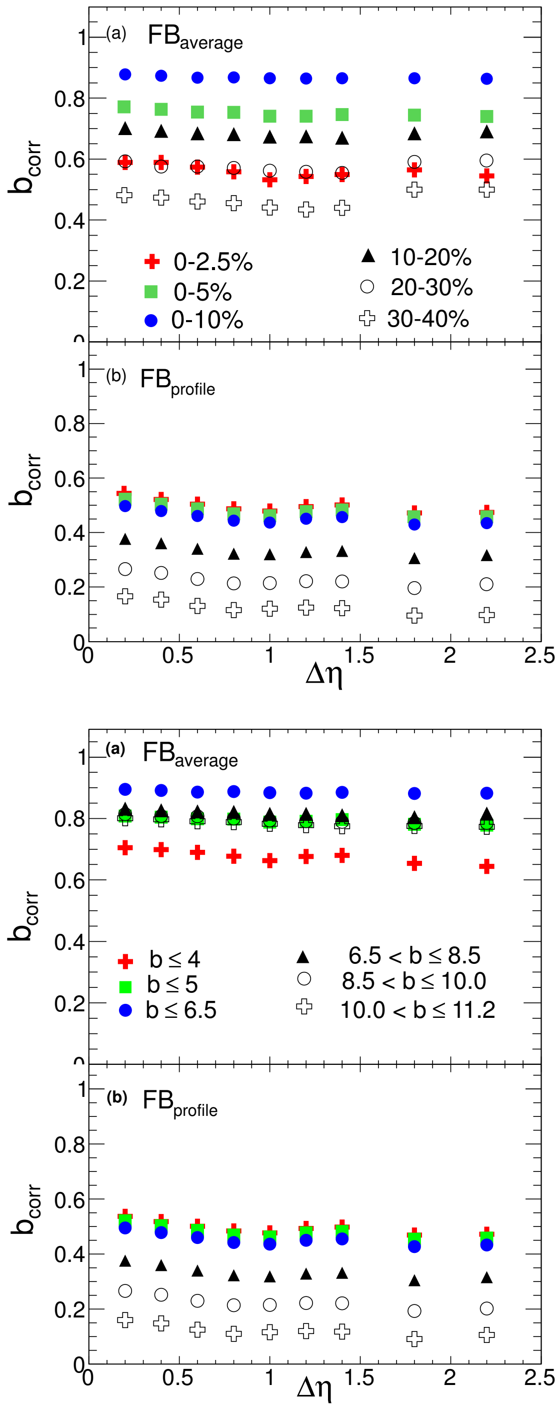

Figure 7.4: Upper: Correlation strength b_{corr} as a function of η *gap* for 6 centrality bins using (a) from FB_{average} and (b) from FB_{profile} for Pb-Pb collisions at $\sqrt{s_{NN}} =$ 2.76 TeV. Lower: Correlation strength b_{corr} as a function of η *gap* for various impact parameters using (a) FB_{average} and (b) FB_{profile} methods for Pb-Pb collisions at $\sqrt{s_{NN}} = 2.76$ TeV.

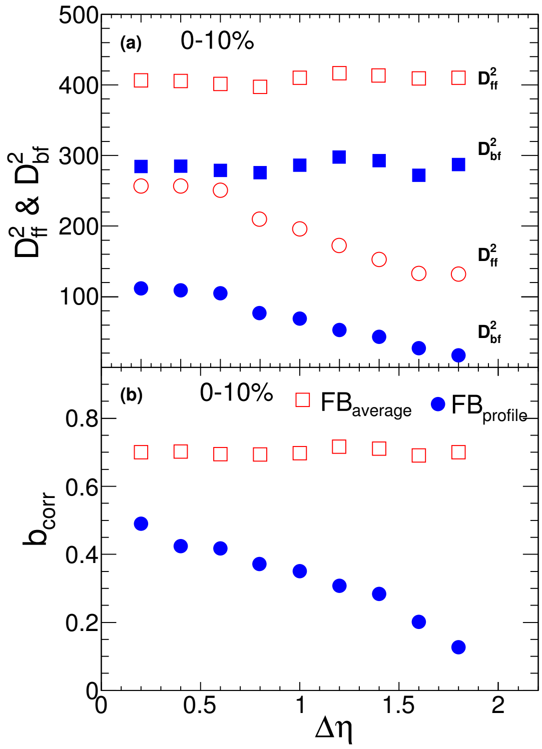

Figure 7.5: (a) $D^2_{\rm ff}$ and $D^2_{\rm bf}$ and (b) correlation strength $b_{\rm corr}$ as a function of η *gap* for 0-10% centrality from $FB_{\rm profile}$ and method $FB_{\rm average}$ for Au-Au collisions at $\sqrt{s_{NN}} = 200$ GeV.

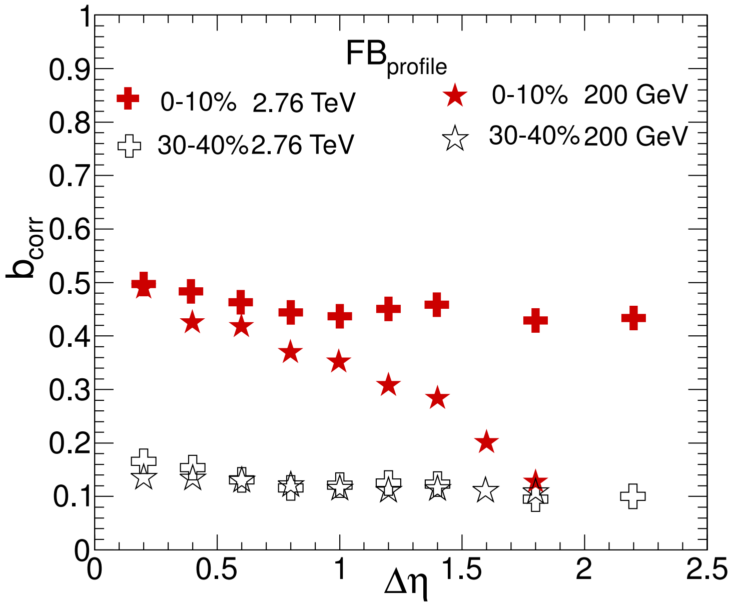

Figure 7.6: Correlation strength as a function of pesudorapidity gaps fo 0-10% and 30-40% centralities in case of Au-Au collisions at $\sqrt{s_{NN}}$ = 200 GeV and Pb-Pb collisions at $\sqrt{s_{NN}}$ = 2.76 TeV. For central collisions, a clear difference in the correlation strength has been observed.

TeV, a flatter distribution is observed. This implies a much stronger correlation over a broad range in pseudorapidity at the LHC energy compared to those at RHIC.

7.4 Summary

In heavy-ion collisions, the correlation strengths are expected to increase with increase of the beam energy as well as centrality of the collision. Within a given centrality window, the fluctuations in the impact parameter or the number of participants lead to multiplicity fluctuations which affect the accurate determination of correlation strength. It is therefore needed to control the centrality of the collisions while performing the correlation analysis. In this work, two different methods, the average method and the profile method, have been presented to study the forward-backward multiplicity correlations in heavy-ion collisions as a function centrality. It is observed that in the $FB_{average}$ method, the correlation strength does not follow any pattern as a function of centrality window. This reflects the impact parameter fluctuation due to finite centrality bin width. The second method, $FB_{profile}$, has been introduced, which properly takes care of the effects due to finite centrality bin width. Appropriate centrality dependence has been observed in going from peripheral to central method. A comparison of the correlation strengths have been made for Au-Au collision at $\sqrt{s_{NN}} = 200$ GeV and Pb-Pb collisions at $\sqrt{s_{NN}} = 2.76$ TeV using the data from HIJING event generator. It has been observed that the correlation strengths are higher for higher energy collision. The correlation strengths decrease as a function of the rapidity gap. This decrease is much slower at LHC energy compared to that of the RHIC energies. The $FB_{profile}$ method can be used to study the F-B correlation strength as a function of centrality in the Pb-Pb collisions at LHC. It is also important from the models (CGC and CSPM) point of view to know the nature of the F-B correlations.

8 Summary and outlook

In this thesis an attempt has been made to measure the multiplicity and pseudoraidity distributions of the inclusive photons and to study the forward-backward (F-B) multiplicity correlations of charged particles in ALICE experiment. Photon production has been studied in p-p and p-Pb collisions using the data from the Photon Multiplicity Detector (PMD) and the data from the ALICE central barrel (Time Projection Chamber (TPC) and Inner Tracking System (ITS)) has been used to study the F-B correlations in p-p collisions.

The first part of the thesis includes the detailed description of PMD, the testing of the PMD modules and extracting the photon signals using the experimental data and simulation. It has been discussed that PMD consists of two identical plane (preshower and CPV) and a Pb converter between them. Each of the planes consists of 20 identical modules containing 4608 honeycomb cells per module. Test of the PMD modules has been performed in the CERN-PS area using the pion and electron beams. The different responses of the pions and electrons to the preshower plane have been observed. It has been seen that the pions affect only one or two cells and deposit very less energy whereas, electrons produce shower while passing through the Pb converter and affect larger number of cells as well as deposit large amount of energy. These two different responses help to exclude most of the charge particles from the photon sample in the experiment. The operating voltage has been optimized as -1300V and the proportion of Ar and CO_2 in the gas mixture has been been chosen as 70 : 30. Conversion of keV to ADC has been obtained in the test beam experiment which is very important to make simulated data similar to experimental data.

A detailed simulation work has been performed to understand the effect of the upstream material in front of the PMD. It has been found that within the PMD coverage ($2.3 < \eta < 3.9$) the contribution of material (in terms of radiation length) due to the other detectors is very less. Deflection of the original photon tracks due to upstream material has been studied and it is found that deflection could be minimized after applying the photon-hadron discrimination thresholds. Systematic uncertainties have been calculated using the PHOJET with normal AliRoot material and with an increase of 10% material budget. It is found that the uncertainties due to the material are 3-5% in multiplicity (up to 1-10 multiplicity) and 7% in pseudorapidity distribution respectively.

Detailed analysis procedure has been discussed in p-p collisions at $\sqrt{s} = 2.76$ and 7 TeV. Unfolding method has been used to correct the raw data. Multiplicity distribution and pseudorapidity density of incident photons have been presented with expectation from different event generators like PYTHA Perugia 0 and PHOJET. It is found that both the models underpredict the data at both energies. Photon multiplicity distributions have been fitted with a single NBD function as well as a double NBD functions. It is observed that double NBD function describes the data better than that of single NBD. The beam energy dependence of average photon multiplicity within $2.3 < \eta < 3.9$ has been presented. Low energy (0.2 to 0.9 TeV) data points have been taken from the UA5 experiment. It is found that the average photon multiplicity increases with beam energy as $\ln\sqrt{s}$ as well as a power law. Limiting fragmentation behavior has been studied at $\sqrt{s}$ = 0.9, 2.76 and 7 TeV. It is difficult to make any conclusion regarding the longitudinal scaling within this limited acceptance of η. Since neither PYTHIA Perugia 0 nor PHOJET could explain the data in forward rapidity region at $\sqrt{s}$ = 2.76 and 7 TeV, it would be interesting to introduce other models to understand the underlying physics.

Preliminary result of pseudorapidity density of inclusive photons has been presented in p-Pb collisions at $\sqrt{s}$ = 5.02 TeV using the PMD. A detailed simulation work has been performed to calculate the detector efficiency and purity for each η bin. Using these correction factors incident photons have been measured in the experiment. The results have been presented for minimum-bias as well as different centrality classes in p-Pb collisions with the expectation from the DPMJET event generator. It is found that DPMJET is close to data for MB events, but it underestimates the data at all centrality classes. Systematic uncertainties to be calculated in this work.

The second part of the thesis includes the study of the forward-backward multiplicity correlations in p-p collisions at $\sqrt{s}$ = 0.9, 2.76 and 7 TeV and method for the study in heavy-ion collisions. To do the efficiency correction a detailed simulation study has been performed with the event generators PYTHIA Perugia - 0 and PHOJET. The results have been presented as a function of η *gap* between the two windows as well as with the different bin widths ($\delta\eta$). It is found that correlation strength decreases with increasing the η *gap* at all the energies and strongly increases with beam energy. Different model predictions such as: PYTHIA Perugia - 0, PYTHIA Perugia - 11 and PHOJET are presented with data. It has been found that all the models describe the data very well at $\sqrt{s} = 0.9$ TeV. Discrepancies between data and models have been found at 2.76 TeV and its become larger at 7 TeV. This may put a constrain to the existing models. Correlation strength increases with the width of the η windows at η $gap = 0$ and a saturation trend is observed. Relative correlation strength has been studied with respect to the 0.9 TeV and it is observed the the correlation strength of 7 TeV and 2.76 TeV increases with respect to 0.9 TeV as a function of η *gap*. It is found that only PYTHIA Perugia - 11 is closer to data. Transverse momentum (p_T) dependence of the correlation strength has been studied with two different approaches. It is observed that correlation strength has been decreases with increasing the minimum cut off the p_T. But if the p_T intervals are chosen such a way that the mean multiplicity is same for every bins, $b_{corr.}$ increases with increasing η *gap*.

Method for the analysis of F-B correlations in heavy-ion collisions has been discussed in the thesis. The simulated data from HIJING event generator has been analyzed. The results have been presented for Pb-Pb at $\sqrt{s_{NN}} = 2.76$ TeV and Au-Au at $\sqrt{s_{NN}} = 0.2$ TeV. Results have been presented for different centrality classes as well as for different impact parameter values. In this work two different methods have been performed to extract the correlation strength as a function of η *gap* for different centrality classes. In $FB_{average}$ method correlation strength is calculated by averaging over the events within a centrality bin. This method of event averaging does not take care of the fluctuation within a centrality window. To take care of these effects, another method is introduced, which is called $FB_{profile}$ method. It has been found that according to $FB_{average}$ the correlation strength does not follow any pattern as a function of centrality window while $FB_{profile}$ method provides a nice centrality dependence of the correlation strength. It has been prescribed that $FB_{profile}$ method should be used to analyze the experimental data in Pb-Pb collisions at LHC energies.

Bibliography

[1] T. S. Pettersson (ed.), P. Lef'evre (ed.), The Large Hadron Collider : conceptual design, CERN-AC-95-05 LHC (1995).

[2] LHC Design Report Volume I+II+III, CERN-2004-003-V-1, CERN-2004-003-V- 2, CERN-2004-003-V-3 (2004), http://ab-div.web.cern.ch/ab-div/Publications/LHC-DesignReport.html.

[3] Peter W. Higgs, Phys. Rev. Lett. Vol 13, 1964

[4] Steven Weinberg, The First Three Minutes: A Modern View of the Origin of the Universe, Basic Books, 1977, [ISBN: 0-465-02437-8].

[5] E. W. Kolb and M. S. Turner, The Early Universe, Westview Press, 1990

[6] E. V. Shuryak, Phys. Rep. 61, 71 (1980).

[7] D. J. Gross, F. Wilczek, Phys. Rev. Lett. 30, 1343 (1973).

[8] H. Politzer Phys. Rev. Lett. 30, 1346 (1973).

[9] Cabibbo N. and Parisi G. 1975 Phys.Lett. B 5967.

[10] M. Stephanov, Phys. Rev. Lett. 76 (1996) 4472.

[11] J. D. Bjorken, Phys. Rev. D27, 140 (1983).

[12] ALICE Collaboration, PRL 110, 082302 (2013)

[13] ATLAS Collaboration,PRL 105, 252303 (2010)

[14] ALICE Collaboration, PRL 109, 072301 (2012) PHENIX Collaboration, PRL 98, 232301 (2007)

[15] P. Koch, B. Mu ller, and J. Rafelski, Phys. Rep. 142, 167 (1986).

[16] STAR Collaboration, Nucl. Phys. A 757, 102 (2005); PRL 108, 072301 (2012); PHENIX Collaboration, Nucl. Phys. A 757, 184 (2005);

[17] ALICE Collaboration, arXiv:1208.4968

[18] J. F. Grosse-Oetringhaus, PhD thesis, University of Munster, Germany, 2009.

[19] R. P. Feynman, Phys. Rev. Lett. 23 (1969) 1415.

[20] Z. Koba, H. B. Nielsen and P. Olesen, Nucl. Phys. B 40 (1972) 317.

[21] UA5 Collaboration, Phys. Lett. B 160 (1985) 193.

[22] UA5 Collaboration, Z. Phys. C 32 (1986) 153.

[23] A. Giovannini and R. Ugoccioni, Phys. Rev. D 59 (1999) 094020 [Erratum-ibid. D 69 (2004) 059903].

[24] ALICE collaboration, Eur. Phys. J. C (2010) 68: 345354

[25] ALICE collaboration, Eur. Phys. J. C (2010) 68: 89108

[26] J BENKCKEs et. al., Phys. Rev. Vol 188, 1969.

[27] A.K.Dash, PhD thesis, http://www.hbni.ac.in/phdthesis/11phdthesis.htm

[28] STAR collaboration, Phys. Rev. C 73, 034906 (2006)

[29] Francois Gelis et. al., Eur.Phys.J.C 48:489-500,2006

[30] PYTHIA 6.4, Physics and Manual, hep-ph/0603175, FERMILAB-PUB-06-052-CD-T, March 2006.

[31] T. Sjostrand, Comput. Phys. Commun. 82, 74 (1994)

[32] T. Sjostrand, S. Mrenna, P. Skands, J. High Energy Phys. 2006, 05 026 (2006)

[33] R. Engel, Z. Phys. C 66, 203 (1995)

[34] R. Engel, J. Ranft, S. Roesler, Phys. Rev. D 52, 1459 (1995)

[35] A. Capella et al., Phys. Rep. 236, 225 (1994)

[36] K. Hahn, J. Ranft, Phys. Rev. D 41, 1463 (1990).

[37] M. Gyulassy, X. -N. Wang, Phys. Rev. C80, 024906 (2009).

[38] J. Ranft: New features in DPMJET version II.5, Siegen preprint, 1999

[39] J. Ranft, DPMJET version II.5, arXiv:hep-ph/9911232v1

[40] Stefan Roesler et. al., arXiv:hep-ph/0012252v1

[41] B. Zhang, C. M. Ko, B. A. Li, and Z. Lin, Phys. Rev. C 61, 067901 (2000).

[42] Y.V. Kovchegov, E. Levin, and L. McLerran, Phys. Rev. C 63, 024903 (2001).

[43] T. Alexopoulos et al. Phys. Lett. B 353:155, (1995).

[44] S. UHLIG et. al. Nucl. Phys. B 132 (1978) 15-28

[45] UA5 Collaboration. Z. Phys., C 37:191, (1988).

[46] E735 Collaboration, Phys. Lett. B, 353 (1995) 155-160.

[47] STAR Collaboration, Phys. Rev. Lett., 103 (2009) 172301.

[48] ALICE Collaboration, ALICE Technical Proposal for A Large Ion Collider Experiment at the CERN LHC, CERN/LHCC 95-71 (1995).

[49] The ALICE experiment at the CERN LHC, 2008 JINST 3 S08002.

[50] ATLAS Collaboration, ATLAS Technical Proposal, CERN/LHCC 94-43 (1994).

[51] CMS Collaboration, The Compact Muon Solenoid Technical Proposal, CERN/LHCC 94-38 (1994).

[52] LHCb Collaboration, LHCb Technical Proposal, CERN/LHCC 98-4 (1998).

[53] LHCf Collaboration, Technical Proposal for the CERN LHCf Experiment, CERN/LHCC 2005-032 (2005).

[54] TOTEM Collaboration, TOTEM Technical Proposal, CERN/LHCC 99-7 (1999).

[55] ALICE Collaboration, ALICE dimuon forward spectrometer: Technical Design Report, CERN-LHCC-99-022; http://cdsweb.cern.ch/record/401974; ALICE dimuon forward spectrometer: addendum to the Technical Design Report, CERN-LHCC-2000-046, http://cdsweb.cern.ch/record/494265.

[56] ALICE Collaboration, ALICE Inner Tracking System (ITS): Technical Design Report, CERN-LHCC-99-012, http://edms.cern.ch/file/398932/1.

[57] ALICE Collaboration, ALICE time projection chamber: Technical Design Report, CERN-LHCC-2000-001, http://cdsweb.cern.ch/record/451098.

[58] ALICE Collaboration, ALICE transition-radiation detector: Technical Design Report, CERN-LHCC-2001-021, http://cdsweb.cern.ch/record/519145.

[59] ALICE Collaboration, ALICE Time-Of-Flight system (TOF): Technical Design Report, CERN-LHCC-2000-012; http://cdsweb.cern.ch/record/430132; ALICE Time-Of Flight system (TOF): addendum to the technical design report, CERN-LHCC-2002-016, http://cdsweb.cern.ch/record/545834.

[60] ALICE Collaboration, Technical design report of the photon spectrometer, CERN-LHCC-99-004, http://cdsweb.cern.ch/record/381432.

[61] ALICE Collaboration, ALICE electromagnetic calorimeter: addendum to the ALICE technical proposal, CERN-LHCC-2006-014, http://cdsweb.cern.ch/record/932676.

[62] ALICE Collaboration, ALICE high-momentum particle identification: Technical Design Report, CERN-LHCC-98-019, http://cdsweb.cern.ch/record/381431.

[63] A. Fernndez et al., Cosmic ray physics with the ALICE detectors, Czech. J. Phys. 55 (2005) B801; A. Fernndez et al., ACORDE a cosmic ray detector for ALICE, Nucl. Instrum. Meth. A 572 (2007) 102.

[64] ALICE Collaboration, ALICE Photon Multiplicity Detector (PMD): Technical Design Report, CERN-LHCC-99-032; http://cdsweb.cern.ch/record/451099; ALICE Photon Multiplicity Detector (PMD): addendum to the technical design report, CERN-LHCC-2003-038, http://cdsweb.cern.ch/record/642177.

[65] ALICE Collaboration, ALICE forward detectors: FMD, TO and VO: Technical Design Report, CERN-LHCC-2004-025, http://cdsweb.cern.ch/record/781854.

[66] ALICE Collaboration, ALICE Zero-Degree Calorimeter (ZDC): Technical Design Report, CERN-LHCC-99-005, http://cdsweb.cern.ch/record/381433.

[67] ALICE Collaboration, ALICE Technical Design Report of the Trigger, Data Acquisition, High-Level Trigger, Control System, CERN/LHCC 2003/062 (2004), https://edms.cern.ch/document/456354/2.

[68] P. Saiz et al., AliEn ALICE environment on the GRID, Nucl. Instrum. Meth. A 502 (2003) 437; AliEn home page, http://alien.cern.ch/.

[69] The ALICE experiment offline project, http://www.cern.ch/ALICE/Projects/offline/aliroot/Welcome.html.

[70] An object-oriented data analysis framework, http://root.cern.ch.

[71] R. Brun, R. Hagelberg, M. Hansroul and J. C. Lassalle, Geant: Simulation Program for Particle Physics Experiments. User Guide and Reference Manual, CERN-DD-78-2-REV (1978).

[72] S. Agostinelli et al. [GEANT4 Collaboration], GEANT4: a Simulation Toolkit, Nucl. Instrum. Meth. A 506 (2003) 250.

[73] A. Fasso et al., The physics models of FLUKA: Status and recent development, Conference Proceedings of Computing in High-Energy and Nuclear Physics (CHEP 03), La Jolla, California, arXiv:hep-ph/0306267 (2003).

[74] A.K. Dash, Institute of Physics Bhubaneswar Internal Report IP/BBSR/2009-7

[75] S.Jena, S.De, R.Singha, A. Nyatha, G. KM, https://aliceinfo.cern.ch/Notes/node/22

[76] S.K. Prasad PhD thesis, Calcutta University, 2010

[77] M.M.Mondal PhD thesis, Calcutta University, 2010

[78] ALICE Collaboration, Eur. Phys. J. C65, 111 (2010)

[79] STAR Collaboration, Phys. Rev. Lett. 95, 062301 (2005)

[80] P. K. Netrakanti, Ph.D. Thesis, Jadhavpur University 2008; D. Das, Ph.D. Thesis, Jadhavpur University 2008; M. Sharma, Ph.D. Thesis, Panjab University 2008; N. Gupta, Ph.D. Thesis, Jammu University 2008; S. M. Dogra, Ph.D. Thesis, Jammu University 2009; http://drupal.star.bnl.gov/STAR/thesis

[81] S. C. Phatak Clustering Algorithm For PMD Data http://www.iopb.res.in/phatak/cluster/clusters.html.

[82] Volker Blobel, arXiv:hep-ex/0208022v1 (2002).

[83] Volker Blobel, Unfolding for HEP experiments - Introduction to inverse problems DESY Computing Seminar 23.rd June 2008 http://www.desy.de/ blobel/itunfold.pdf.

[84] M.G. Albrow et al. (Tev4LHC QCD Working Group), arXiv:hep-ph/0610012 (2006), D6T (109) tune

[85] P.Z. Skands, Multi-Parton Interaction Workshop, Perugia, Italy, 28-31 Oct. 2008, arXiv:0905.3418[hep-ph] (2009), Perugia-0 (320) tune

[86] Z. Phys. C - Particles and Fields 43, 75-89 (1989)

[87] https://aliceinfo.cern.ch/Notes/node/149

[88] L. P. Csernai, J. Kapusta, and L. D. McLerran, Phys. Rev. Lett. 97 (2006) 152303

[89] PHOBOS Collaboration, Phys. Rev. Lett. 93 (2004) 082301

[90] ALICE Collaboration, Phys. Rev. Lett. 110 082302 (2013)

[91] https://twiki.cern.ch/twiki/bin/viewauth/ALICE/PACentStudies

[92] W. Braunschweig et al. (TASSO Collaboration). Z. Phys., C45:193, (1989).

[93] P. Abreu et al. (DELPHI Collaboration). Z. Phys., C50:185, (1991).

[94] R. Akers. Phys. Lett., B320:417, (1994).

[95] C.M. Bromberg et al. Phys. Rev., D9:1864, (1974).

[96] S. Uhlig et al. Nucl. Phys., B132:15, (1978).

[97] R.E. Ansorge et al. (UA5 Collaboration). Z. Phys., C37:191, (1988).

[98] M. Arneodo et al. (European Muon Collaboration). Nucl. Phys., B258:249, (1985).

[99] V.V. Aivazyan et al. (NA22 Collaboration). Z. Phys., C42:533, (1989).

[100] A. Capella and A. Krzywicki, Phys. Rev. D 18, 4120 (1978).

[101] A. Capella et al., Phys. Rep. 236, 225 (1994).

[102] N. Armesto, L. McLerran, and C. Pajares, Nucl. Phys. A 781, 201 (2007).

[103] A. Capella and J. Tran Thanh van. *Phys. Rev.*, D29:2512, (1984).

[104] G.J. Alner et al. *Phys. Rept.*, 154:247, (1987).

[105] https://aliceinfo.cern.ch/Notes/node/164

[106] G. Aad et al. (The ATLAS Collaboration), JHEP 511 07 (2012) 019 [arXiv:1203.3100]

[107] T. Lappi, L. McLerran, Nucl. Phys. A**832** (2010) 330.

[108] C. Pajares, Nucl. Phys. B**854** (2011) 125.

[109] A. Bzdak, Phys. Rev. C80 024906 (2009).

[110] A. Bialas, M. Bleszynski, W. Czyz, Nucl. Phys. B**111** (1976) 461.

List Of Publications

1. **Inclusive photon production at forward rapidities for proton-proton collisions at $\sqrt{s} = 0.9$, 2.76 and 7 TeV.**

   Sudipan De, S. Singha, S. Jena, S. K. Prasad, T. K. Nayak (ALICE Collaboration)

   Target journal: EPJC (Collaboration Review)

2. **Forward-backward multiplicity correlations in pp collisions at $\sqrt{s} =$ 0.9, 2.76 and 7 TeV.**

   I. Altsybeev, Sudipan De, G. Feofilov, V. Kovalenko, B. K. Srivastava, V. Vechernin (ALICE Collaboration)

   Target journal: JHEP (Collaboration Review)

3. **Method for the analysis of forward-backward multiplicity correlations in heavy-ion collisions.**

   Sudipan De, T. Tarnowsky, Tapan K. Nayak, B. K. Shrivastva

   Phys. Rev. C 88.044903 (2013)

4. **Baseline study for higher moments of net-charge distributions at energies available at the BNL Relativistic Heavy Ion Collider.**

   Nihar R. Sahoo, Sudipan De, Tapan K. Nayak

   Phys. Rev. C 87.044906 (2013)

5. **Charged-Particle Multiplicity Density at Midrapidity in Central Pb-Pb Collisions at $\sqrt{s_{NN}} = 2.76$ TeV**

   Phys. Rev. Lett. 105, 252301 (2010) (ALICE Collaboration)

6. **Elliptic Flow of Charged Particles in Pb-Pb Collisions at $\sqrt{s_{NN}} = 2.76$ TeV**

   Phys. Rev. Lett. 105, 252302 (2010) (ALICE Collaboration)

7. **Centrality Dependence of the Charged-Particle Multiplicity Density at Midrapidity in Pb-Pb Collisions at $\sqrt{s_{NN}} = 2.76$ TeV**

   Phys. Rev. Lett. 106, 032301 (2011) (ALICE Collaboration)

8. **Suppression of charged particle production at large transverse momentum in central PbPb collisions at $\sqrt{s_{NN}} = 2.76$ TeV**

   Phys. Lett. B 696 (2011) 30-39 (ALICE Collaboration)

9. **Two-pion Bose-Einstein correlations in central Pb-Pb collisions at $\sqrt{s_{NN}} = 2.76$ TeV**

   Phys. Lett. B 696 (4): 328-337 (2011) (ALICE Collaboration)

10. **Higher Harmonic Anisotropic Flow Measurements of Charged Particles in Pb-Pb Collisions at $\sqrt{s_{NN}} = 2.76$ TeV**

    Phys. Rev. Lett. 107, 032301 (2011) (ALICE Collaboration)

11. **Strange particle production in proton-proton collisions at $\sqrt{s} = 0.9$ TeV with ALICE at the LHC**

    Eur. Phys. J. C 71 (3), 1594 (2011) (ALICE Collaboration)

12. **Femtoscopy of pp collisions at $\sqrt{s} = 0.9$ and 7 TeV at the LHC with two-pion Bose-Einstein correlations**

    Phys. Rev. D 84, 112004 (2011) (ALICE Collaboration)

13. **Measurement of charm production at central rapidity in proton-proton collisions at $\sqrt{s} = 7$ TeV**

    JHEP 01 (2012) 128 (ALICE Collaboration)

14. **J/ψ Polarization in pp Collisions at $\sqrt{s} = 7$ TeV**

    Phys. Rev. Lett. 108 (2012) 082001 (ALICE Collaboration)

15. **Harmonic decomposition of two particle angular correlations in Pb-Pb collisions at $\sqrt{s_{NN}} = 2.76$ TeV**

    Phys. Lett. B 708 (2012) 249-264 (ALICE Collaboration)

16. **Heavy flavour decay muon production at forward rapidity in protonproton collisions at $\sqrt{s} = 7$ TeV**

    Phys. Lett. B 708, (2012) 265 - 275 (ALICE Collaboration)

17. **Particle-Yield Modification in Jetlike Azimuthal Dihadron Correlations in Pb-Pb Collisions at $\sqrt{s_{NN}} = 2.76$ TeV**

    Phys. Rev. Lett. 108, 092301 (2012) (ALICE Collaboration)

18. **Measurement of event background fluctuations for charged particle jet reconstruction in Pb-Pb collisions at $\sqrt{s_{NN}} = 2.76$ TeV**

    JHEP 03 (2012) 053 (ALICE Collaboration)

19. **Light vector meson production in pp collisions at $\sqrt{s} = 7$ TeV**

    Phys. Lett. B 710, (2012) 557-568 (ALICE Collaboration)

20. **J/ψ Production as a Function of Charged Particle Multiplicity in pp Collisions at $\sqrt{s}$ = 7 TeV**

    Phys. Lett. B 712 (2012) 165-175 (ALICE Collaboration)

21. **Multi-strange baryon production in pp collisions at $\sqrt{s}$ = 7 TeV with ALICE**

    Phys. Lett. B 712 (2012) 309 (ALICE Collaboration)

22. **Underlying Event measurements in pp collisions at $\sqrt{s}$ = 0.9 and 7 TeV with the ALICE experiment at the LHC**

    JHEP 1207 (2012) 116 (ALICE Collaboration)

23. **Measurement of charm production at central rapidity in proton-proton collisions at $\sqrt{s}$ = 2.76 TeV**

    JHEP 1207 (2012) 191 (ALICE Collaboration)

24. **J/ψ Suppression at Forward Rapidity in Pb-Pb Collisions at $\sqrt{s_{NN}}$ = 2.76 TeV**

    Phys. Rev. Lett. 109, 072301 (2012) (ALICE Collaboration)

25. **Transverse sphericity of primary charged particles in minimum bias proton-proton collisions at $\sqrt{s}$ = 0.9, 2.76 and 7 TeV**

    Eur. Phys. J. C 72, 2124 (2012) (ALICE Collaboration)

26. **Production of muons from heavy flavour decays at forward rapidity in pp and Pb-Pb collisions at $\sqrt{s_{NN}}$ = 2.76 TeV**

    Phys. Rev. Lett. 109, 112301 (2012) (ALICE Collaboration)

27. **Suppression of high transverse momentum prompt D mesons in central Pb-Pb collisions at $\sqrt{s_{NN}}$ = 2.76 TeV**

    JHEP 9 (2012) 112 (ALICE Collaboration)

28. **Neutral pion and η meson production in proton-proton collisions at $\sqrt{s}$ = 0.9 TeV and 7 TeV**

    Phys. Lett. B 717 (2012) 162-172 (ALICE Collaboration)

29. **K0s-K0s correlations in 7 TeV pp collisions from the LHC ALICE experiment**

    Physics Letters B 717 (2012) 151-161 (ALICE Collaboration)

30. **Production of K*(892) and phi(1020) in pp collisions at $\sqrt{s}$ = 7TeV**

    Eur. Phys. J. C 72 (2012) 2183 (ALICE Collaboration)

31. **Rapidity and transverse momentum dependence of inclusive J/ψ production in pp collisions at $\sqrt{s}$ = 7 TeV**

    Phys. Lett. B 718 (2012) 692-698 (ALICE Collaboration)

32. **Measurement of prompt J/psi and beauty hadron production cross sections at mid-rapidity in pp collisions at $\sqrt{s}$ = 7 TeV**

    JHEP 11 (2012) 065 (ALICE Collaboration)

33. **Coherent J/ψ photoproduction in ultra-peripheral Pb-Pb collisions at $\sqrt{s_{NN}} = 2.76$ TeV**

    Phys. Lett. B 718 (2013) 1273-1283 (ALICE Collaboration)

34. **Ds meson production at central rapidity in proton–proton collisions at $\sqrt{s}$ = 7 TeV**

Phys. Lett. B 718 (2012) 279-294 (ALICE Collaboration)

35. **Inclusive J/ψ production in pp collisions at $\sqrt{s}$ = 2.76 TeV**

    Phys. Lett. B 718 (2012) 295 (ALICE Collaboration)

36. **Pion, Kaon, and Proton Production in Central Pb-Pb Collisions at $\sqrt{s_{NN}}$ = 2.76 TeV**

    Phys. Rev. Lett. 109, 252301 (2012) (ALICE Collaboration)

37. **Measurement of the Cross Section for Electromagnetic Dissociation with Neutron Emission in Pb-Pb Collisions at $\sqrt{s_{NN}}$ = 2.76 TeV**

    Phys. Rev. Lett. 109, 252302 (2012) (ALICE Collaboration)

38. **Measurement of electrons from semileptonic heavy-flavour hadron decays in pp collisions at $\sqrt{s}$ = 7 TeV**

    Phys. Rev. D 86, 112007 (2012) (ALICE Collaboration)

39. **Charge separation relative to the reaction plane in Pb–Pb collisions at $\sqrt{s_{NN}}$ = 2.76 TeV**

    Phys. Rev. Lett. 110 (2013) 012301 (ALICE Collaboration)

40. **Long-range angular correlations on the near and away side in p-Pb collisions at $\sqrt{s_{NN}}$ = 5.02 TeV**

    Phys. Lett. B 719 (2013) (ALICE Collaboration)

41. **Pseudorapidity Density of Charged Particles in p + Pb Collisions at $\sqrt{s_{NN}}$ = 5.02 TeV**

    Phys. Rev. Lett. 110, 032301 (2013) (ALICE Collaboration)

42. **Anisotropic flow of charged hadrons, pions and (anti-)protons measured at high transverse momentum in Pb-Pb collisions at $\sqrt{s_{NN}} =$ 2.76 TeV**

Phys. Lett. B 719 (2013) 18-28 (ALICE Collaboration)

43. **Transverse Momentum Distribution and Nuclear Modification Factor of Charged Particles in p + Pb Collisions at $\sqrt{s_{NN}} = 5.02$ TeV**

Phys. Rev. Lett. 110, 082302 (2013) (ALICE Collaboration)

44. **Centrality Dependence of Charged Particle Production at Large Transverse Momentum in Pb-Pb Collisions at $\sqrt{s_{NN}} = 2.76$ TeV**

Phys. Lett. B 720 (2013) (ALICE Collaboration)

45. **Charged kaon femtoscopic correlations in pp collisions at $\sqrt{s} = 7$ TeV**

Phys. Rev. D 87, 052016 (2013) (ALICE Collaboration)

46. **Measurement of electrons from beauty hadron decays in pp collisions at $\sqrt{s} = 7$ TeV**

Phys. Lett. B 721 (2013) 13-23 (ALICE Collaboration)

47. **Net-Charge Fluctuations in Pb-Pb collisions at $\sqrt{s_{NN}} = 2.76$ TeV**

Phys. Rev. Lett. 110, 152301 (2013) (ALICE Collaboration)

48. **Measurement of the inclusive differential jet cross section in pp collisions at $\sqrt{s} = 2.76$ TeV**

Phys. Lett. B 722 (2013) 262-272 (ALICE Collaboration)

49. **Charge correlations using the balance function in Pb-Pb collisions at $\sqrt{s_{NN}} = 2.76$ TeV**
Phys. Lett. B 723 (2013) 267279 (ALICE Collaboration)

50. **Measurement of inelastic, single and double diffraction cross sections in proton-proton collisions at LHC with ALICE**
Eur. Phys. J. C 73 (2013) 2456 (ALICE Collaboration)

51. **Mid-rapidity anti-baryon to baryon ratios in pp collisions at $\sqrt{s} =$ 0.9, 2.76 and 7 TeV measured by ALICE**
Eur. Phys. J. C 73 (2013) 2496 (ALICE Collaboration)

52. **Long-range angular correlations of π, K and p in p-Pb collisions at $\sqrt{s_{NN}} = 5.02$ TeV**
Phys. Lett. B 726 (2013) 164-177 (ALICE Collaboration)

53. **D Meson Elliptic Flow in Noncentral Pb-Pb Collisions at $\sqrt{s_{NN}} =$ 2.76 TeV**
Phys. Rev. Lett. 111, 102301 (2013) (ALICE Collaboration)

54. **Multiplicity dependence of two-particle azimuthal correlations in pp collisions at the LHC**
JHEP 09 (2013) 049 (ALICE Collaboration)

55. **Centrality dependence of the pseudorapidity density distribution for charged particles in Pb-Pb collisions at $\sqrt{s_{NN}} = 2.76$ TeV**
Phys. Lett. B 726 (2013) 610-622 (ALICE Collaboration)

56. **Centrality dependence of , K, and p production in Pb-Pb collisions at $\sqrt{s_{NN}}$ = 2.76 TeV**

    Phys. Rev. C 88, 044910 (2013) (ALICE Collaboration)

57. **Centrality determination of Pb-Pb collisions at $\sqrt{s_{NN}}$ = 2.76 TeV with ALICE**

    Phys. Rev. C 88, 044909 (2013) (ALICE Collaboration)

58. **J/ψ Elliptic Flow in Pb-Pb Collisions at $\sqrt{s_{NN}}$ = 2.76 TeV**

    Phys. Rev. Lett. 111, 162301 (2013) (ALICE Collaboration)

59. **Multiplicity dependence of the average transverse momentum in pp, p-Pb, and Pb-Pb collisions at the LHC**

    Phys. Lett. B 727 (2013) 371-380 (ALICE Collaboration)

60. **Charmonium and e^+e^- pair photoproduction at mid-rapidity in ultra-peripheral Pb-Pb collisions at $\sqrt{s_{NN}}$ = 2.76 TeV**

    Eur. Phys. J. C 73 (2013) 2617 (ALICE Collaboration)

Conference Proceedings:

1. **Inclusive photon production at forward rapidities for pp collisions at $\sqrt{s}$ = 0.9 TeV and 7 TeV in ALICE at the LHC**

   Sudipan De for the ALICE Collaboration

   Proceedings of DAE Symp. on Nucl. Phys. 56 (2011) 908

2. **Expectation of photon multiplicity in p-p collisions at LHC energies**

   S. Singha, Sudipan De, B. Mohanty, T. K. Nayak

   Proceedings of DAE Symp. on Nucl. Phys. 56 (2011) 986

3. **Charged hadron production in proton-proton collisions at LHC energy**

   S. K. Das, N. R. Sahoo, Sudipan De, T. Nayak

   Proceedings of DAE Symp. on Nucl. Phys. 56 (2011) 988

4. **Forward-backward multiplicity correlations in pp collisions in ALICE at 0.9, 2.76 and 7 TeV**

   G. Feofilov, I. Altsybeev, V. Vechernin, Sudipan De, B. K. Srivastava

   Proceeding of Science (Baldin ISHEPP XXI) 075

5. **Method for the study of forward-backward multiplicity correlations in heavy-ion collisions**

   Sudipan De, B. K. Srivastava, T. K. Nayak

   Proceedings of the DAE Symp. on Nucl. Phys. 58 (2013) 776